NASA CONTRACTOR REPORT

NASA CR-
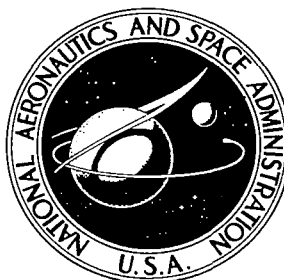
NASA CR-1145

EFFECT OF BLUNTNESS ON HYPERSONIC TWO-DIMENSIONAL INLET TYPE FLOWS

by Robert J. Sanator, John L. Boccio, and Dan Shamshins

Prepared by
FAIRCHILD HILLER
Farmingdale, Long Island, N. Y.
for Ames Research Center

NATIONAL AERONAUTICS AND SPACE ADMINISTRATION • WASHINGTON, D. C. • OCTOBER 1968

EFFECT ON BLUNTNESS ON HYPERSONIC

TWO-DIMENSIONAL INLET TYPE FLOWS

By Robert J. Sanator, John L. Boccio, and Dan Shamshins

TABLE OF CONTENTS

Page

LIST OF ILLUSTRATIONS

v

LIST OF ILLUSTRATIONS (Cont'd)

SUMMARY

An important aerodynamic phenomenon that warrants consideration in the development of inlet analytical techniques arises as a result of the practical constraint of leading edge bluntness. An investigation of the effect of bluntness on two-dimensional hypersonic inlet type flows has therefore been conducted. Specifically, tests were performed on two geometric configurations – a flat plate and an isentropic compression ramp – each accommodating leading edges of three different radii. The nominal test Mach numbers were 7.3 and 10.55, with corresponding free-stream unit Reynolds number ranges of 0.25 to 2.0 x 10^6 per foot, and 0.75 to 2.0 x 10^6 per foot, respectively.

Results generated during the test phases of this program are compared with theoretical analyses and reflect blunt leading-edge effects on inviscid-flow profiles, surface-pressure phenomena and viscous-layer growth along the models, with and without incident shock wave-boundary layer interactions.

INTRODUCTION

Airbreathing propulsion has been proposed as the key to efficient flight at hypersonic speeds. For the intermediate to upper range of speeds, the ramjet engine, operating in the supersonic combustion mode, is the prime propulsive candidate. Important to the ultimate acceptance of these ramjet engines is the ability to design and construct compatible air induction systems. Additionally, because of the stringent requirements placed on inlet test facilities by envisioned engine operational conditions, emphasis must be placed on the development of reliable analytical techniques for use in inlet evaluation and design.

An important aerodynamic phenomenon that warrants consideration in the development of inlet analytical techniques arises as a result of the practical constraint of leading-edge bluntness. This constraint issues from the need to maintain leading-edge heat transfer rates and temperatures at acceptable levels. The leading-edge diameter required is essentially an absolute, dependent only on flight conditions and material properties, with minimums (in the case of active cooling) dictated by producibility and reliability. Therefore the relative consequence of bluntness varies with the application, accentuating with decrease in vehicle size. Elimination of active cooling, increase in flight time and extension of operating envelopes to higher velocities and lower altitudes will also increase the influence of bluntness.

In any event, a highly curved shock wave exists in the inlet flow fields as a result of the finite leading edges of the inlet components. An entropy layer is formed near the surface, consisting of streamlines that have passed through the stronger portions of the curved shock. The presence of this bluntness-induced vortical layer, in which exist strong normal gradients in velocity, temperature and density, has a significant effect upon the downstream boundary-layer development and its response to continuous or discontinuous pressure gradients.

Kutschenreuter, Reference 1, investigated the development of the hypersonic boundary layer, with and without shock wave-boundary layer interactions, on a set of

sharp-edge compression ramps. The flows investigated therein were devoid of bluntness induced external shear that can have significance in practical inlet flows. In fact, there exists a dearth of applicable information regarding the interaction of the bluntness induced entropy layer with the developing viscous layer, particularly in the case where incident shock-boundary layer interactions are present.

The present investigation was conducted to obtain experimental and analytical results showing the effects of leading-edge bluntness, and it is essentially an extension of the sharp leading-edge investigation described in Reference 1. Models with various leading-edge bluntnesses were tested at Ames Research Center and the data obtained were compared with predictions obtained from theoretical analyses. The results show the blunt leading edges effects on inviscid flow profiles, surface pressures and viscous-layer growth on two-dimensional surfaces with and without incident shock wave-boundary layer interactions.

SYMBOLS

B-1	designation of large leading-edge bluntness, leading-edge radius = 0.188"
B-2	designation of small leading-edge bluntness, leading-edge radius = 0.063"
C	designation of flat-plate model, also $T_\infty \mu_w / T_w \mu_\infty$, temperature-viscosity parameter
C_D	$D/(1/2) \rho_\infty U_\infty^2 t$, leading-edge (nose) drag coefficient, = 1.23
$C_{P,P}$	$(P_p - P_o)/(1/2 \rho U^2)_o$, separation plateau-pressure coefficient
D	leading-edge (nose) drag per unit span, lb/ft
E-3	designation of compression-surface model
f'	U/U_E, velocity ratio
g	H/H_E, total-enthalpy ratio
H	total enthalpy, ft^2/sec^2
I_1	$\int_o^\eta (g - f'^2)\, d\eta$
K_ϵ	$M_\infty^3\, C_D\, \epsilon\, (t/X)$
L	model length in free-stream direction, 48 inches
ℓ_T	distance between beginning of interaction to point where maximum pressure is achieved in region (3) of Figure 26
M	Mach number
n	power law profile parameter
P	pressure, lb/ft^2
$P_{(3)}$	maximum pressure achieved in region (3) of Figure 26
Re	Reynolds number
Re/ft	Reynolds number/foot (free stream unless otherwise noted)

3

r $(T_{PROBE} - T_\ell)/(T_T - T_\ell)$, *total-temperature probe recovery factor*

T temperature, °R

t diameter of blunt leading edge, ft

U velocity, ft/sec

X length from sharp leading edge in stream direction, inches, (Figure 5)

Y distance normal to model surface, inches

$\bar{Y}$ *ordinate of compression surface, inches,* (Figure 5)

Z distance along span of model measured from centerline (Table I)

α angle of attack of primary models, 3°

α_g shock-generator inclination

α_L incident-shock turning angle

β $X_\epsilon K_\epsilon^{-2/3}$, bluntness-viscous displacement interaction parameter

δ boundary-layer height, inches

$\delta*$ displacement thickness, inches

ϵ ρ_∞/ρ_s, density ratio across the shock

ζ vorticity, $(sec)^{-1}$

η Howarth-Dorodnitsyn normal coordinate transformation

θ momentum thickness, inches

μ viscosity, lb sec/ft^2

ρ density, lb sec^2/ft^4

χ $M_\infty^3 \sqrt{C_\infty/Re_{\infty,X}}$

SYMBOLS (Cont'd)

X_ϵ $\epsilon \left[0.664 + 1.73 \, (H_W/H_\infty) \right] X$, parameter governing boundary-layer displacement effect

ω exponent in temperature-viscosity relation, $\mu \sim T^\omega$

Ω vorticity interaction parameter

Subscripts

E	edge of boundary layer
inv	edge of an equivalent body in an inviscid flow with vorticity interaction
ℓ	local conditions
p	along pressure plateau
PROBE	pertaining to probe indicated quantity
s	condition just behind bow shock wave
T	total conditions
t	diameter of blunt leading edge, ft
W	conditions at body surface
X	based on length X, inches
∞	free stream
o	beginning of shock wave – boundary layer interaction
(1)	region just upstream of incident shock
2	downstream of normal shock
(2)	region between incident and reflected shock
(2)'	region just downstream of shock-generator leading edge
(3)	region downstream of reflected shock
4	conditions just inside total-temperature probe
δ, δ^*, θ	conditions based on boundary-layer height, displacement thickness and momentum thickness, respectively.

TEST APPARATUS AND MODELS

The current investigation was conducted in the NASA-Ames 3.5 foot Hypersonic Wind Tunnel Facility. The tunnel, shown schematically in Figure 1, is a blow-down type with run times ranging from 1 to 4 minutes. The nominal Mach numbers were 7.3 and 10.55 with corresponding free-stream unit Reynolds number ranges of 0.25 to 2.0 x 10^6 per foot and 0.75 to 2.0 x 10^6 per foot. Helium injection in the tunnel boundary layer is utilized for the purpose of cooling the expansion nozzle wall. During operation, a period of flow stabilization of about 15 to 25 seconds was required before data sampling began. The acquisition of test data was accomplished in five second intervals through a 100 channel Beckman analog to digital recorder. These data were stored on tape and processed by an IBM 7094 computer system.

The models employed in this investigation consisted of a flat plate, shown in Figures 2 and 3, and an isentropic compression surface, shown in Figures 4 and 5. These models were previously used in the studies of Reference 1, but with sharp leading edges only, and are designated there as Model C and Model E-3, respectively. In the present tests both models were aligned at a 3-degree compression angle with respect to the tunnel nominal free-stream direction. Each model could be fitted with any one of three leading edges, i.e., a sharp wedge as in Reference 1, or one of two hemicylinders. One hemicylinder has a 0.188-inch radius and is designated as B-1, while the other has a 0.063-inch radius and is designated as B-2. Secondary shock-generator surfaces, as indicated in Figures 2 through 5, were also provided for both models. While further details of the model configurations can be found in Reference 1, it is noted here that both primary models, (C and E-3), are 48 inches long and that the spans of C and E-3 are 18 and 14 inches, respectively.

Boundary-layer tripping devices were employed in the investigation for those cases where turbulent boundary layers were desired. A schematic representation of the trips used, which essentially are two-dimensional vortex generators is given in Figure 6. Trip configurations 1 and 3 were used on the B-1 compression-surface model when tested at Mach numbers of 10.55 and 7.4 respectively. Likewise, trip configurations 2 and 4 were used for the B-2 compression-surface model. It is pointed out that the only differences between trip configurations 1 and 2 are in the trip distributions

7

along the span of the model and in the projection above the model surface. A typical comparison of the observed trip effectiveness is presented in Figure 7 in terms of non-dimensionalized velocity profiles. Clearly, the wedge vortex generators are effective in promoting transition as evidenced by the relative fullness of the tripped boundary-layer velocity profile.

The model surface instrumentation consisted of pressure orifices and slug-temperature gages. A three-pronged boundary-layer probe, shown in Figure 8, comprised of pitot, stagnation-temperature and field static-pressure probes, was used to obtain profile data. Also shown in Figure 8 is a flow-field rake consisting of five pitot and two static-pressure probes. The locations of surface instrumentation for both models are presented in Tables I and II. Schlieren photographs were used for visual observation of the flow fields.

The indicated temperature measurements, obtained with a singly-shielded thermocouple probe of 0.04 inch O.D., were corrected to the true stagnation temperatures in the manner proposed by Winkler, Reference 2, whereby the temperature-probe recovery, r, is expressed as a function of the convection heat transfer coefficient and the thermal resistance of the thermocouple wire. Relating the aforementioned parameters in terms of experimentally measured quantities, it is possible to define an independent correlation parameter as $\rho_4/T_T^{3/4} \sim P_{T_2}/T_T^{7/4}$. A representative calibration curve is shown in Figure 9 on a semi-log scale. The necessary tunnel reference temperatures were obtained by a Rosemount probe mounted underneath the model in the inviscid free stream.

Since the recovery range used in the present tests extended to values below those tested by Winkler, preliminary calibration tests were performed both in the NASA-Ames tunnel and the von Karman Hypersonic Wind Tunnel Facility at A.E.D.C. The lower recoveries obtained for the probes used, when compared with Winkler's, reflect differences in probe designs dictated by size requirements and placement of the thermocouple bead within the shield.

RESULTS AND DISCUSSION

Experimental results and comparisons with theoretical predictions for the flat-plate and compression-surface models, in the absence of incident shock waves, are presented below in Section A. These primary surface flows are studied first in order to evaluate the ability of various analytical procedures to describe the attendant flow fields. Additionally, the data provide an important experimental base for use in analyzing the shock wave-boundary layer interaction data that are discussed in Section B. To evaluate the effects of bluntness variation on surface flow characteristics and on shock wave-boundary layer interactions comparisons are made with the sharp leading-edge experimental results of Kutschenreuter, et al , and with the theoretical evaluations presented by Gnos, et al , in Reference 3.

A. PRIMARY SURFACE FLOWS

Surface pressure distributions on the compression-surface model are shown in Figure 10 for three different leading-edge radii for a nominal Mach number of 10.55 and a free-stream unit Reynolds number per foot of 2.0 million. The sharp nose experimental results, Figure 10a, are taken directly from Reference 3, while the inviscid theoretical results have been generated using the computer program of Sorensen, Reference 4. For the blunt configurations, Figures 10b and 10c, the inviscid predictions are obtained using the blunt body solution of Lomax, Reference 5, together with the RAD method of characteristics program, Reference 6.

To account for strong viscous interaction on the sharp-nose model, Gnos, et al , use a semi-empirical technique that produces results in agreement with those predicted using the method of Bertram and Blackstock, Reference 7. This method yields closer agreement with experiments in the region near the leading edge than the inviscid predictions shown in Figure 10a. For the large bluntness configuration Gnos, et al , show that agreement between theory and experiment is improved when the inviscid theory is combined with a boundary-layer solution. For the smaller bluntness configuration however, a curious pattern for the sur-face-pressure distribution, indicated by a rise at approximately $X/L = 0.2$, is shown in Figure 10b. Moreover, agreement with the inviscid prediction is poor

9

and, as shown later in this report, only a slight improvement is achieved when the theoretical boundary-layer displacement effects are included.

Surface pressures measured during the current test series, but not presented herein, on the flat-plate model with the B-2 blunt leading edge, also show the same curious rise in pressure observed on the compression surface. Because this rise occurs at approximately the same station for both the flat-plate and the compression-surface models, leading-edge bluntness appears to be the primary cause for the pressure rise. This lack of agreement for the small bluntness case contrasts sharply with the results reported for both the more blunt and the sharp configurations, thus requiring a detailed analysis of the possible underlying causes.

One possibility that might be offered for the noted pressure rise is the presence of a secondary shock in the inviscid field. Vaglio-Laurin, Reference 8, in analyzing inviscid flows about slender bodies and planar surfaces, shows that wave coalescence can occur in the flow field following a complex reflection pattern between the surface and the bow shock. Such an occurrence is also shown by Lighthill, Reference 9. However, both authors conclude that the effects of a secondary shock wave will be noted many nose diameters downstream. Because that conclusion is drawn from the results of approximate inviscid theories, this type of wave coalescence should also be indicated by application of the method of characteristics. However, in the present case, the pressure rise (observed at approximately 75 nose diameters downstream of the leading edge) is not predicted by the method of characteristics within the entire surface length. Consequently, a purely inviscid effect on flow-field development is not considered likely and the phenomenon is attributed to one of viscous interaction.

To account for the influence of viscous interaction on the surface-pressure distribution, two points should be considered: These are the effect of bluntness on boundary-layer transition and the effect of bluntness induced vorticity on boundary-layer development.

Considering boundary-layer transition, Deem and Murphy, Reference 10, note in their studies that unpredicted increases in static pressure occur in the neighborhood of boundary-layer transition on sharp flat plates. Indeed, the

deflection of the external stream by an induced abrupt increase in boundary-layer height can cause a rise in surface pressure. Since the models considered in the present discussion are blunt in contrast to the sharp leading-edge models used by Deem and Murphy, corroboration of boundary-layer transition as responsible for the noted surface-pressure rise, cannot be established. However, it is presently assumed that if transition does occur along the B-2 configurations a concomitant rise in static pressure should accompany the transition process. It remains then to determine if boundary-layer transition is occurring within the region where the pressure rise is observed, i.e., $0.2 \leq X/L \leq 0.4$.

The experimental boundary-layer growth and integral properties for the compression-surface and flat-plate models with the B-2 leading edge are presented in Figure 11. For the flat-plate case, in particular, boundary-layer surveys indicate an abrupt change in boundary-layer characteristics at approximately $X/L = 0.4$. However, Kutschenreuter, et al , report transition to start on the sharp leading-edge models at a downstream station of $X/L = 0.54$. Consequently, under similar free-stream conditions, natural transition on the sharp models is reported to initiate downstream of the station where sudden changes in boundary-layer development are observed for the B-2 blunted configurations. However, Potter and Whitfield, Reference 11, conclude that blunting the leading edges of plates causes the transition point to move downstream. Therefore, although large changes in boundary-layer development are occurring in the region where sharp rises in surface pressure are observed, the possibility of transition occurring in this region is rejected because it contradicts the results of a large body of experimental data. Furthermore, the profile data presented later in this report indicate that if transition occurs, it does so far downstream on the model.

Before assaying the possible effect of bluntness induced vorticity on boundary-layer development and surface pressures, the predictions of theory and the experimental results of the B-1 blunted configurations are compared. The viscous theory used is the nonsimilar boundary-layer analysis of Smith and Clutter, Reference 12, while the inviscid results are obtained from the RAD method of characteristics program. Surface pressures for the compression-surface model are summarized in Figure 12. Data, plotted in terms of the similitude parameters of Chernyi, Reference 13, are from tests conducted at Mach 7.4 and Mach 10.55 with a free-

11

stream unit Reynolds number of 2.0 million per foot. Inviscid calculations at both Mach numbers are shown with viscous corrections for the Mach 10.55 case only. In general, good agreement between the inviscid predictions and experimental results is shown. Slight improvement is obtained when the theoretically determined displacement thickness is used to define the effective body. In addition, reasonably good agreement between theoretical and experimental boundary-layer growths and integral properties is shown for both the compression-surface and flat-plate models in Figures 13 and 14, respectively. For the compression-surface model, a comparison of Figure 10c with Figure 13 shows the viscous-layer growth rate to follow closely the changes in surface pressure, i.e., the rate of growth is progressively retarded as the pressure along the surface increases. The laminar boundary-layer velocity profiles taken at the last downstream profile stations and shown in Figures 15 and 16 also agree well with theory. Comparatively little effect on profile shape due to the mild adverse pressure gradient is also indicated. Thus, for the B-1 blunted configurations, surface-pressure distributions are predicted well by existing theoretical methods and techniques. In addition, boundary-layer growth is shown here, and in Reference 3, to be adequately described by available boundary-layer theories.

The possibility that bluntness induced vorticity is the primary cause of the surface-pressure rise observed for the B-2 blunted configurations is considered below. Because of the lack of an exact theoretical method to analyze the effects of outer-edge vorticity on boundary-layer development, the discussion relies on the experimental observations in addition to some approximate theoretical findings.

The definition of bluntness induced interaction, given by Hayes and Probstein, Reference 14, is that during such an interaction the boundary layer develops within the pressure and vorticity field created by the slightly blunted leading-edge of an otherwise slender body. Ferri and Libby, Reference 15, originally pointed out the existence and importance of vorticity interaction. Without external vorticity the assumption that conditions at the outer edge of the boundary layer are well approximated by inviscid wall conditions, is valid. With external vorticity however, the velocity at the outer edge must equal the velocity in the inviscid flow at the same value of the stream function. The significance of changes in outer-

edge conditions and streamline absorption into the developing boundary layer is further discussed in a survey article by Benefield and Hair, Reference 16. The results show the iterative technique of combining and matching the boundary layer and inviscid flow field to be an improved mathematical flow field model.

The theoretical inviscid stagnation pressure, normalized with respect to the Mach 10.55 free-stream value, at three boundary-layer profile stations, along the flat plate are shown in Figure 17. Figure 17(a) typifies the results for the larger blunted configuration, while Figure 17(b) shows the results for the smaller bluntness case. Respective boundary-layer growths, interpolated from the experimental data obtained at unit free-stream Reynolds number per foot of 2.0 million, are superimposed on the figure. The stagnation-pressure ratio, which is directly related to entropy, indicates the boundary layer for the larger bluntness configuration to be developing in a region of essentially constant entropy normal to the body. In this case then, large entropy gradients, which manifest themselves, kinematically, in large vorticity gradients, are not the prevalent effect on boundary-layer growth. Rather, the boundary layer develops primarily under the influence of the bluntness induced pressure distribution.

For the smaller blunted configuration the boundary layer appears to be developing in regions where large variations in entropy normal to the body surface are occurring. This is tantamount to large gradients in boundary-layer edge properties. In Figure 18, where the predicted and measured edge values are compared, it is noted that the edge condition variations for the B-2 configuration are quite large compared to those for the B-1 blunt configuration. Moreover the good agreement between theory and experimental results for the B-1 configuration is not observed for the B-2 case.

Figure 19 indicates the variations in normalized velocity derivatives in the neighborhood of the boundary-layer edge at the corresponding three stations of Figure 17. For the larger blunted configuration, Figure 19(a) shows the gradient at the outer edge to be nearly zero while for the smaller blunted configuration, Figure 19(b), the edge velocity gradients are relatively quite large. According to Reference 14,

13

when the vorticity interaction parameter, which is approximated by

$$\Omega = \zeta_{inv} / (U_{inv} / \delta),$$ (1)

and which is essentially a measure of the ratio of external inviscid vorticity to the average vorticity in the boundary layer, is of order one, vorticity interaction should be taken into account. Note, that the subscript "inv" refers to flow properties obtained at $Y = \delta$ in an equivalent inviscid flow. If the vorticity interaction parameter is taken as

$$\Omega \approx \left[\partial (U/U_E) / \partial (Y/\delta) \right]_{Y = \delta}$$ (2)

with

$$\zeta_{inv} \approx (\partial U / \partial Y)_{Y = \delta}$$ (3)

and

$$U_{inv} \approx U_E$$ (4)

then examination of Figure 19(b) yields values of Ω which range from nearly zero at $X/L = 0.33$ to a value close to 0.4 at $X/L = 0.54$. For the case shown in Figure 19(a) the vorticity interaction parameter is nearly zero at all three stations. Also, since the edge gradients shown in Figure 19(b) indicate that the value of the parameter, Ω, is lower at $X/L = 0.79$ than at $X/L = 0.54$, there must exist a region along the body where Ω reaches a maximum. Thus the importance of vorticity interaction in the present flow situation is evident.

The complete experimentally determined velocity profiles at the three stations discussed above for the B-2 blunted flat plate are shown in Figure 20. In addition to the superimposed theoretical results, a velocity profile with a profile parameter, n, of two, is also shown at the last station. The disparity between the experimental results and the theoretical boundary layer analyses is quite evident. However, the velocity profile at the last station agrees fairly well with that obtained using the profile parameter value of two.

14

This value of n is the lower limit ascribed by Kutschenreuter, et al, to transitional profiles; the upper limit being five. With this criterion it is possible to conclude that transition is occurring at this station, i.e. at $X/L = 0.79$. This result is in support of the conclusion drawn earlier that transition is not occurring in the region where pressure rises are noted.

In addition to the lack of agreement with laminar boundary-layer theory at the downstream stations shown in Figure 20, there is noted an increased fullness with respect to a laminar profile near the wall for the latter two profiles and the existence of inflection in profile curvature. The increased profile fullness agrees with the result of Hayes and Probstein that external shear interaction increases the value of skin friction above that usually predicted by laminar theory. The inflection connotes a double layer nature to the profile and implies the action of external shear on laminar-profile development.

The poor agreement between experimentally determined boundary-layer integral properties and the results of Smith and Clutter for the B-2 flat plate configuration, shown in Figure 21, in contrast to the rather good agreement for the correspondingly larger blunted configuration, shown in Figure 14, reaffirms the inadequacy of conventional boundary layer theories to account for rapid changes in edge conditions. In the case of the smaller bluntness, the bow-shock induced vorticity adjacent to the boundary layer has been shown to be approximately one-half of the average vorticity generated within the boundary layer. Because of the inability to account for inviscid vorticity in the external boundary conditions, the application of conventional boundary layer analytical techniques is questionable in these cases.

While the above demonstrates the effect of vorticity on boundary-layer development, the effect of vorticity on surface pressure remains to be shown. For the B-2 compression-surface model, comparisons are shown in Figure 22 of the experimental pressures and those predicted by the theoretical procedures previously described for the B-1 compression model. In addition, attempts to account for boundary-layer edge variations by using the experimentally determined displacement-thickness distribution in the usual inviscid-viscous calculations for

the Mach 10.4 flow situation are shown. The discrepancy between theory and experiment at the higher Mach number between the values of the Chernyi parameter of .009 and .018 (corresponding to X/L between 0.2 and 0.4) is clearly indicated. When the experimentally determined displacement-thickness distribution is employed in the usual superposition procedure, the measured pressure distribution is simulated, qualitatively, indicating that the effect observed is traceable to an interaction between the inviscid and viscous flows. At Mach 7.4, agreement with the inviscid predictions is better than at the higher Mach number. This result is explained as follows: at the same value of unit Reynolds number, both the boundary-layer thickness and shock-wave curvature are reduced for the lower Mach number; thus the effects of bluntness-induced vorticity will be felt by the developing boundary layer at a much further downstream station.

The idea of an interaction region where the pressure distribution is dependent on both bluntness-induced and viscous-induced effects is introduced in the entropy layer theory of Cheng, Reference 17. The shock layer is assumed to be composed of three layers, a viscous layer along the body surface, and inviscid entropy layer generated by the highly curved portion of the shock, and an inviscid region where the hypersonic small disturbance theory may be applied. Of course the existence of three distinct layers, especially the entropy layer, is only a mathematical artifice that allows analytic approximations to the physical processes. The asymptotic solutions obtained by Cheng yield explicit estimates of regions of bluntness and displacement thickness dominated flow. A measure of the two effects is contained in the parameter, β,
where

$$\beta \equiv \chi_\epsilon \, K_\epsilon^{-2/3} \tag{5}$$

The quantity, χ_ϵ, is a parameter governing the boundary-layer displacement effect and K_ϵ is a parameter controlling the inviscid tip-bluntness effect. These parameters are defined by Cheng as

$$\chi_\epsilon \equiv \epsilon \left[0.664 + 1.73 \, (H_W/H_\infty) \right] \chi \tag{6}$$

$$K_\epsilon \equiv M_\infty^3 \, C_D \, \epsilon \, (t/\chi) \tag{7}$$

16

It is found that for values of $\beta \leq 0.1$, bluntness effects are dominant, whereas the boundary-layer displacement effect is of primary importance if $\beta \geq 1.0$. Within these two limits exists the region of combined bluntness and viscous interaction. The downstream extent of this region corresponds to the point of complete injestion of the entropy layer by the developing boundary layer. However, within this region two forms of viscous interaction are presently proposed. One form corresponds to the case where the surface pressures induced by boundary-layer growth begin to exceed those induced by the blunt leading edge. The other form of viscous interaction proposed is due to vorticity. The induced effect on pressures of the rapidly changing displacement thickness, resulting from the injestion of stream-lines of rapidly varying entropy into the boundary layer, must be considered in addition to the inviscid bluntness induced effect.

Of course, the limits discussed above are approximate. In fact the bluntness induced limit of $\beta < 0.1$ is derived from blast wave solutions and vorticity is not considered at all! However, the following possible sequence of events is proposed. With $\beta < 0.1$ the inviscid surface-pressure field engendered by the leading edge is the dominant factor in boundary-layer development. As β increases and approaches 0.1, the influence of external shear generated by the curved shock is requisite to the development of the boundary layer as is the bluntness induced pressure distribution. These two influences gradually diminish as the entropy layer is being injested by the developing boundary layer. Hence as β approaches unity, the "memory" associated with the effect of the blunt leading edge on surface-pressure distribution and boundary-layer development disappears. Simultaneously, the self-induced pressure field generated by the developing boundary layer increases in importance with increasing β.

Rewriting Equation (5) using Equations (6) and (7) yields

$$\beta = \frac{\sqrt{2}}{C_D^{2/3}} \, \epsilon^{1/3} \, \sqrt{C_\infty} \, (I_1 M_\infty) \, (R_{e_\infty , t})^{-1/2} \, (X/t)^{1/6} \tag{8}$$

This is the form for β used by Dewey, Reference 18. Dewey applies the methods of local similarity in investigating viscous interaction problems. As such there

is no necessity to distinguish between strong and weak interactions. The parameter I_1, defined by Dewey as the displacement-thickness integral, is, under the assumption of a perfect gas with constant specific heats, given by

$$I_1 = \int_0^\eta (g - f'^2) \, d\eta \qquad (9)$$

I_1 is a function of the pressure gradient, the stagnation-temperature ratio at the wall, the Prandtl number, and the viscosity exponent. In Cheng's analysis the pressure gradient is assumed small. Consequently, the value of I_1 can be approximated by

$$I_1 = [0.455 + 1.22 \, (H_W/H_\infty)] \qquad (10)$$

For $M_\infty = 10.55$, free stream unit Reynolds per foot of 2.0 million, leading-edge thickness, t, equal to 0.126-inches, nose drag coefficient, C_D, of 1.23 and a wall stagnation temperature ratio, T_W/T_T, of 0.25

$$\beta = 4.48(10)^{-2} \, (X/t)^{1/6}$$

where, in the above, the temperature viscosity parameter, C_∞, is given by

$$C_\infty = (T_\infty/T_W)^{1-\omega}$$

with the viscosity exponent ω equal to 0.76. The density ratio across the shock, ϵ, has been approximated here by that associated with a 3° sharp wedge. Thus for bluntness effects to be dominant, i.e., $\beta \approx 0.1$,

$$X/t \leq 125$$

or

$$X/L \leq .328$$

From the above calculations, it appears that approximately 70% of the length of the B-2 blunt configurations is in the region of combined bluntness and viscous interaction. The qualitative sketch shown in Figure 23 illustrates the behavior

18

of the viscous-interaction and bluntness-interaction contributions to the surface pressure and also shows a possible distribution within the combined interaction region.

Thus, significant effects directly attributable to leading-edge bluntness have been shown by the presently reported experimental study. These effects were traced to the bluntness induced entropy-layer flow and the manner in which it interacts with the developing boundary layer.

No definite conclusions regarding leading-edge bluntness induced vorticity on turbulent boundary-layer development can be drawn from the experimental results since natural turbulent flow was not achieved for the conditions at which the models were tested. The use of boundary-layer trips affects the external flow as well as the boundary-layer development. Thus the vorticity within the inviscid flow field is a result of entropy gradients produced by both the blunt leading-edge bow wave and the shocks generated by the boundary-layer trips. It appears however that trips reduce the velocity gradients at the edge of the boundary layer. Figure 24 compares the velocities near the edge of the boundary layer for a tripped and an untripped condition. These velocity profiles were measured at station X/L = 0.54 on the flat plate model at Mach 10.55 and free stream unit Reynolds number per foot of 2 million.

An experimental and analytical study of the flow field about blunt two-dimensional bodies has shown significant effects directly attributable to leading-edge bluntness induced vorticity. Tests conducted at Mach 10.55 and 7.4 and free stream unit Reynolds number per foot of 2 million have shown that:

- For the 0.188-inch leading-edge radius models, the usual boundary-layer displacement technique, which simply considers the viscous effect by displacing the flow by the boundary-layer displacement thickness, agrees well with experiment.

- For the 0.063-inch leading-edge radius models, only fair agreement exists between surface pressure measurements made at Mach 7.4 and those predicted by inviscid theory. Better agreement is expected if the viscous displacement effects are included in the theoretical analysis.

19

- At Mach 10.55, agreement with theory and experiment for the 0.063-inch leading-edge radius model is poor. Examination of measured boundary-layer profiles, comparisons with similar experiments on the sharp configurations, and order of magnitude analyses of the viscous-interaction phenomena have shown bluntness-induced vorticity to be a possible cause for the discrepancy.

The shear, or vortical-layer flow, associated with bluntness introduces local flow conditions that have a strong influence on the development of the boundary-layer flow. The influence that bluntness has on shock-boundary-layer interaction is discussed in the next section.

B. FLOWS WITH SHOCK WAVE–BOUNDARY LAYER INTERACTIONS

This section of the report summarizes the experimental results pertaining to laminar and turbulent viscous layer – shock wave interactions on the configurations previously described. Both surface–pressure data and profile data within the interaction region are illustrated. To augment the discussion, schlieren photographs are displayed. Correlation with existing theories and comparisons with results of similar experiments with both sharp and blunt leading edges are presented. For the corresponding sharp leading-edge studies, reference is made to the works of Watson, et al, Reference 19, and Kutschenreuter, Reference 1. A compendium of sharp-nose results with and without shock wave–boundary layer interactions is given by Watson, et al, Reference 20.

As in the case of shock wave–boundary layer interactions along bodies with sharp leading edges, the corresponding interaction region along the blunted configuration displays similar salient features. Disturbances caused by the incident shock propagate upstream through the boundary layer causing it to thicken. The thickening boundary layer interacts with the inviscid flow causing the surface pressure to rise from that level measured in the absence of interaction. If the disturbance is strong enough a separation bubble occurs which gives rise to a pressure plateau. Also, the reattachment of the separated region produces a reattachment compression wave system that eventually will coalesce into a shock.

Although most of these salient features are readily distinguishable and comparable to similar interaction on bodies with sharp leading edges, the effect of blunting the leading edge produces additional complications in the interacting flow. These are the influences of the bluntness induced vortical layer on the developing boundary layer and the effect of the non–uniform primary–surface shock-layer flow properties on the shape and strength of the secondary incident shock.

In addition, the blunt-edge case introduces an experimental difficulty. The schlieren effectiveness is reduced because the existence of the entropy layer reduces the density gradients at the boundary-layer edge as illustrated in Figure 25. Figure 25(a) shows a typical schlieren photograph taken during a test with shock

wave-boundary layer interaction in the presence of external shear. It is observed that in contrast to the schlieren photograph shown in Figure 25(b), which is typical of those taken for flows about sharp bodies, the boundary-layer edge is not distinguishable.

Pressure Distributions

Of specific interest in shock wave-boundary layer interaction is the pressure rise across the interaction, $P_{(3)}/P_{(1)}$, as a function of the strength of the incoming disturbance. Comparison of pressure rises across the interaction region, whose domain is defined in Figure 26, with inviscid predictions obtained using a modified form of the computer program of Sorensen (that accounts for the blunt leading edge), is shown in Figure 27 for the compression surface model. The sharp leading-edge data of Kutschenreuter, et al, for the corresponding Mach 10.4 and 7.3 conditions are also indicated on Figure 27. In Figure 28, absolute pressure rises, $P_{(3)}/P_\infty$, as a function of initial shock-generator pressure ratio, $P_{(2)}'/P_\infty$ for the sharp and blunt flat-plate models are presented. The sharp leading-edge data and inviscid theory of Reference 1 are also shown.

Before drawing specific attention to these figures, two comments are noteworthy. First, it should be realized that the theoretical distributions shown in Figure 27 do not account for the longitudinal extent of the interaction region. This simplification can lead to errors if the impinged surface supports an existing surface-pressure gradient in the absence of shock-boundary layer interaction. Consequently, since the theoretical inviscid shock impingement and subsequent reflection occur along a mathematically infinitesimal length of the body, differences between the experimental value of $P_{(3)}$, the maximum pressure achieved in region (3), and the corresponding theoretical values of the surface pressure just downstream of the theoretical reflected shock can be expected. The contributions of the actual reflection processes thus include the effect of additional flow-field development prior to the point at which the experimental value of $P_{(3)}$ is chosen and also include the possible interaction of the expansion fan emanating from the aft-end of the shock generator.

Another point deals with the choice of the parameter defining the incident-shock strength. For interactions along sharp bodies, an upstream condition and the shock-generator setting are sufficient to define the incident wave. Analytical expressions can simply be used to relate such parameters directly to shock strength,

that is, the ratio $P_{(2)}/P_{(1)}$ across the incident wave. For blunted configurations however, correlation of absolute pressure levels achieved is not as ostensibly related to shock-generator angle. In fact, exact analytical expressions relating shock-generator angle to incident-shock strength do not exist since the strength of the incident wave varies as it traverses the bluntness induced flow field. The results, using the Sorensen computer program, modified to account for leading-edge bluntness, indicate that for a given generator angle and bluntness, the strength of the incident shock decays as it traverses the shock layer of the primary surface. The shock angle relative to the free-stream direction increases toward the primary surface, as shown in Figure 29. Of course, the decay in shock strength and the amount of curvature are functions of the location of the shock-generator-leading edge with respect to the leading edge of the primary surface. The amount of leading-edge bluntness of the primary surfaces is also an important factor. Thus, the strength of the incoming wave is taken to be the theoretical shock strength at a height above the plate equal to the measured boundary-layer height. This procedure seems justifiable due to the general agreement in the location of the sudden rise in surface pressure and the intersection of the theoretical shock waves with the measured boundary-layer heights, as shown in Figure 29. These boundary layer-heights were obtained from the study of primary surface flows without shock interactions.

Overall pressure rises as a function of incident-wave strength for the compression-surface model at Mach numbers of 10.4 and 7.3, shown in Figures 27 (a) and 27(b), respectively, indicate the blunt leading-edge data to be generally lower than that predicted by theory. Comparison of the experimental data shows that an incoming wave of a given strength impinging on the sharp body produces a larger overall pressure than on the blunted configurations. For the flat-plate model, Figure 28, a similar observation is made. That is, a reduction in absolute pressure achieved across an interaction, for a given incident-shock strength, occurs for the blunted configurations. Stated somewhat differently, the above two figures show that to maintain a certain overall pressure ratio across the interaction region requires stronger incident waves for the blunted leading-edge configuration models than for the corresponding sharp leading-edge configurations.

Typical surface-pressure distributions within the domain of interest resulting from incident shock wave-laminar boundary-layer interactions along the compression-

surface model are shown in Figures 30 and 31 for Mach 10.4 and in Figures 32 and 33 for Mach 7.3. Figures 30 and 32 illustrate the surface pressures for the B-1 configuration while Figures 31 and 33 are for the small blunted configuration. For comparative observation, each plot also contains the pressure distribution for the zero interaction case with the value of X_o equal to the most upstream value of X_o for the interaction cases plotted. As the figures indicate, for the laminar interactions, separation along the compression surface is observed for all generator angles. The results indicate a relatively minor effect on plateau-pressure levels and on the location of the beginning of interaction with increasing generator angles. Thus, although the interaction length increases with generator angle due to incident shocks of increasing strength, the beginning of interaction remains relatively fixed. Such observations tend to corroborate the findings of Chapman, Kuehn, and Larson, Reference 21, Erdos and Pallone, Reference 22, and Needham and Stollery, Reference 23, that the value of the plateau pressure is a function of local conditions.

Surface-pressure distributions for shock wave-turbulent boundary-layer interactions occurring along the blunted compression-surface model at a free-stream Mach number of 7.4 are shown in Figures 34 and 35 and at Mach 10.55 in Figures 36 and 37. Figures 34 and 36 summarize the data obtained for the B-1 blunted configurations while Figures 35 and 37 are for the B-2 blunted configuration. For the turbulent cases, in contrast to the laminar cases, both attached and separated interactions are observed.

At Mach 7.4, separation, defined by an inflection in the pressure rise, occurs somewhere between 4° and 6° for the large bluntness configuration (Figure 34). Beyond this angle the inflection region increases in the longitudinal direction. For the smaller bluntness configuration (Figure 35), no inflection (hence no separation) is evident for any of the cowl generator angles indicated. In fact, although not shown in the figure, tests with generator angles of 15° failed to cause separation. Thus on the basis of these observations, separation is more likely to occur, for the same

free-stream conditions and shock-generator angle, for the more blunted configuration. At Mach 10.55, further evidence of the increasing tendencies toward separation with increasing bluntness is obtained by comparing Figures 36 and 37. Although the experimental data make it difficult to draw a conclusion regarding the effect of Mach number on the susceptibility of the boundary layer to separation as a result of the interaction, the definite plateaus in pressure shown for the 7.4 Mach number cases in Figure 34, as opposed to the pressure inflections shown for the 10.55 Mach number cases of Figure 36, lead one to suspect that increasing the Mach number will increase the shock generator angle required for separation.

Direct comparative representation of surface-pressure distributions illustrating the effects of increasing bluntness on shock wave-laminar boundary-layer interactions is given in Figure 38. At a generator angle of 3 degrees, the sharp leading-edge model displays an attached interaction, whereas the blunted configurations at the same generator angle exhibit surface pressure rises under the influence of a separated boundary layer. Similarly for turbulent interactions, the increasing tendency for separation with increasing bluntness indicated previously is emphasized in Figure 39. Increasing the generator angle from 4 to 6 degrees causes the turbulent boundary layer to separate on the B-1 configuration while still remaining attached along the smaller bluntness B-2 model.

In order to determine the specific effect of bluntness that produces the results described above, it is important to note that bluntness produces opposing effects with regard to boundary-layer separation. Increasing the bluntness provides lower edge Mach numbers and local unit Reynolds numbers. Holden, Reference 24, shows that decreasing the edge Mach number promotes flow separation while decreasing the Reynolds number tends to inhibit flow separation. From the present tests, the reduction in edge Mach number due to bluntness appears to be the dominant cause in increasing the tendencies for boundary layer separation.

Boundary-Layer Development

In addition to surface-pressure measurements within the interaction region, boundary-layer survey data were also obtained. Figure 40 shows the pitot and static-pressure profiles measured within a separated turbulent-interaction region along the B-1 blunted compression-surface model. Data are shown for the free-

stream Mach number of 7.4 and free-stream unit Reynolds number per foot of
2.0 million and with a shock-generator inclination of six degrees. The profile stations,
i.e., X/L = 0.646 and 0.775, are, respectively, upstream and downstream of the
shock-impingement location. The latter profile is within the region of maximum
surface pressure.

The same data have been used to generate Figure 41. In this figure the
velocity profiles, which are calculated using the corrected total temperature to-
gether with the measured pitot and static pressures, are superimposed on the
corresponding schlieren photograph. The two waves shown are, respectively, the
induced wave and the recompression shock wave while the incident wave is out-
side of the field of vision. The boundary-layer height at the upstream profile
station is 0.52-inches, while at the downstream station it is 0.3-inches. Figure
40 shows the static-pressure variation normal to the surface to be small for the
upstream profile. For the downstream profile a marked variation in static pres-
sure is evident. However these variations are largely outside the viscous layer.

The surface-pressure distribution within the interaction region, shown in
Figure 41, indicates a plateau to start at approximately 33.5-inches and to be
0.5-inches in length. A summary of total-pressure, static-pressure, velocity
and total-temperature profiles for the corresponding two stations are shown in
Figures 42 through 45.

For similar free-stream conditions and shock-generator angle, profile data
within an attached turbulent interaction along the B-2 blunted compression model
are shown in Figures 46 and 47. In this case however both profiles are downstream
of incident-shock impingement point. The profile stations are two inches apart,
with the upstream station located at X/L = 0.775. The gap in the pitot-pressure
data between Y equal to 0.2-inch and 0.4-inch for the downstream station is due
to erroneous data recorded within this region. The data, if available, would be
expected to indicate a peak pressure as indicated by the dotted line. This peak
would occur at the lower edge of the reflected shock shown in the schlieren photo-
graph of Figure 47. The boundary-layer data at X/L = 0.813, shown in Figures
48 through 51, are correct however, because the δ = 0.18-inch is within the region
where valid data were obtained.

Correlation With Theory

An attempt to apply the analysis of Lees and Reeves, Reference 25, to include shock wave–boundary layer interactions over blunted plates was unsuccessful. The primary effect of bluntness on the analysis of Lees and Reeves lies in the violation of the assumed homentropic state upstream and downstream of the interaction. Thus because of bluntness, the interaction between the inviscid and viscous flow cannot set up Prandtl-Meyer compression waves, as is assumed, because of the non-uniformity of the incoming flow at the beginning of interaction. Also, the impinging shock wave is curved because of this non-uniform state and as such the straight-shock reflection routine used in the analysis is not applicable. Further, because of the downstream nonhomentropic state, the viscous velocity profiles cannot approach the Blasius type as is assumed. The analysis of Holden attempts to account for non-uniform conditions upstream of a shock wave-boundary layer interaction. Holden points out that interactions influenced by strong viscous-inviscid coupling prior to shock impingement can correlate well with the viscous hypersonic similitude parameters. Experiments along sharp plate–wedge model configurations corroborate this claim. For a blunted plate, however, the boundary-layer development is quite different from that on the sharp configuration. From the foregoing, it is believed that an analytical approach attempting to describe interactions along slender, blunted bodies remains lacking.

In view of the above, it is worthwhile to apply the simple correlation laws to the current cases of shock interactions along blunted configurations. The experimental investigations herein reported together with similar studies on blunted ramp-wedge combinations such as those of Townsend, Reference 26, and Graham and Vas, Reference 27, have indicated the separation phenomenon to be strongly dependent on the local flow conditions at the beginning of interaction. In Figure 52, the plateau-pressure coefficients occurring within a laminar interaction obtained from the present experimental program are compared with the results reported by Townsend. The shaded area in the vicinity of $M_{E,X_O} = 3$ represents Townsend's results on a blunted ramp-wedge model. The remaining shaded areas, taken from Figure 13 of the aforementioned report and duly referenced therein, represent similar testing on sharp configurations. Data from the present tests are indicated by the darker

27

symbols. These data were obtained from the tests conducted at Mach numbers of 7.4 and 10.4 for a variety of shock-generator angles. In general the data for both the compression-surface and flat-plate models agree well with the theories of Chapman, et al., and Erdos and Pallone. For the compression-surface model, the two data points that fall well above the theoretical predictions were obtained from interactions due to incident shocks impinging well up on the compression surface. As such, the plateau-pressure coefficient is dependent on the pressure rise due to the effects of the compression surface in addition to that associated with the interaction.

Correlation of total interaction lengths, ℓ_T, defined as the distance from start of the interaction to the peak-pressure location, with the incident-shock turning angle, is presented in Figure 53 together with Pinckney's, Reference 28, semi-empirical results and the sharp data of Reference 19. Although the experimental data were obtained under similar Mach number conditions as the theory, the profile parameters, as indicated, are different. In addition, the incident-shock turning angle was obtained using the Sorensen computer program and a procedure similar to that previously discussed for the choice of the incident-shock strength. Consequently, the flow deflection angle used in the figure is that which occurs theoretically across the incident-shock point located at a height above the surface equal to the interpolated experimental boundary-layer height. Also, the results of Pinckney come from investigations with adiabatic wall conditions while the data shown are from cold wall studies, and, as noted in Reference 19, care should be exercised in extrapolating the results of Pinckney. However, the trend indicated by the theory is in general agreement with the data shown.

A similar correlation of total interaction length for shock wave-laminar boundary-layer interaction with the net pressure rise across the interaction region is shown in Figure 54. In the plot, the interaction length, in addition to being normalized with respect to the boundary-layer height at the beginning of inter-action, is also multiplied by governing parameters of References 21 and 22. For both the sharp and blunt leading-edge models, the data concentrate around each geometric configuration. The observed concentration of data points around each geometric configuration, i.e., flat plate and compression surface, lends further credence to the importance of local conditions on interaction criteria. Also, the

data suggest that correlation of various geometric configurations, can be made if the parameters contained some geometric characteristic since the data for both models display essentially linear trends on a logarithmic scale. However, no attempt has been made here to determine such a parameter. The data also indicate that the effect of the compression ramp is to reduce the total interaction length. However, it should be recalled that some uncertainty in the data exists due to the introduction of expansion waves from the aft portion of the shock generator into the interaction region.

CONCLUDING REMARKS

An experimental program has been undertaken, in the 3.5 foot hypersonic wind tunnel at NASA-Ames Research Center, to study the effects of leading-edge bluntness on flow-field development and on incident shock wave-boundary layer - interactions. Specifically, tests were conducted on two geometric configurations - a flat plate and an isentropic compression ramp - each accommodating leading edges of three different radii.

Significant effects on flow-field development have been shown to be directly attributable to leading-edge bluntness. These effects are traced to the bluntness induced entropy layer and the manner in which it reacts with the developing boundary layer. Tests conducted on the primary surfaces at Mach 10.4 and 7.4 and free stream unit Reynolds number per foot of 2 million show that:

- For the 0.188-inch leading-edge radius models, the usual boundary-layer displacement technique, which simply considers the viscous effect by displacing the flow by the boundary layer displacement thickness, agrees well with experiment

- For the 0.063-inch leading-edge radius models, only fair agreement exists between surface pressure measurements made at Mach 7.4 and those predicted by inviscid theory. Improved agreement is expected if the usual viscous displacement effects are considered.

- At Mach 10.55, agreement with theory and experiment for the 0.063-inch leading edge radius model is poor. Examination of measured boundary-layer profiles, comparisons with similar experiments on the sharp configurations, and order of magnitude analyses of the viscous interaction phenomena have shown bluntness induced vorticity to be a possible cause for the discrepancy.

Within the domain of variables for the shock wave-boundary layer interaction tests, leading-edge bluntness is observed to promote separation. In establishing this fact, considerations of the effects of leading edge bluntness on boundary layer development, on flow conditions just external to the boundary layer and on the

31

strength and location of the incident shock have been made. Since bluntness produces lower downstream edge values of Mach number and Reynolds number, the former tending to promote separation and the latter tending to retard it, it is concluded that the Mach number effect apparently dominates the separation criteria.

REFERENCES

1. Kutschenreuter, Paul , Brown, L. David, Hoelmer, Werner. et al, "Investigation of Hypersonic Inlet Shock-Wave Boundary Layer Interaction," AFFDL-TR-65-36, 1966.

2. Winkler, E.M., "Stagnation Temperature Probes for Use at High Supersonic Speeds and Elevated Temperatures," NAVORD Report 3834, U.S. Naval Ordnance Lab., White Oak, Maryland, October 1954.

3. Gnos, A. Vernon, Gallo, William F. and Latham, Elden A., "Two-Dimensional Boundary Layers and Flow Fields of Hypersonic Inlets," Conference on Hypersonic Aircraft Technology, Ames Research Center, May 16-18, 1967, pp 299-313.

4. Sorensen, V.L., "Computer Program for Calculating Flow Fields in Supersonic Inlets," NASA TND - 2897, July, 1965.

5. Lomax, H, and Inouye, M., "Numerical Analyses of Flow Properties About Blunt Bodies Moving at Supersonic Speeds in an Equilibrium Gas," NASA-TR R-204, 1964.

6. Cousin, S.B., and Casaccio, A., "The Calculation of Ideal and Real Gas Shock Layers about Slender Bodies by the Method of Characteristics," Republic Aviation Report No. 2889, June, 1965.

7. Bertram, M.H., and Blackstock, T.A., "Some Simple Solutions of the Problem of Predicting Boundary Layer Self-Induced Pressures, "NASA TND-798, 1961.

8. Vaglio-Laurin, R., "Asymptotic Flow Pattern of a Hypersonic Body," PIBAL Rep. No. 805, Dept. of Aerospace Eng. and Appl. Mach. Polytechnic Inst. of Brooklyn, 1964.

9. Lighthill, M.J., "The Energy Distribution behind Decaying Shocks -I. Plane Waves, " Phil. Mag., Ser 7, Vol. 41, No. 322, November 1950.

10. Deem, R. E., and Murphy, J. S., "Flat Plate Boundary Layer Transition at Hypersonic Speeds, "Douglas Aircraft Company, AIAA Paper No. 65-128, January, 1965.

11. Potter, J. L., and Whitfield, J. D., "Boundary - Layer Transition Under Hypersonic Conditions," AEDC-TR-65-99, May, 1965.

12. Smith, A. M. O., and Clutter, D. W., "Solution of the General Boundary Layer Equations for Compressible Laminar Flow, Including Equilibrium Dissociation, "Douglas Aircraft Company Engineering Paper No. 1657, November, 1963.

13. Chernyi, G. G., "Introduction to Hypersonic Flow, "Translated and Edited by R. F. Probstein, Academic Press, 1961.

14. Hayes, W. D. and Probstein, R. F., "Hypersonic Flow Theory, "Academic Press, New York, 1959.

15. Ferri, A., and Libby, P. A., "Note on the Interaction Between the Boundary Layer and the Inviscid Flow, " J. Aero Sci., 21, 130, 1954.

16. Benefield, J. W., and Hair, L. M., "Inlet Flow Field Analyses for High Mach Number Applications," J. Spacecraft, Vol 4, No. 5, May, 1967.

17. Cheng, H. K., "Hypersonic Flow with Combined Leading Edge Bluntness and Boundary Layer Displacement Effect, "Cornell Aeronautical Laboratory Report No. AF-1285 - A - 4, August, 1960.

18. Dewey, Jr., C.F., "Bluntness and Viscous - Interaction Effects on Slender Bodies at Hypersonic Speeds, "Rand Corporation Memorandum RM-3832-PR, September, 1964.

19. Watson, Earl C., Murphy, John D., and Rose, William C., "Shock Wave-Boundary Layer Interactions in Hypersonic Inlets, "Conference on Hypersonic Aircraft Technology, Ames Research Center, May 16-18, 1967, pp 315-344.

20. Watson, E. C., Gnos, A. V., Gallo, W. F. and Latham, E. A., "Boundary Layers and Hypersonic Inlet Flow Fields, "AIAA Paper No. 66-606, AIAA Second Propulsion Joint Specialist Conference, Colorado Springs, Colorado, June 13-17, 1966.

21. Chapman, D. R., Kuehn, D. M. and Larson, H. K., "Investigation of Separated Flows in Supersonic and Subsonic Streams with Emphasis on the Effect of Transition, " NACA Rep. 1356, 1958. (Supersedes NACA TN 3869)

22. Erdos, J., and Pallone, A., "Shock-Boundary Layer Interaction and Flow Separation, " From: Proceedings of the 1962 Heat Transfer and Fluid Mechanics Institute. pp. 239-254, Printed by Stanford University Press, 1962.

23. Needham, D. A., and Stollery, J. L., "Boundary Layer Separation in Hypersonic Flow, "AIAA Paper No. 66-455, AIAA 4th Aerospace Sciences Meeting, Los Angeles, California June 27-29, 1966.

24. Holden, M.S., "Theoretical and Experimental Studies of Laminar Flow Separation on Flat Plate-Wedge Compression Surfaces in the Hypersonic Strong Interaction Regime, "Cornell Aeronautical Laboratory Report No. AF-1894-A-2, May 1967.

25. Lees, L. and Reeves, B. L., "Supersonic Separated and Reattaching Laminar Flows: 1. General Theory and Application to Boundary-Layer Shock-Wave Interactions, "AIAA Journal, Vol. 2, No. 11 November 1964.

26. Townsend, J. C., "Effects of Leading-Edge Bluntness and Ramp Deflection Angle on Laminar Boundary-Layer Separation in Hypersonic Flow," NASA TN D-3290, February, 1966.

27. Graham, W. J., and Vas, I. E., "An Experimental Investigation of the Separation of a Hypersonic Boundary Layer on a Flat Plate, "Princeton University Report PDAE Rept. 631, February, 1966.

28. Pinckney, S. Z., "Semiempirical Method for Predicting Effects of Incident-Reflecting Shocks on the Turbulent Boundary Layer, "NASA TN D-3209, October, 1965.

TABLE I

INSTRUMENTATION LOCATIONS FOR FLAT PLATE RAMP-MODEL C
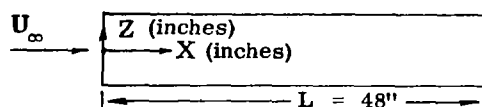
Code

P - Static Pressure

T - Temperature or Heat Flux Rate

Instrument		X	Z	Instrument		X	Z	Instrument		X	Z
1	P	1.50	0	42	P	29.47	-0.875	83	P	11.60	0
2	P	4.00	0	43	P	30.00	-0.875	84	P	11.80	0
3	P	6.06	0	44	P	30.53	-0.875	85	P	12.20	0
4	P	8.00	0	45	P	31.00	0	86	P	12.40	0
5	P	10.00	0	46	P	31.50	0	87	P	12.60	0
6	P	12.00	0	47	P	32.00	0	88	P	13.00	0
7	P	13.75	0	48	P	32.50	0	89	P	14.50	0
8	P	14.38	-0.875	49	P	33.00	0	90	P	22.20	0
9	P	15.00	0	50	P	33.62	-0.875	91	P	22.80	0
10	P	15.56	0	51	P	34.25	0	92	P	24.00	0
11	P	16.13	+0.500	52	P	34.81	0	93	T	3.00	0
12	P	16.13	0	53	P	35.38	+0.500	94	T	5.00	0
13	P	16.13	-0.500	54	P	35.38	0	95	T	7.00	0
14	P	16.63	-0.875	55	P	35.38	-0.500	96	T	9.00	0
15	P	17.13	-0.875	56	P	35.88	-0.875	97	T	10.00	+0.625
16	P	17.56	-0.875	57	P	36.38	-0.875	98	T	11.00	+0.625
17	P	18.00	0	58	P	36.81	-0.875	99	T	12.00	+0.625
18	P	18.50	0	59	P	37.25	0	100	T	13.00	+0.625
19	P	19.00	0	60	P	37.25	0	101	T	15.00	+0.625
20	P	19.50	-0.875	61	P	38.25	0	102	T	18.00	+0.625
21	P	20.00	-0.875	62	P	38.75	-0.875	103	T	20.00	+0.625
22	P	20.50	-0.875	63	P	39.25	-0.875	104	T	22.00	+1.250
23	P	21.00	0	64	P	42.00	0	105	T	23.00	+0.625
24	P	21.50	0	65	P	43.00	0	106	T	24.00	+1.250
25	P	22.00	0	66	P	44.00	0	107	T	25.00	+1.250
26	P	22.50	0	67	P	45.03	0	108	T	26.50	+0.625
27	P	23.00	0	68	P	46.00	0	109	T	28.00	+0.625
28	P	23.38	0	69	P	47.00	0	110	T	29.00	+0.625
29	P	23.75	0	70	T	2.44	+0.625	111	T	30.00	0
30	P	24.38	-0.875	71	T	5.25	+0.625	112	T	32.00	+0.625
31	P	25.03	0	72	T	9.50	+0.625	113	T	34.00	+0.625
32	P	25.56	0	73	T	16.50	+0.625	114	T	38.00	+0.625
33	P	26.12	+0.500	74	T	21.00	+0.625	115	T	22.00	+0.625
34	P	26.12	0	75	T	24.00	+0.625	116	T	24.50	+0.625
35	P	26.12	-0.500	76	T	27.00	+0.625	117	P	33.60	0
36	P	26.62	-0.875	77	T	30.00	+0.625	118	P	24.50	0
37	P	27.13	-0.875	78	T	33.00	+0.625	119	P	11.20	0
38	P	27.57	-0.875	79	T	36.00	+0.625	120	T	23.60	+0.625
39	P	28.00	0	80	T	39.00	+0.625	121	T	26.50	+1.250
40	P	28.50	0	81	P	11.00	0				
41	P	29.00	0	82	P	11.40	0				

TABLE II

INSTRUMENTATION LOCATIONS FOR COMPRESSION RAMP-MODEL E-3
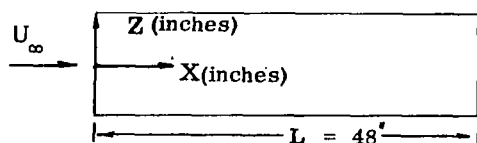
Code

P - Static Pressure

T - Temperature or Heat Flux Rate

A = 2.563 in.

Instrument		X-A	Z	Instrument		X-A	Z	Instrument		X-A	Z
2	P	1.19	0	35	P	23.62	-0.50	68	P	39.06	0
3	P	3.43	0	36	P	24.12	-0.880	69	P	39.56	0
4	P	5.43	0	37	P	24.62	-0.880	70	P	40.06	0
5	P	7.43	0	38	P	25.06	-0.880	71	P	40.56	0
6	P	9.43	0	39	P	25.50	0	72	P	41.06	0
7	P	11.43	-0.880	40	P	26.00	0	73	P	41.56	0
8	P	11.94	-0.880	41	P	26.50	0	74	P	42.06	0
9	P	12.43	0	42	P	27.00	-0.880	75	P	42.57	0
10	P	12.94	0	43	P	27.50	-0.880	76	P	43.08	0
11	P	13.56	+0.500	44	P	28.00	-0.880	77	P	43.58	0
12	P	13.56	0	45	P	28.50	0	78	P	44.10	0
13	P	13.56	-0.500	46	P	29.00	0	79	P	44.62	0
14	P	14.06	-0.880	47	P	29.50	0	80	P	45.12	0
15	P	14.56	-0.880	48	P	30.00	0	81	T	6.50	0
16	P	15.00	-0.880	49	P	30.50	-0.880	82	T	11.00	0
17	P	15.44	0	50	P	31.00	-0.880	83	T	17.50	0
18	P	15.94	0	51	P	31.53	0	84	T	28.00	+0.625
19	P	16.44	0	52	P	32.03	0	85	T	30.00	+0.625
20	P	16.94	-0.880	53	P	32.50	+0.500	86	T	31.00	+0.625
21	P	17.44	-0.880	54	P	32.50	0	87	T	32.00	+0.625
22	P	17.94	-0.880	55	P	32.50	-0.500	88	T	33.00	+0.625
23	P	18.44	0	56	P	33.00	-0.880	89	T	34.00	+0.625
24	P	18.94	0	57	P	33.50	-0.880	90	T	35.00	+0.625
25	P	19.44	0	58	P	34.03	-0.880	91	T	36.00	+0.625
26	P	19.94	0	59	P	34.56	0	92	T	37.00	+0.625
27	P	20.44	0	60	P	35.06	0	93	T	38.00	+0.625
28	P	20.94	0	61	P	35.56	0	94	T	39.00	+0.625
29	P	21.44	-0.880	62	P	36.06	-0.880	95	T	40.00	+0.625
30	P	21.94	-0.880	63	P	36.56	-0.880	96	T	22.00	0
31	P	22.47	0	64	P	37.06	-0.880	97	T	43.00	+0.625
32	P	22.97	0	65	P	37.56	0	98	T	26.00	+0.625
33	P	23.62	+0.50	66	P	38.06	0	99	T	28.00	0
34	P	23.62	0	67	P	38.56	0	100	T	36.50	0
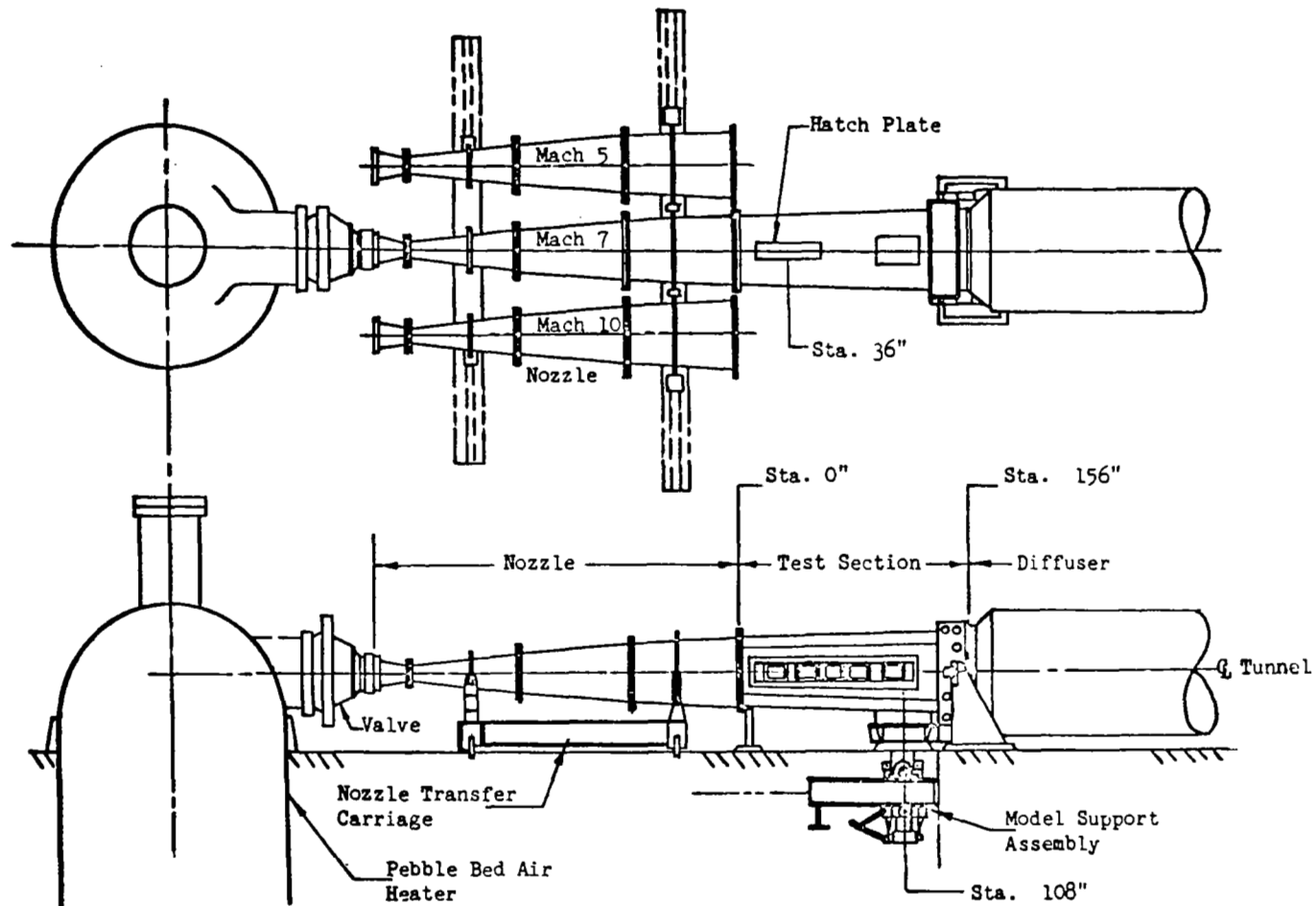
Figure 1. SCHEMATIC OF NASA-AMES 3.5 FOOT HYPERSONIC WIND TUNNEL
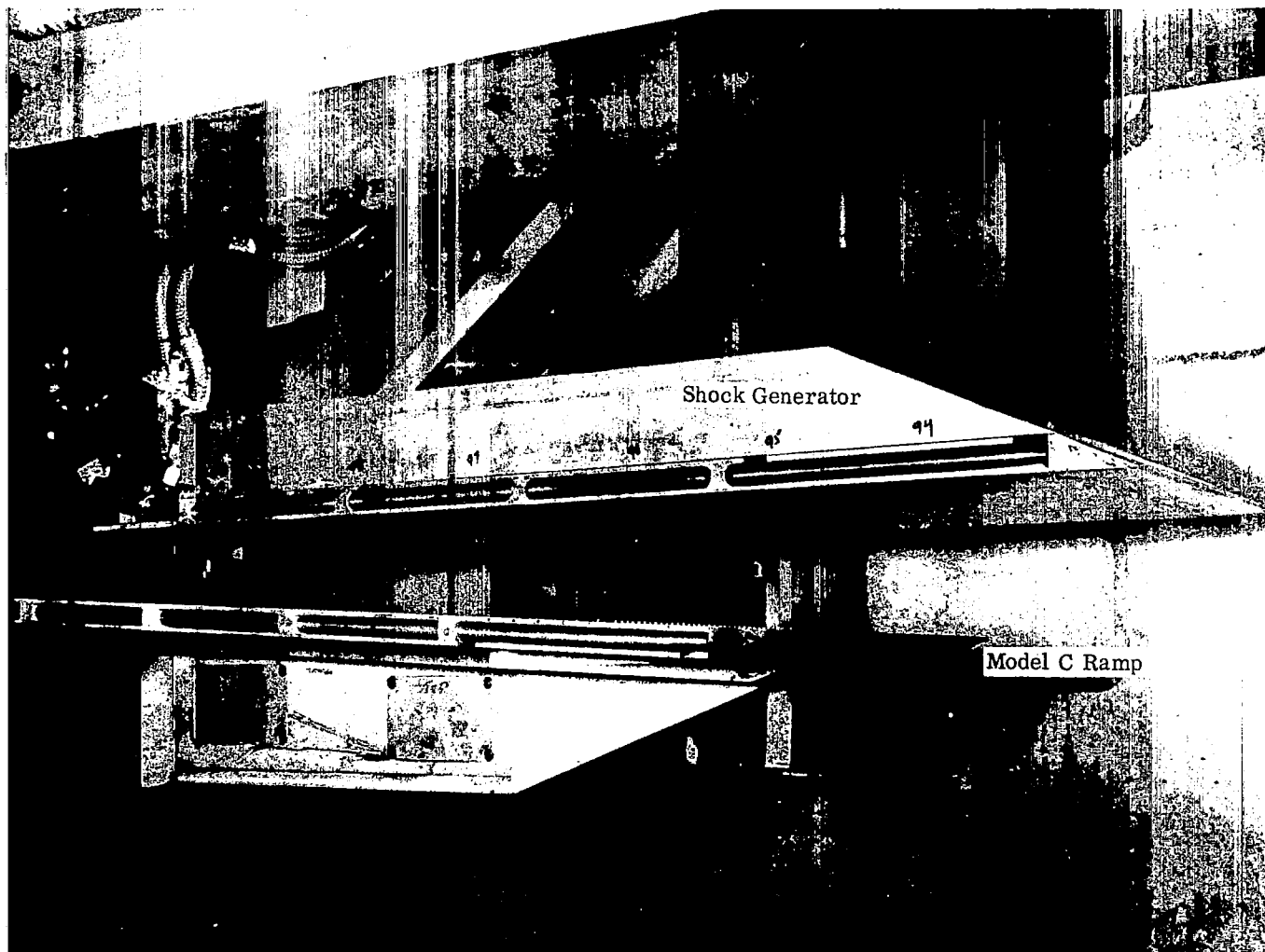
Figure 2. FLAT PLATE MODEL, C, WITH SHOCK GENERATOR,
.063 in. LEADING EDGE RADIUS.

0.188 in. R

B-1 Leading Edge

0.063 in. R

B-2 Leading Edge

Shock Generator

Model C Ramp

α_g

$\alpha = 3°$

U_∞

$L = 48$ in.
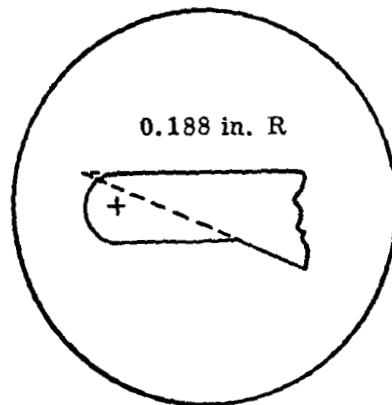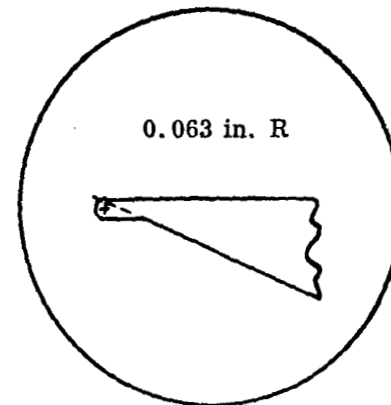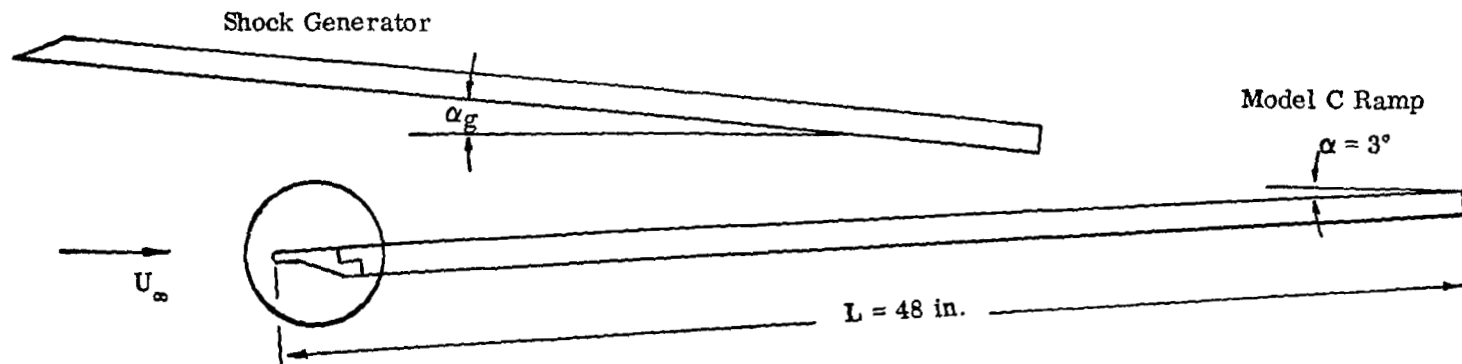
Figure 3. SCHEMATIC OF FLAT PLATE MODEL, C,
WITH SHOCK GENERATOR.
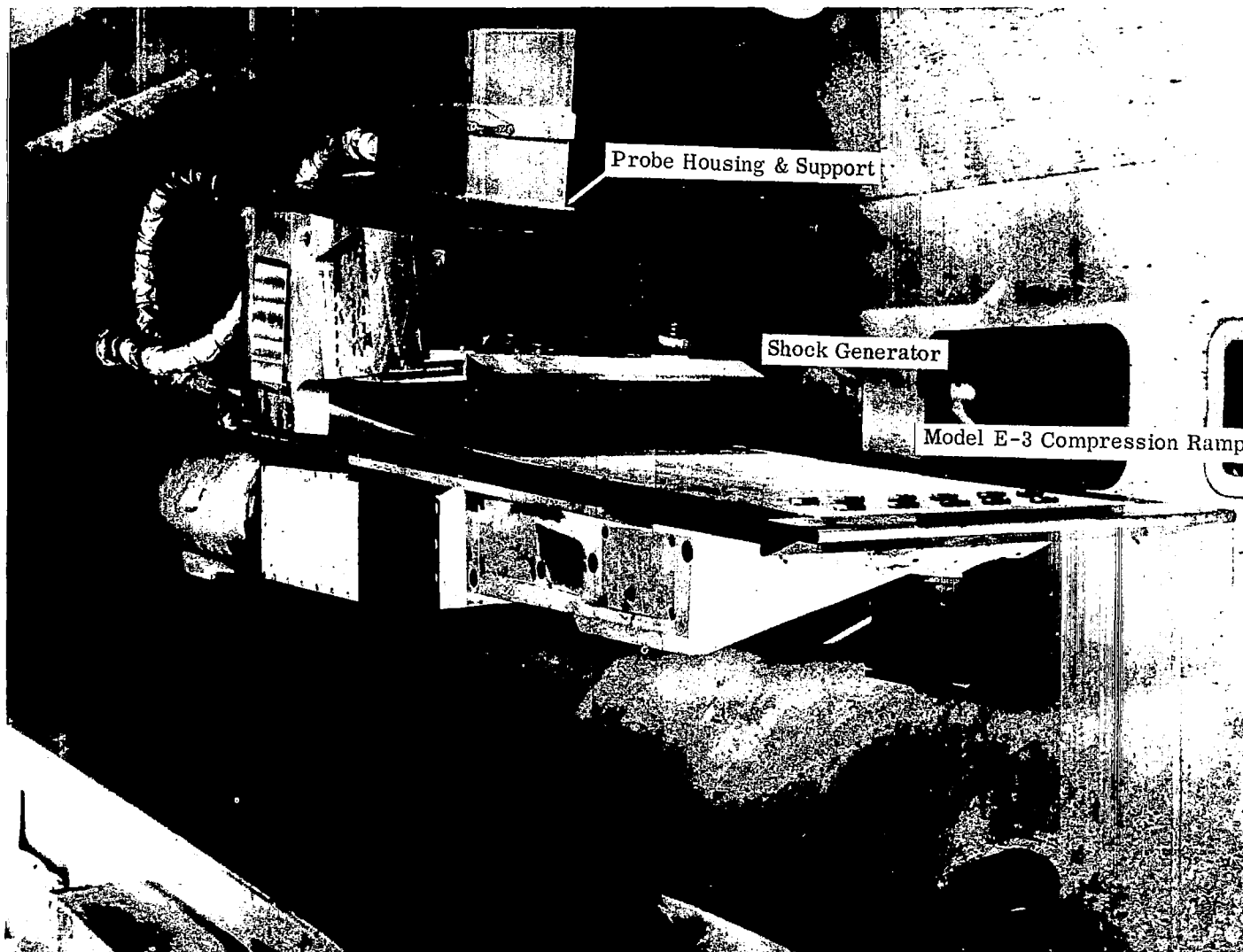
Figure 4. COMPRESSION SURFACE MODEL, E-3, WITH SHOCK GENERATOR,
.188 in. LEADING EDGE RADIUS.

Model E-3 Compression Ramp Coordinates

(inches)

X	$\bar{Y}$	X	$\bar{Y}$
0	0	29	1.926
10	.524	30	2.038
11	.578	31	2.156
12	.634	32	2.280
13	.692	33	2.408
14	.752	34	2.540
15	.813	35	2.676
16	.874	36	2.816
17	.936	37	2.960
18	1.000	38	3.108
19	1.066	39	3.260
20	1.136	40	3.414
21	1.210	41	3.572
22	1.286	42	3.734
23	1.366	43	3.900
24	1.450	44	4.070
25	1.536	45	4.244
26	1.626	46	4.422
27	1.720	47	4.604
28	1.820	48	4.790
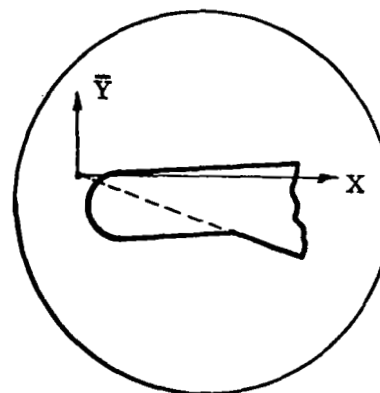
Coordinate System
(0, 0) -- Sharp Leading Edge

Shock Generator   Model E-3 Compression Ramp
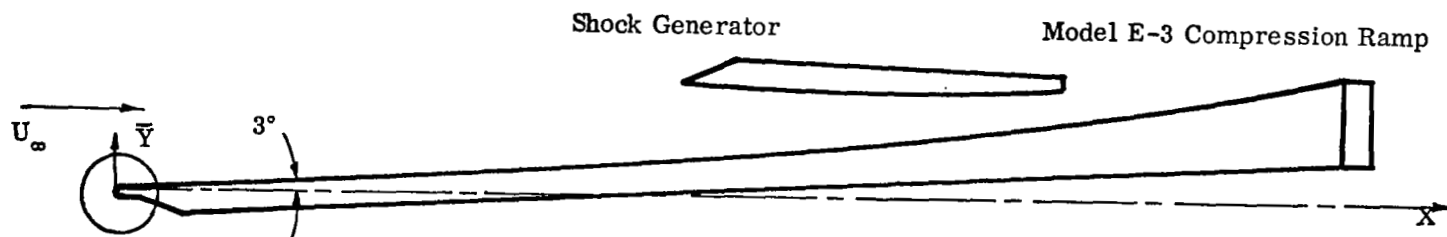
Figure 5. SCHEMATIC OF COMPRESSION SURFACE MODEL, E-3,
WITH SHOCK GENERATOR.
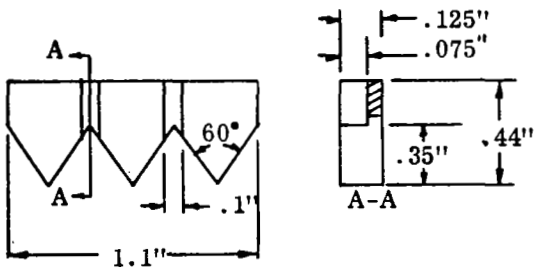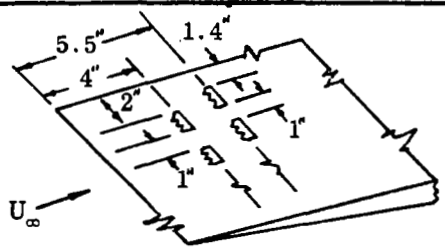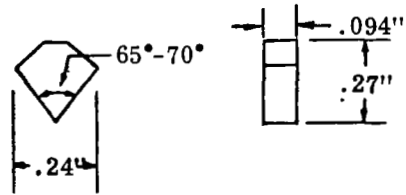
Conf. No.	Type	Distribution
1		First row projected .150 in. above the model surface Second row projected .175 in. above the model surface
2	Same as 1	Along X = 4in. and projected .150 in. above the plate surface. Nominal lateral spacing of 0.40 in between elements.
3		Along X = 7in. trips spaced .375 in. from center to center
4		Along X = 4 in. trips spaced .375 in. from center to center and projected .065 in. above the plate surface.

Figure 6. BOUNDARY LAYER TRIP CONFIGURATIONS.
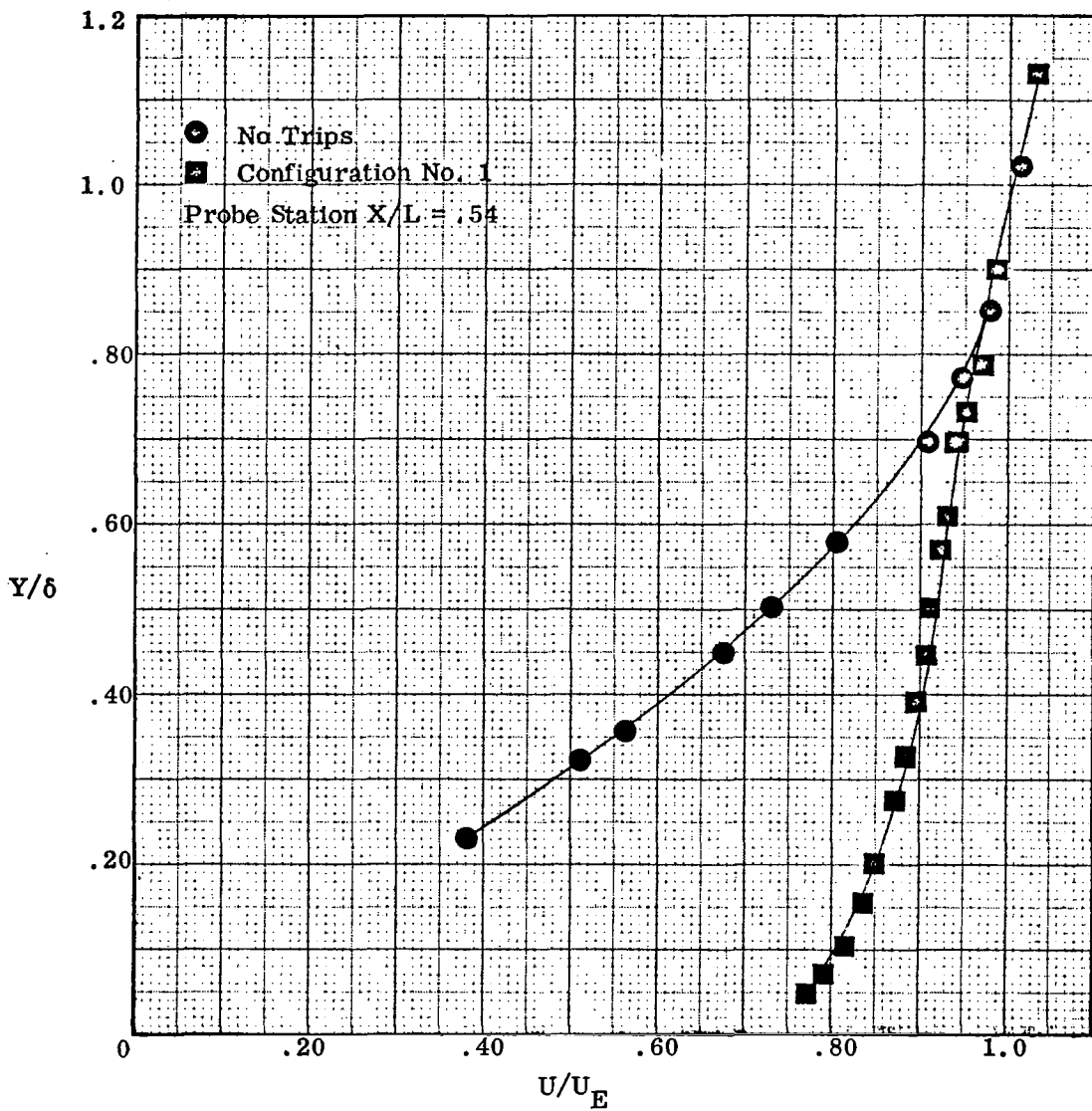
Figure 7.   COMPARISON OF TRIP EFFECTIVENESS ON COMPRESSION SURFACE,
.188 in. LEADING EDGE RADIUS
$M_\infty = 10.55$, Re/ft = 2 x 10^6

44
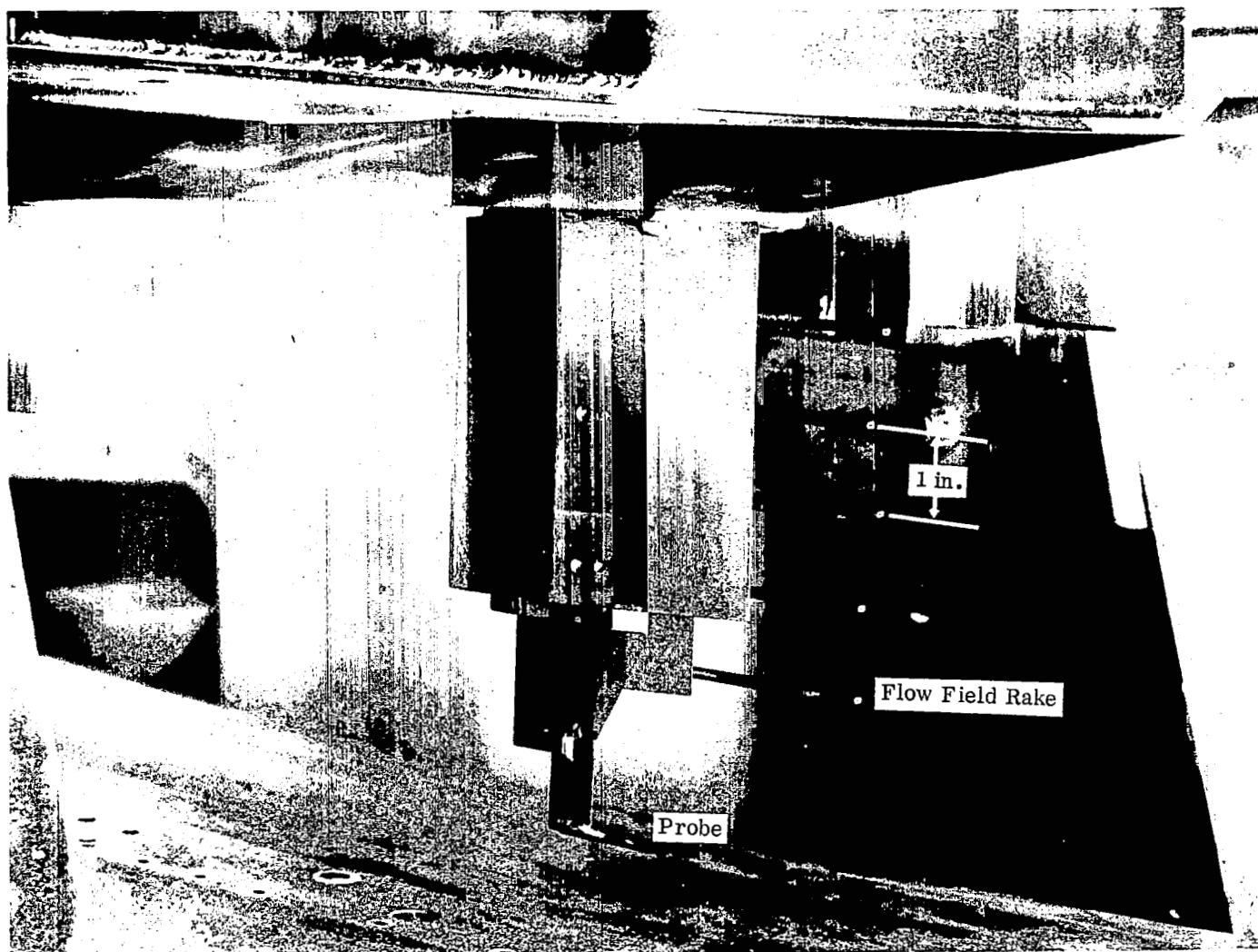
Figure 8. BOUNDARY LAYER PROBE AND FLOW FIELD RAKE.
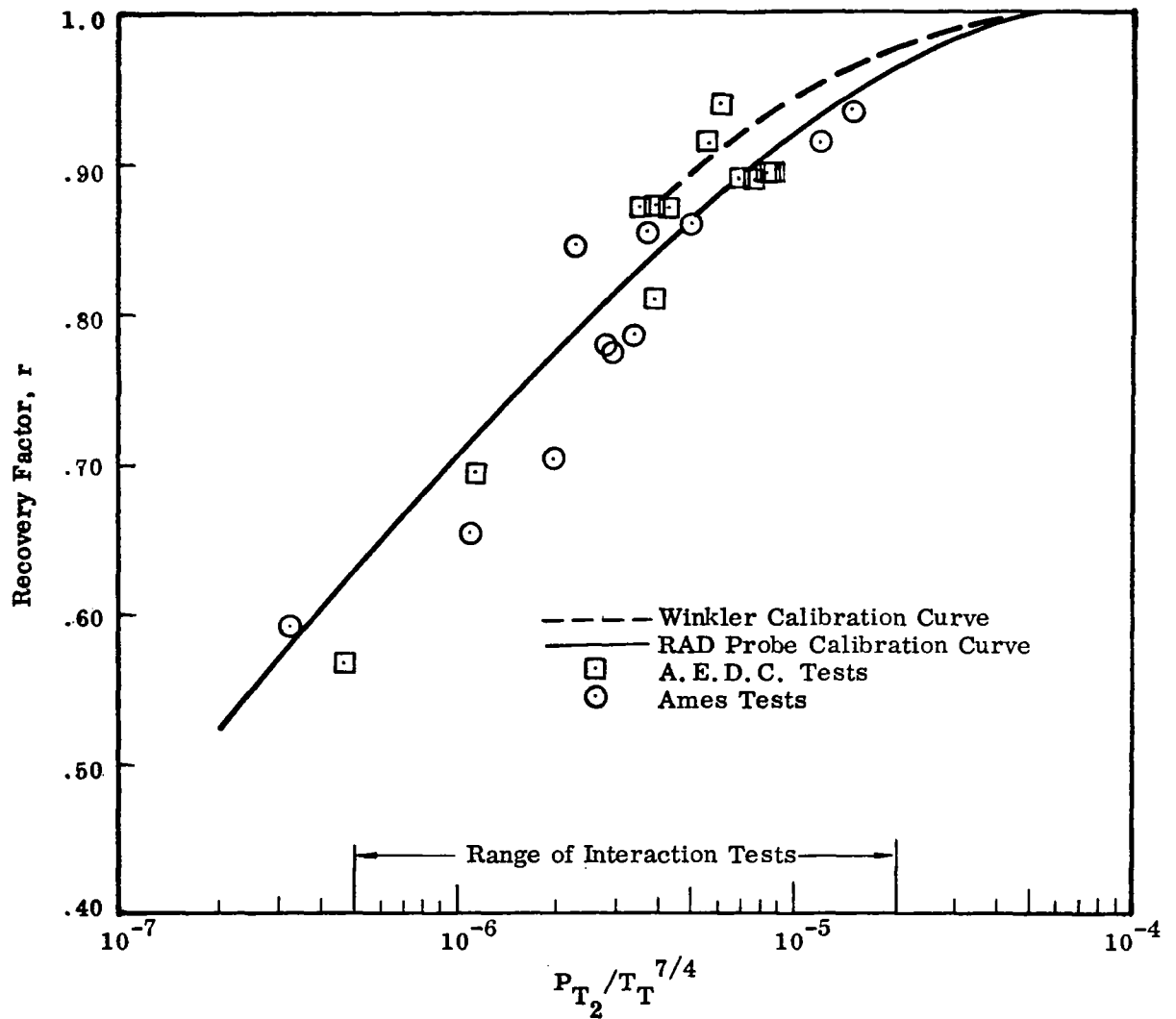
Figure 9. TEMPERATURE PROBE CALIBRATION CURVE.
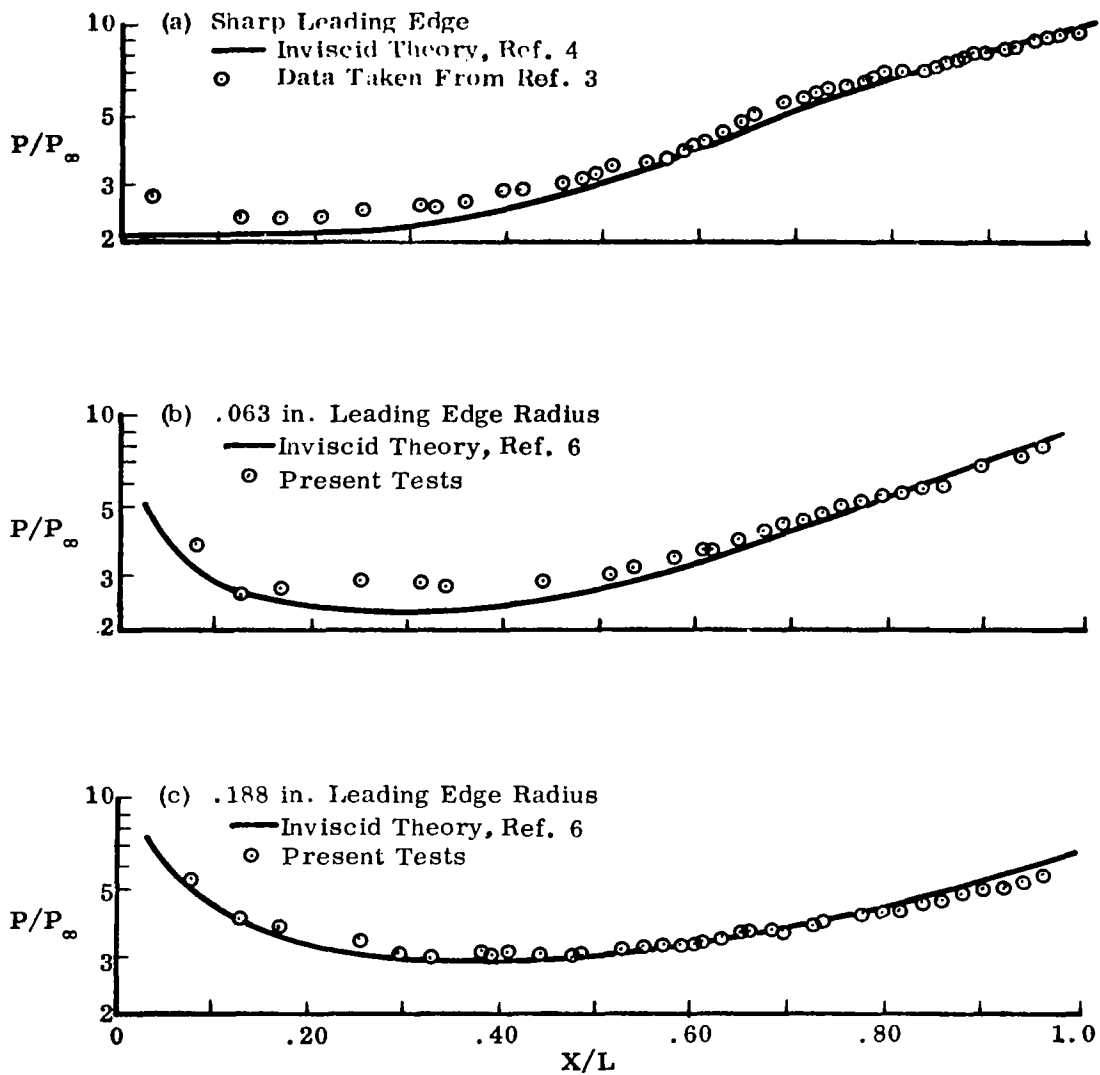
Figure 10. SURFACE PRESSURE DISTRIBUTION,

COMPRESSION SURFACE MODEL,

$M_\infty = 10.55$, Re/ft $= 2 \times 10^6$.
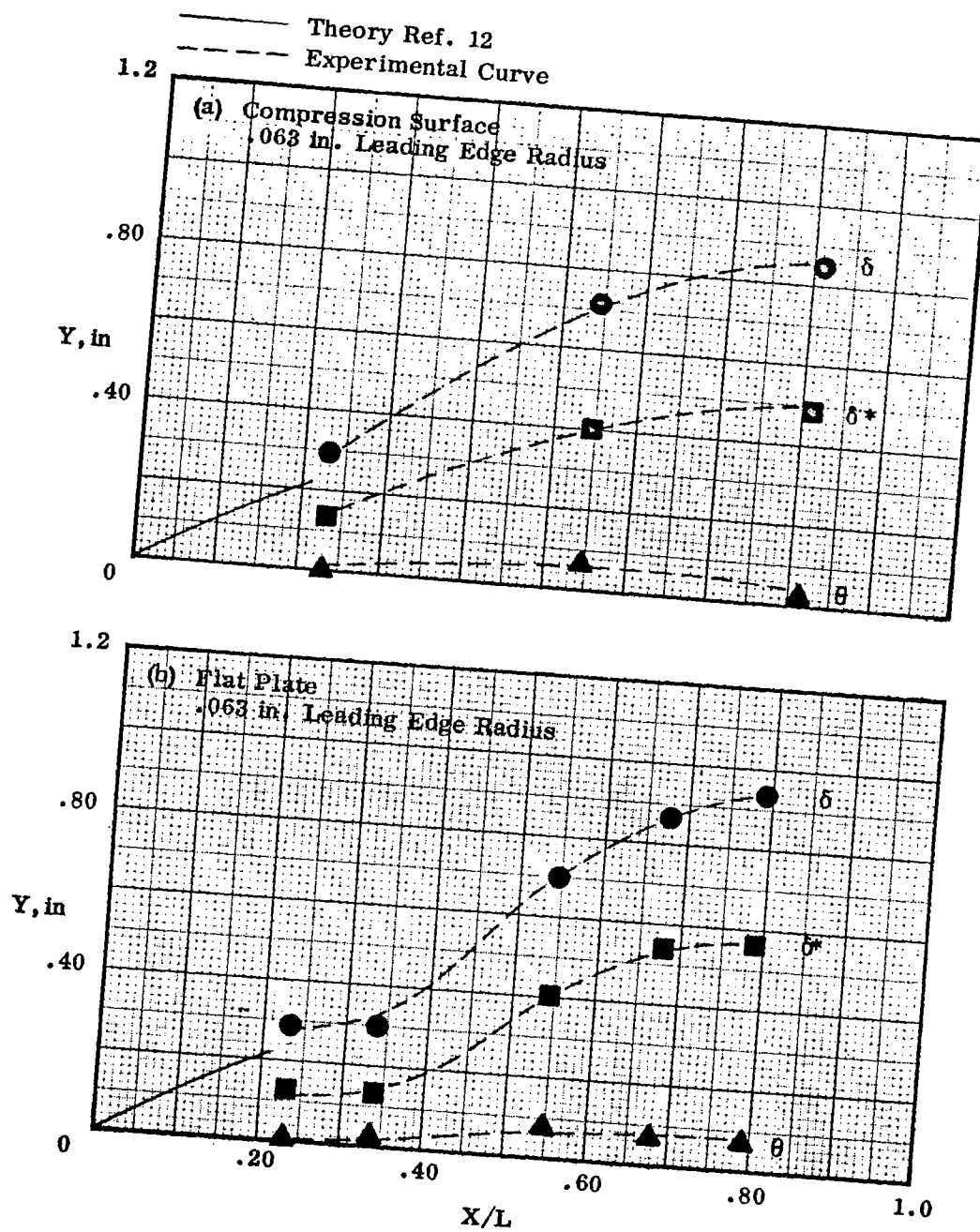
Figure 11. BOUNDARY LAYER GROWTH,
$M_\infty = 10.55$, $Re/ft = 2 \times 10^6$.

$\bullet$ - M_∞ = 7.4,   Re/ft = 2 x 10^6
$\Box$ - M_∞ = 10.55, Re/ft = 2 x 10^6
———— Inviscid Theory, M_∞ = 7.4, Ref. 6
— — — Inviscid Theory, M_∞ = 10.55, Ref. 6
— $\cdot$ — Inviscid + Viscous Theory, M_∞ = 10.55, Re/ft = 2 x 10^6, Present Study
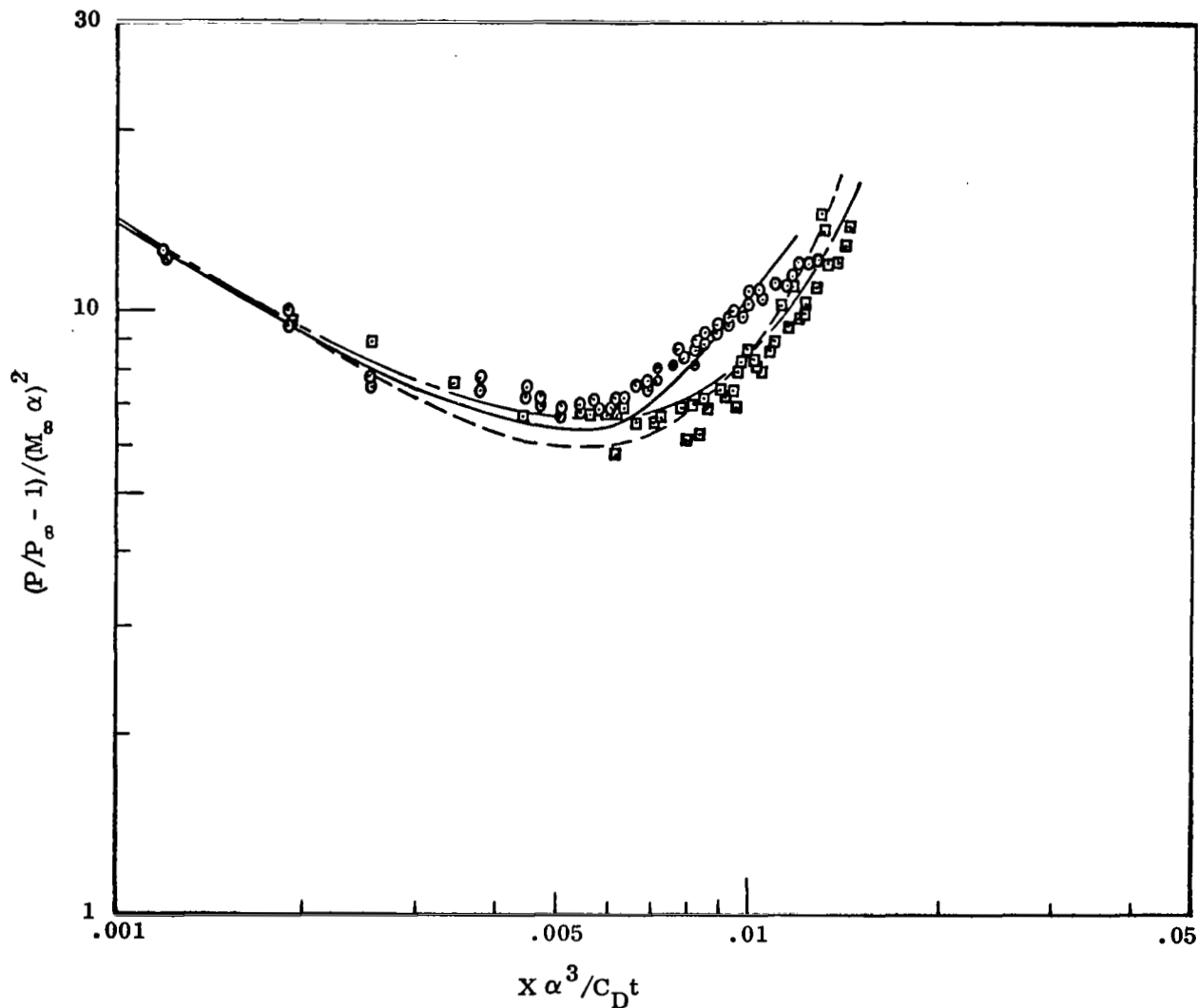
Figure 12. SURFACE PRESSURE CORRELATION,
COMPRESSION SURFACE,
.188 in. LEADING EDGE RADIUS.
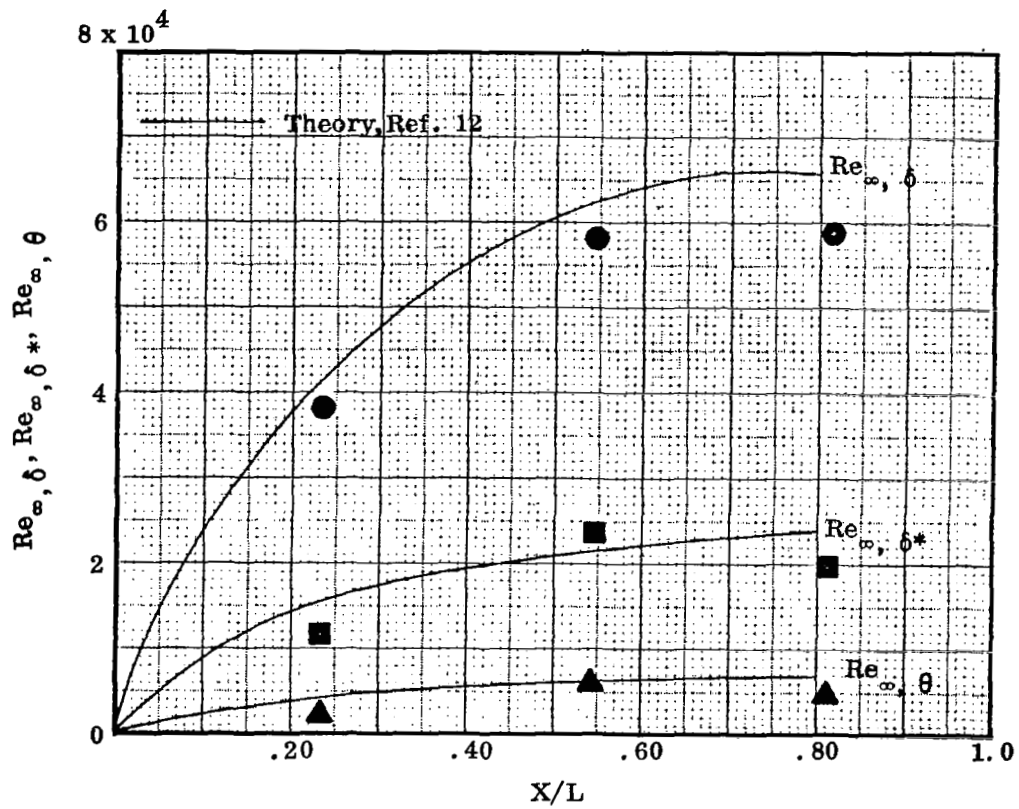
Figure 13. LAMINAR BOUNDARY LAYER GROWTH,
COMPRESSION SURFACE,
.188 in. LEADING EDGE RADIUS,
$M_\infty = 10.55$, $Re/ft = 2 \times 10^6$.
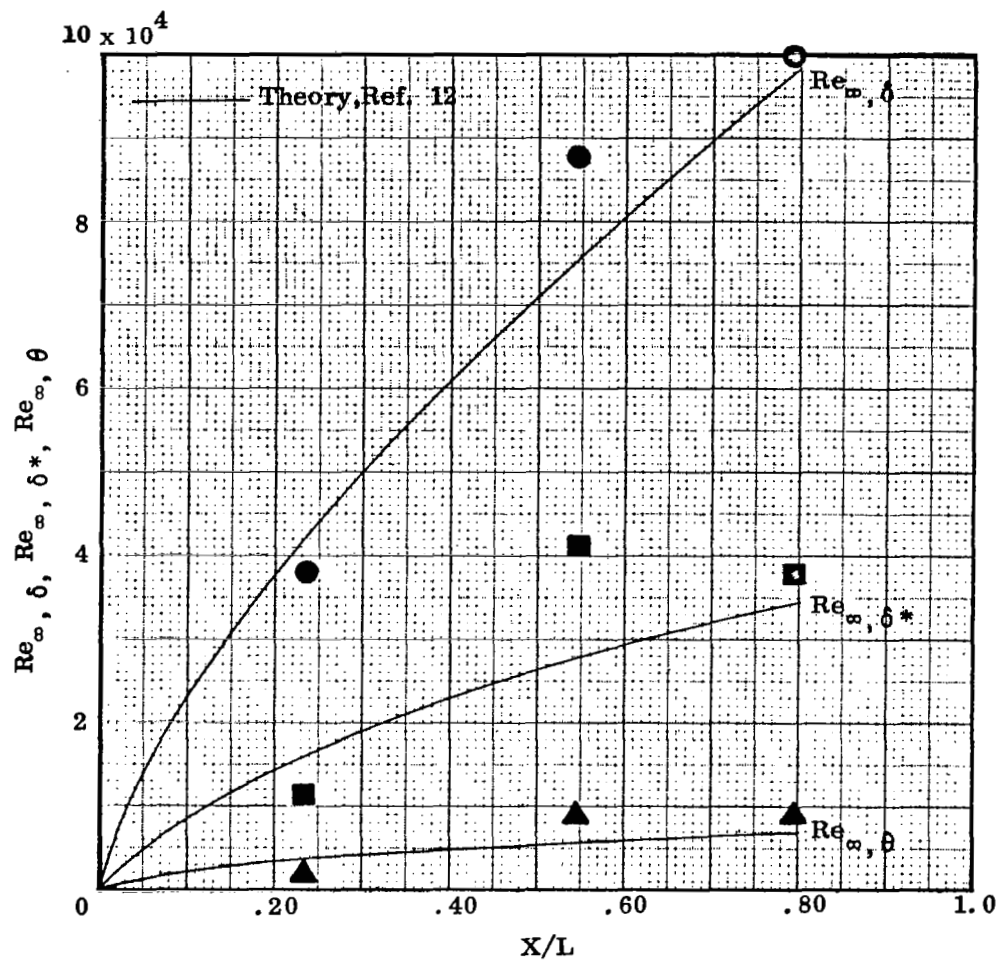
Figure 14. LAMINAR BOUNDARY LAYER GROWTH,
FLAT PLATE,
.188 in. LEADING EDGE RADIUS,
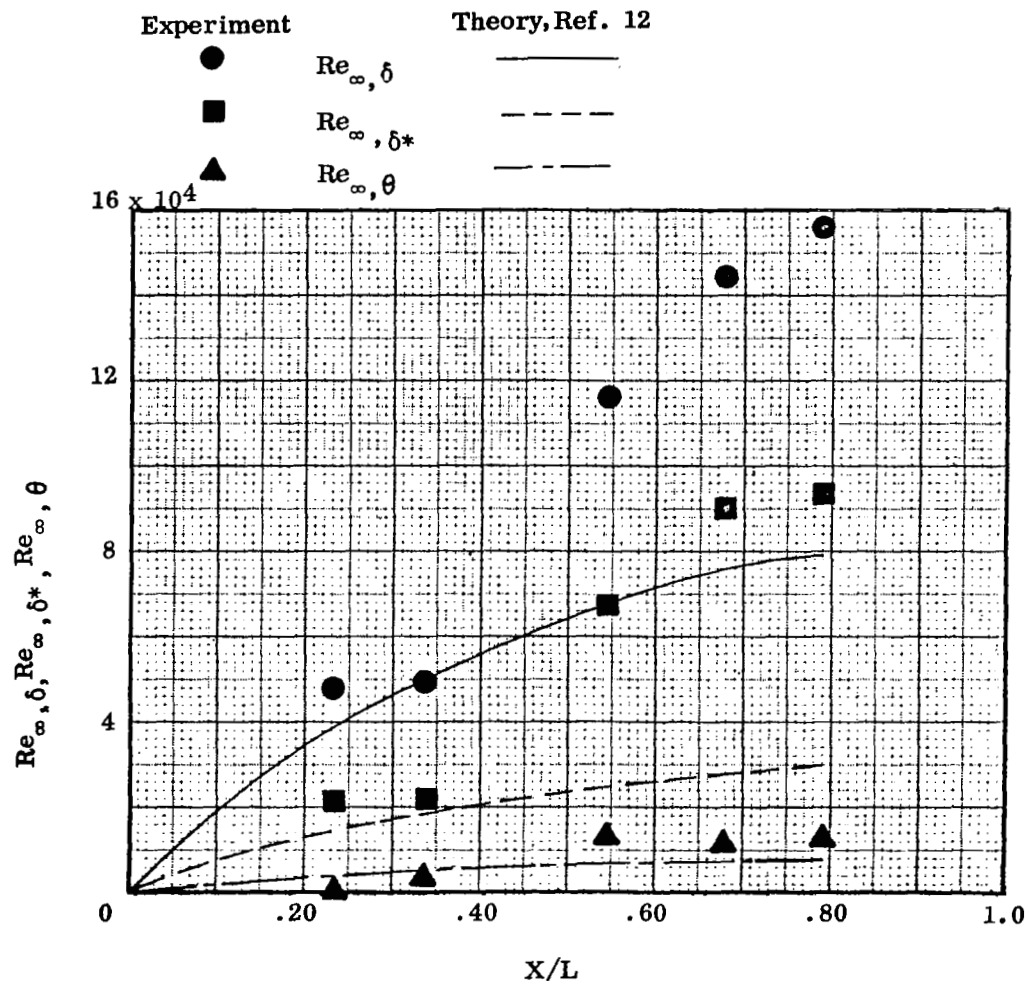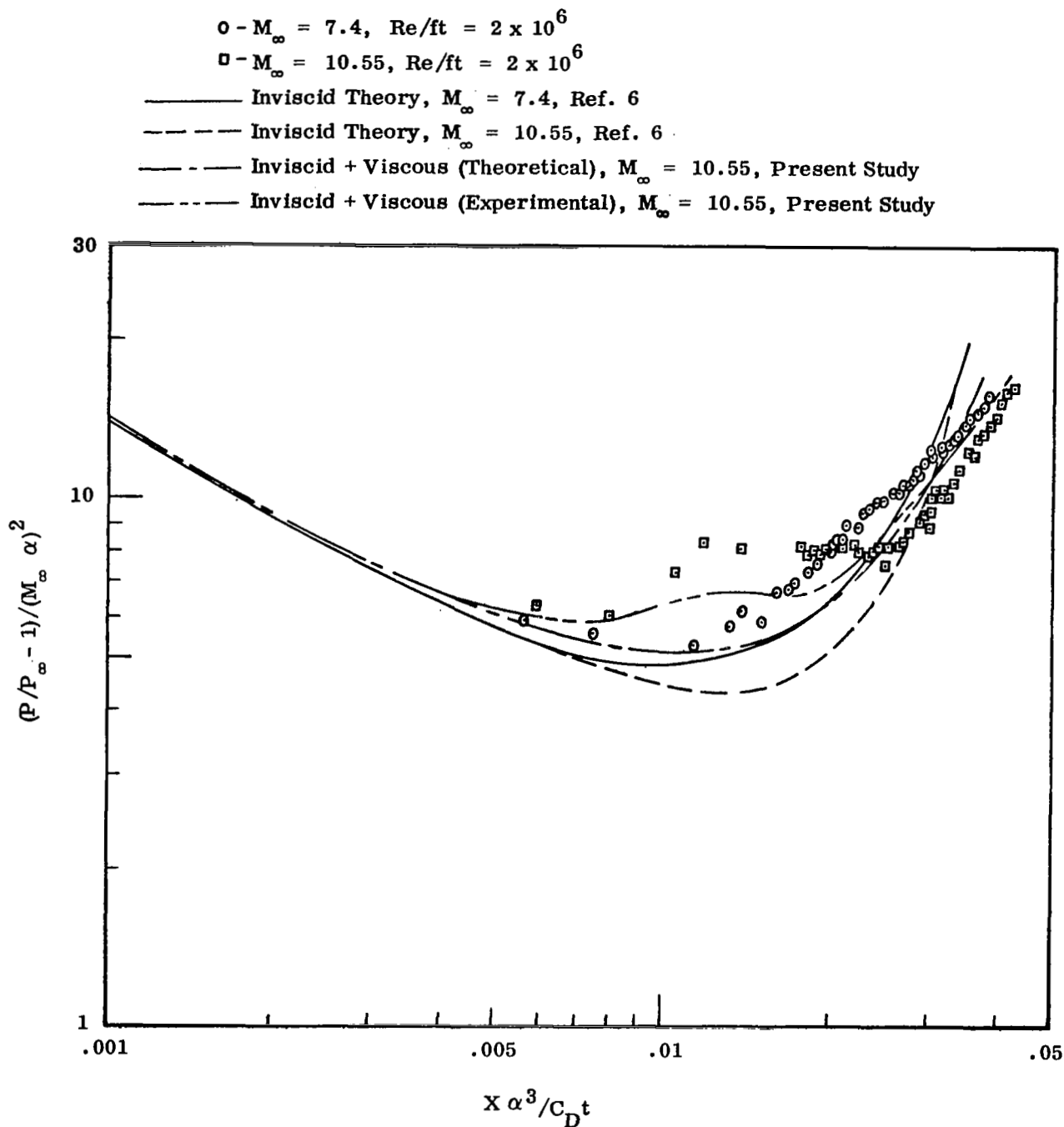$M_\infty = 10.55$, $Re/ft = 2 \times 10^6$.

51
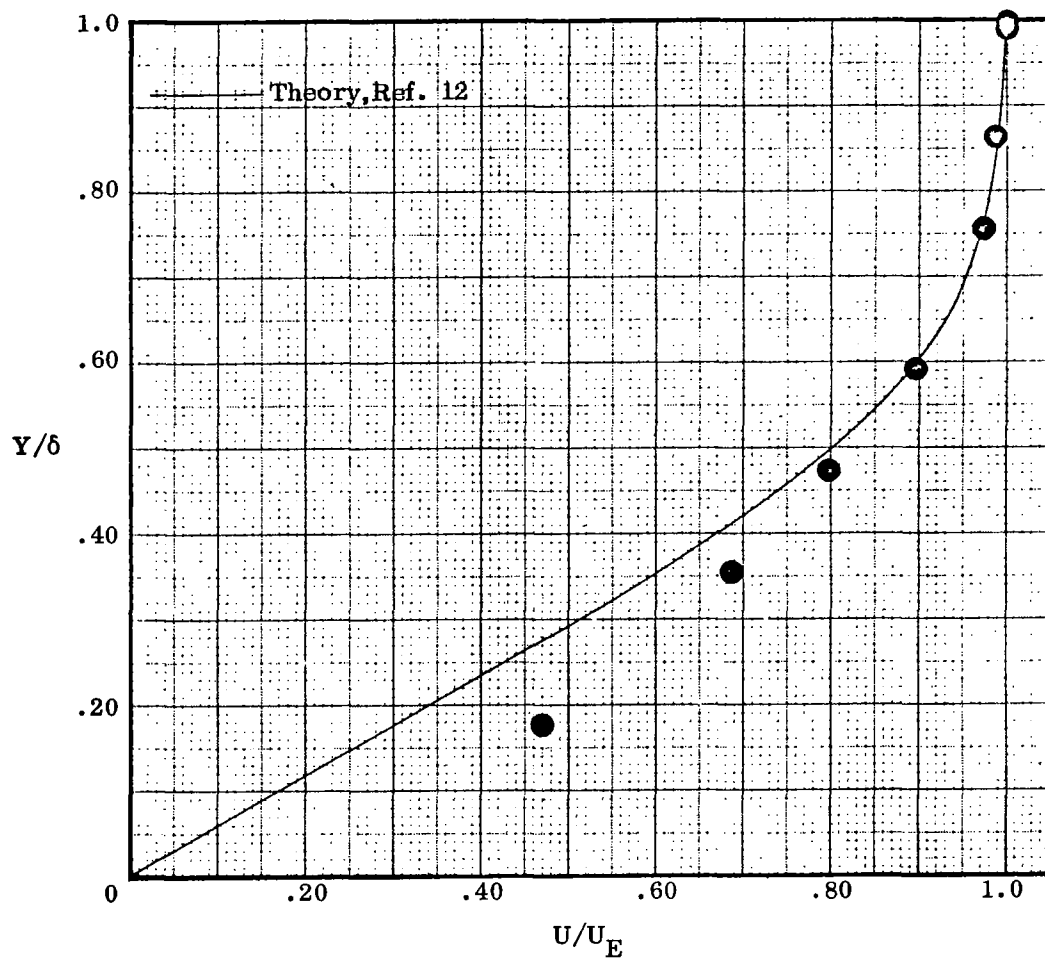
Figure 15. LAMINAR VELOCITY PROFILE,
COMPRESSION SURFACE,
.188 in. LEADING EDGE RADIUS,
PROBE STATION X/L = .813,
$M_\infty = 10.55$, $Re/ft = 2 \times 10^6$.

52
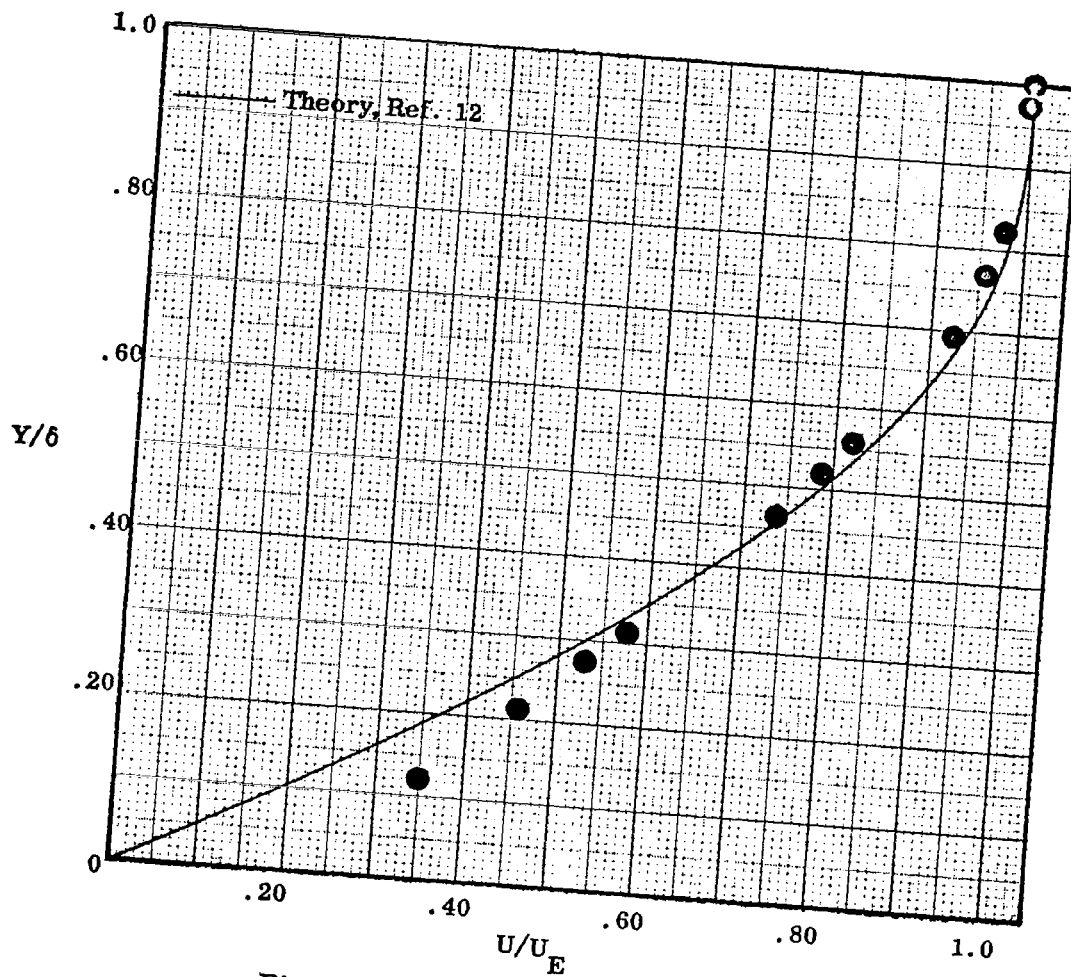
Figure 16. LAMINAR VELOCITY PROFILE,
FLAT PLATE,
.188 in. LEADING EDGE RADIUS,
PROBE STATION X/L = .79,
M_∞ = 10.55, Re/ft = 2 x 10^6.
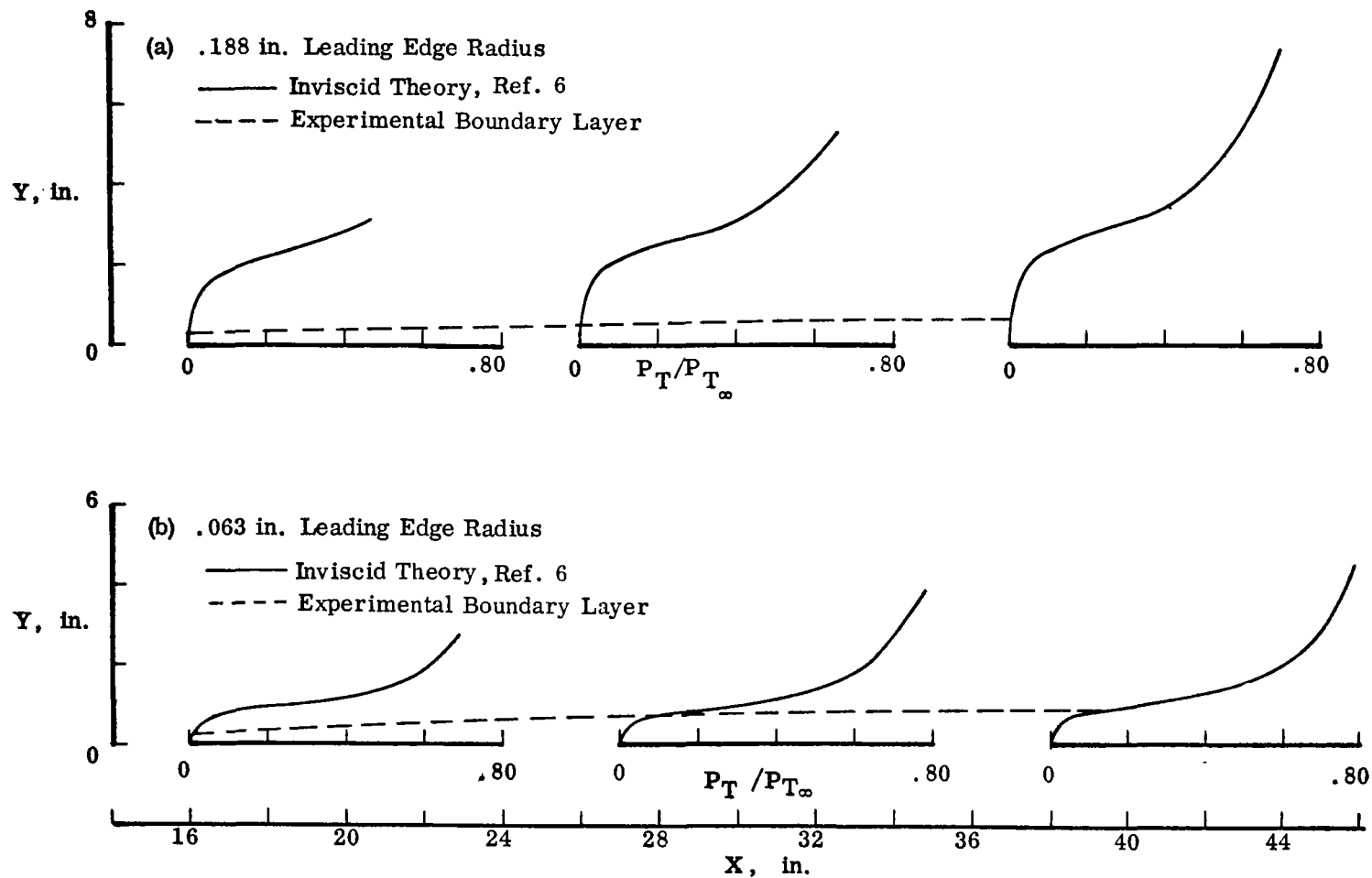
Figure 17. STAGNATION PRESSURE PROFILE DEVELOPMENT,

FLAT PLATE,

$M_\infty = 10.55$, Re/ft $= 2 \times 10^6$.

● .063 in. Leading Edge Radius ——— ⎫ Inviscid + Viscous Theory
■ .188 in. Leading Edge Radius — — — ⎭ Present Study
Experimental Curve ——— – ——
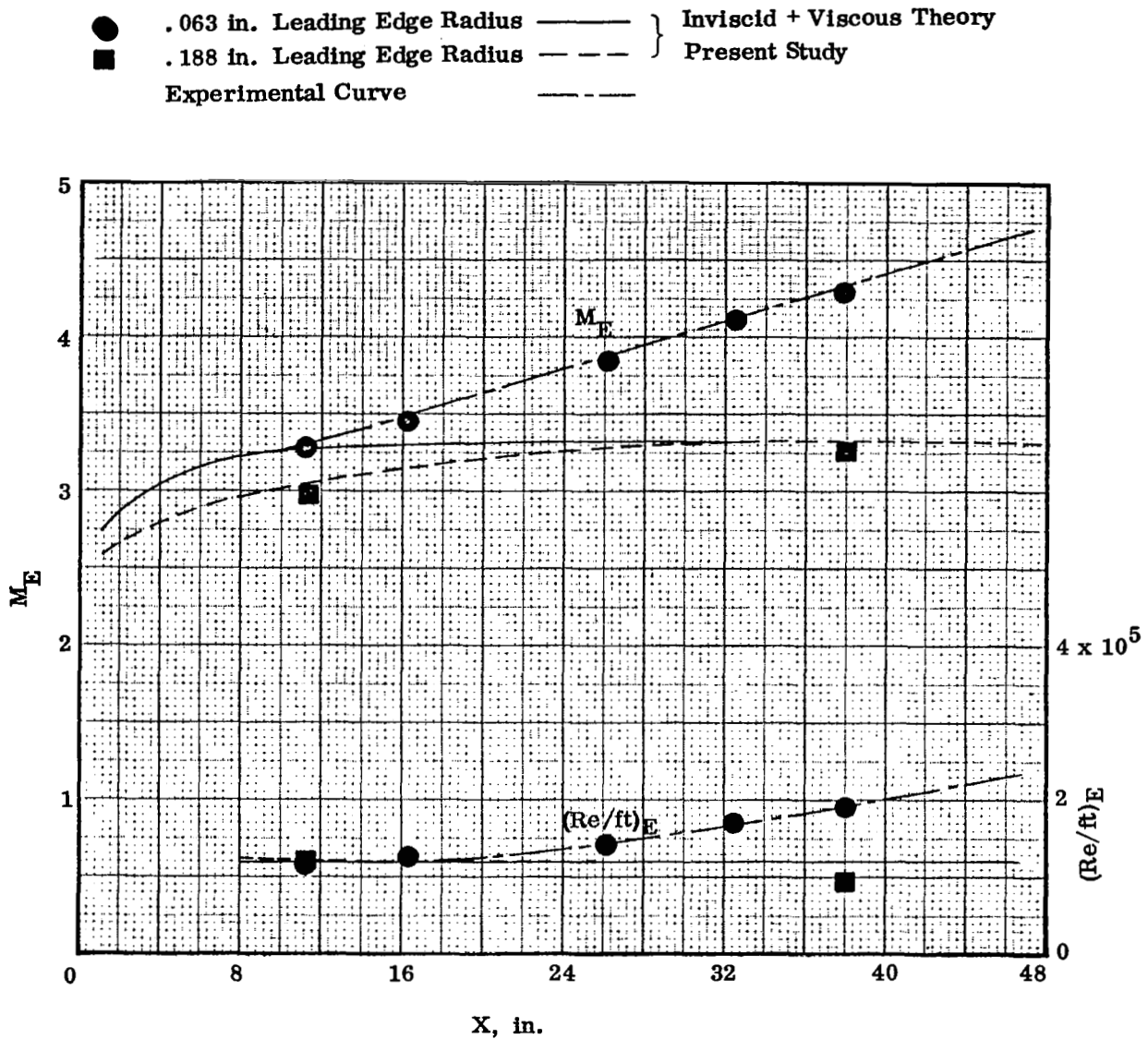
Figure 18. VARIATION OF BOUNDARY LAYER EDGE CONDITIONS,
FLAT PLATE,
$M_\infty = 10.55$, $Re/ft = 2 \times 10^6$.

Probe Stations

⊙ X/L = .232	⊙ X/L = .330
▢ X/L = .540	▢ X/L = .540
△ X/L = .790	△ X/L = .790

(a) .188 in. Leading Edge Radius

(b) .063 in. Leading Edge Radius

Y/δ

U/U_E

U/U_E
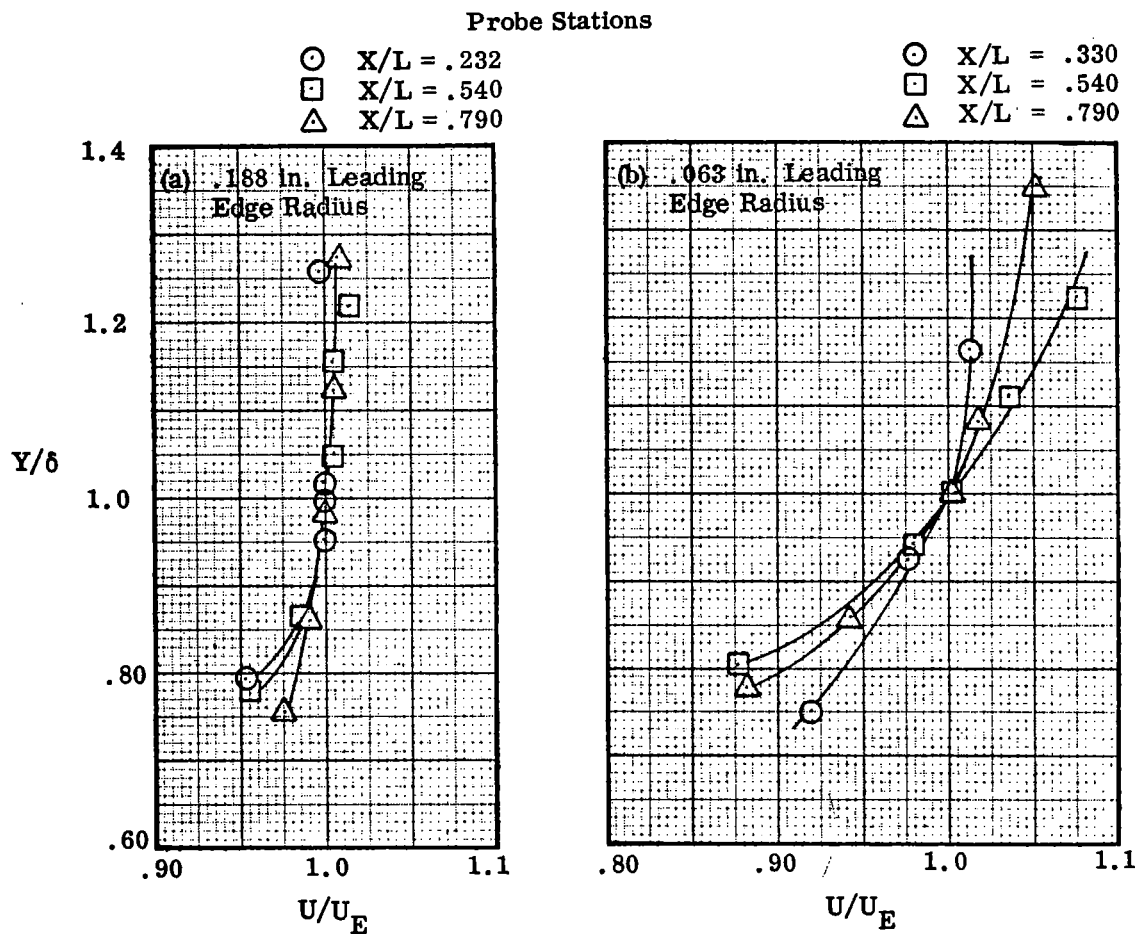
Figure 19. EFFECT OF BLUNTNESS ON VISCOUS-LAYER OUTER-EDGE VELOCITY GRADIENT,
FLAT PLATE,
$M_\infty = 10.55, Re/ft = 2 \times 10^6$.

56

(a) X/L = .33

(b) X/L = .54

(c) X/L = .79

Y/δ

1.0

.50

0

Theory, Ref. 12

Theory, Ref. 12

Theory, Ref. 12

$U/U_E = (Y/\delta)^{1/2}$

.50

1.0

0

.50

1.0

0

.50

1.0

U/U_E
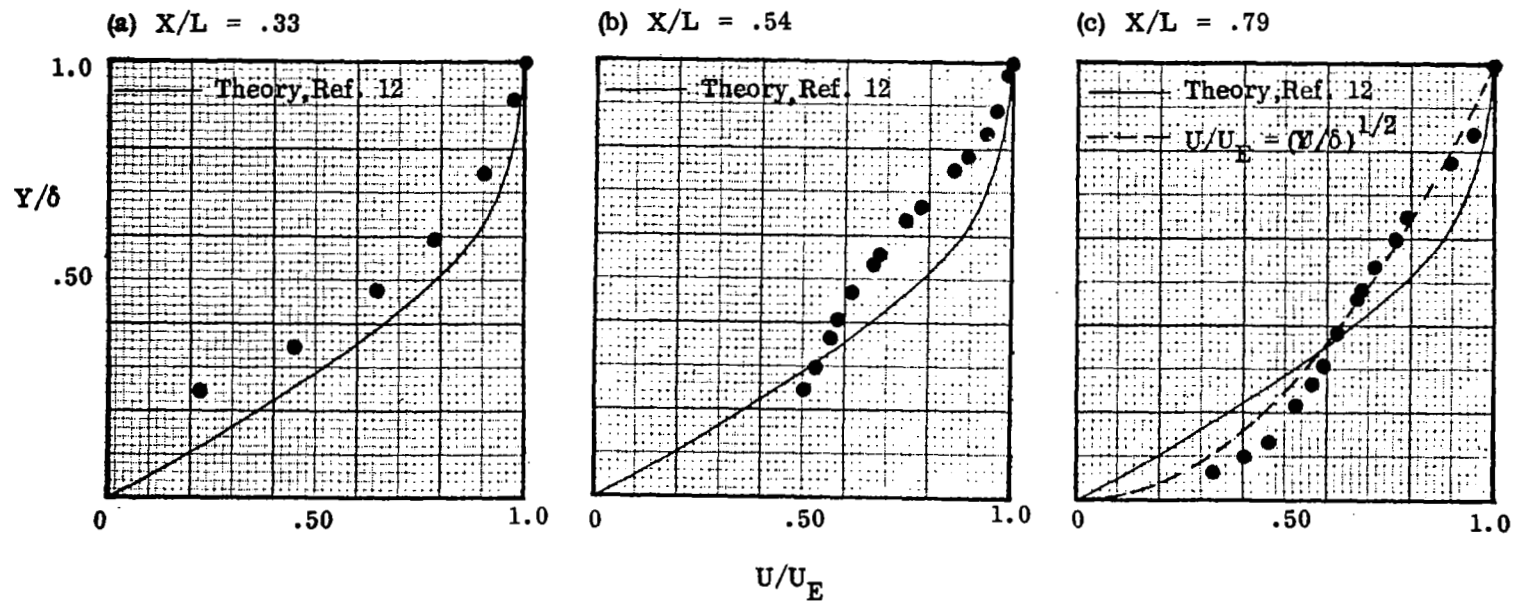
Figure 20. BOUNDARY LAYER PROFILE DEVELOPMENT,
FLAT PLATE, .063 in. LEADING EDGE RADIUS,
M_∞ = 10.55, Re/ft = 2 x 10^6.

Figure 21. BOUNDARY LAYER GROWTH,
FLAT PLATE,
.063 in. LEADING EDGE RADIUS,
M_∞ = 10.55, Re/ft = 2 x 10^6.

58

$o - M_\infty = 7.4$, Re/ft $= 2 \times 10^6$
$\square - M_\infty = 10.55$, Re/ft $= 2 \times 10^6$
——— Inviscid Theory, $M_\infty = 7.4$, Ref. 6
— — — Inviscid Theory, $M_\infty = 10.55$, Ref. 6
—— · —— Inviscid + Viscous (Theoretical), $M_\infty = 10.55$, Present Study
—— · · —— Inviscid + Viscous (Experimental), $M_\infty = 10.55$, Present Study

Figure 22. SURFACE PRESSURE CORRELATION,
COMPRESSION SURFACE,
.063 in. LEADING EDGE RADIUS
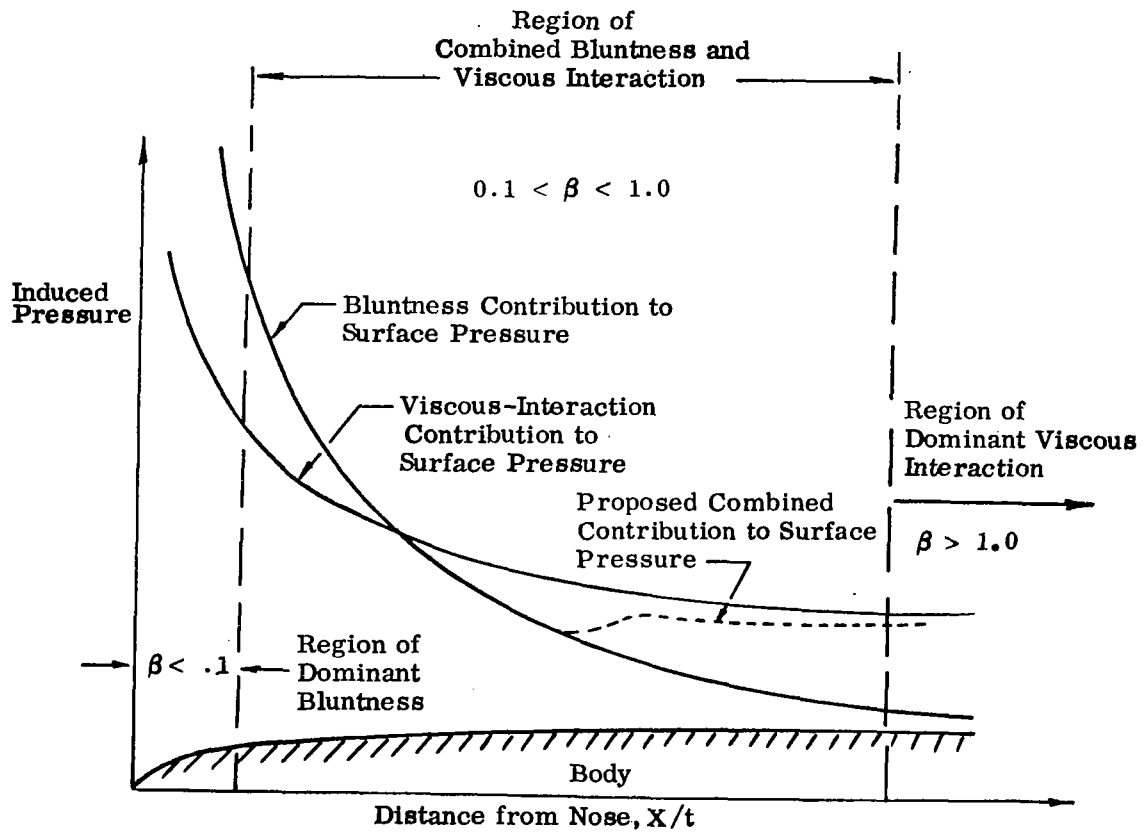
Figure 23. VISCOUS-INTERACTION AND BLUNTNESS CONTRIBUTIONS TO THE SURFACE PRESSURE DISTRIBUTION.

60

● Trip, Configuration No. 2, δ = .84 in.

■ No Trips, δ = .72 in.

X/L = .54
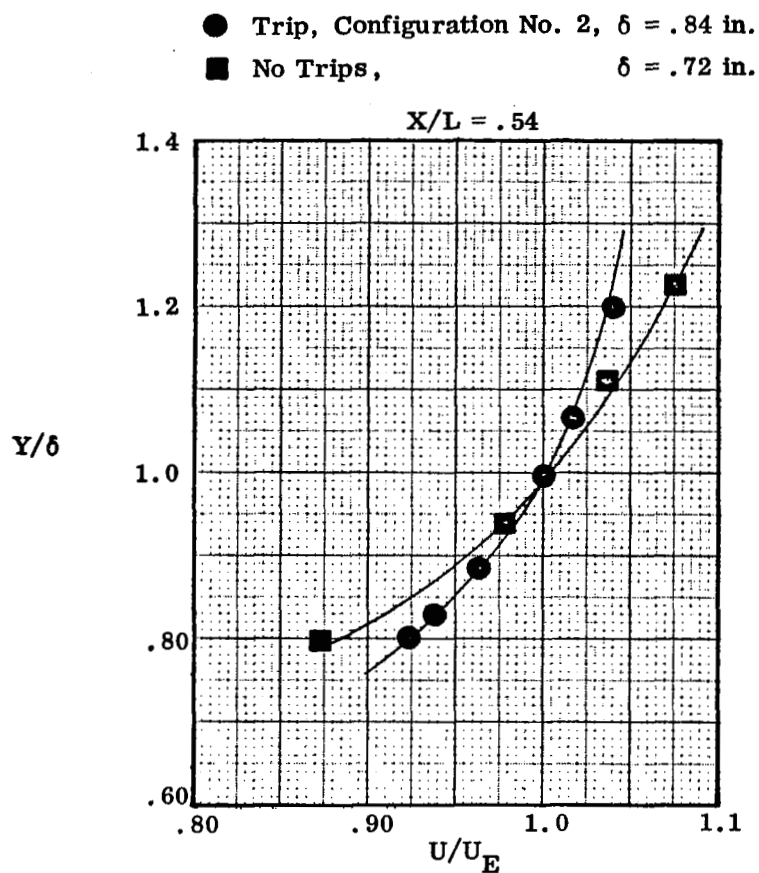
Figure 24. EFFECT OF TRIPS ON OUTER EDGE VELOCITY GRADIENT,
FLAT PLATE, .063 in. LEADING EDGE RADIUS,
M_∞ = 10.55, Re/ft = 2 x 10^6.
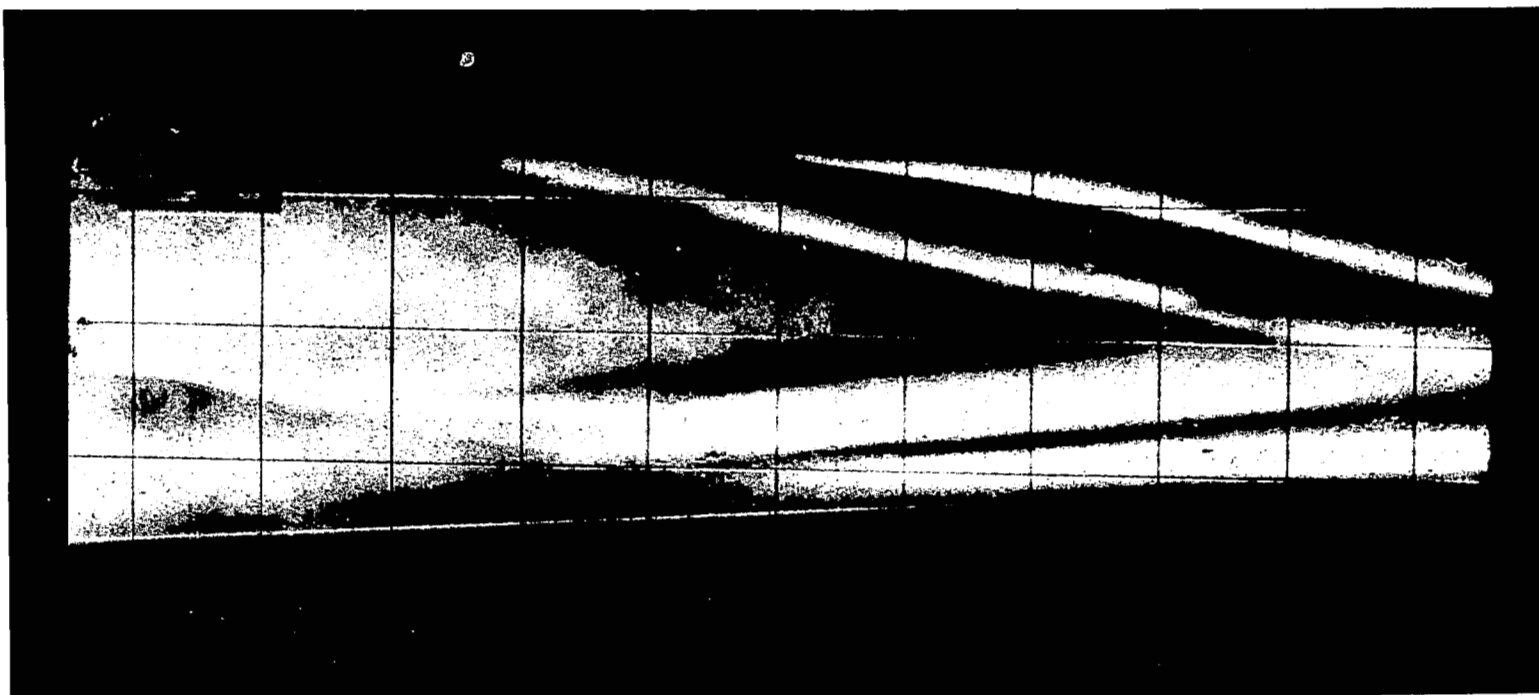
(a) .063 in. Leading Edge Radius

Figure 25. TYPICAL SCHLIEREN PHOTOGRAPHS OF LAMINAR INTERACTION REGION,

FLAT PLATE, α_g = 6°,
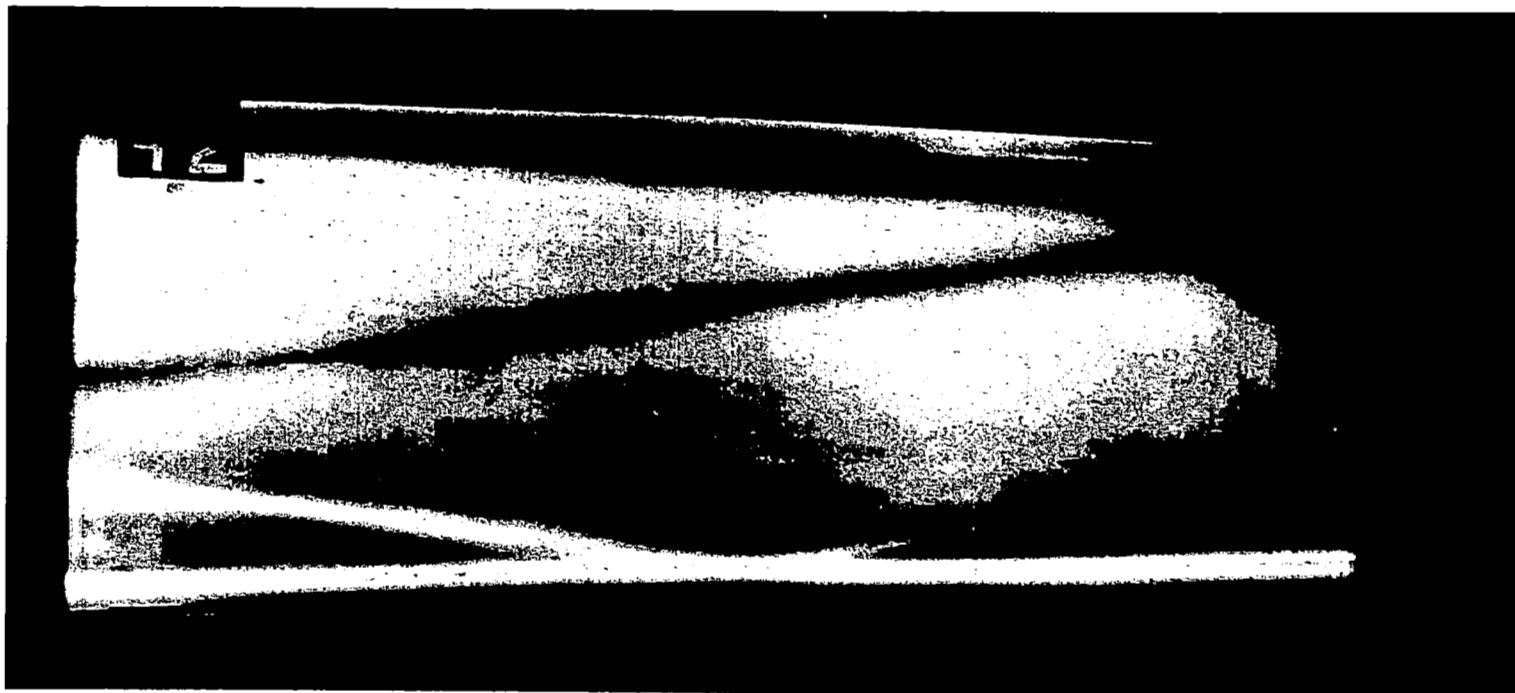
M_∞ = 10.4, Re/ft = .75 x 10^6 .

(b) Sharp Leading Edge

Figure 25. CONCLUDED.

Bow Shock Wave

(2)′ Shock Generator

Incident Shock

(2)

Region (1)

(3)

Reflected Shock

Compression Surface

∞
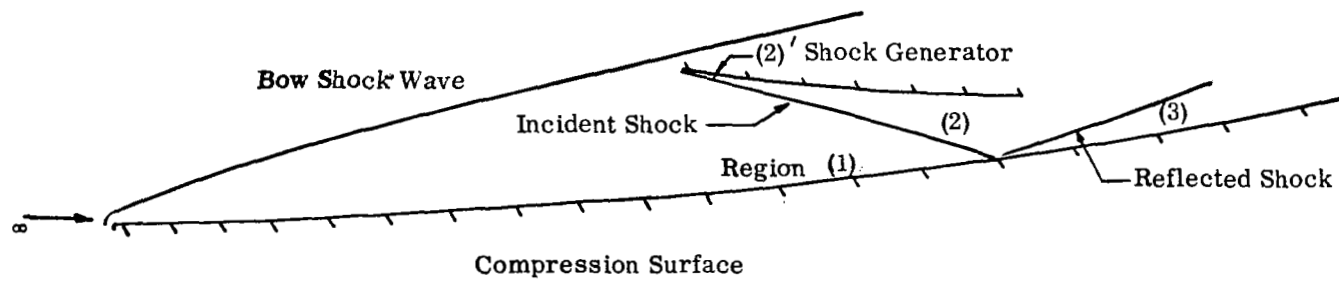
Figure 26. INTERACTION REGION DEFINITION.

(a) $M_\infty = 10.4$, $Re/ft = .75 \times 10^6$

▲ Sharp Leading Edge, Ref. 1

● .188 in. Leading Edge Radius

■ .063 in. Leading Edge Radius

Inviscid Theory, Ref. 4

– – – .063 in. Leading Edge Radius

——— .188 in. Leading Edge Radius
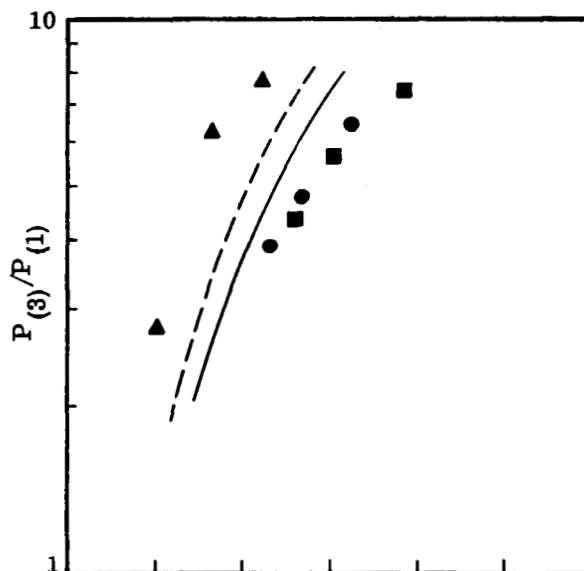
(b) $M_\infty = 7.3$, $Re/ft = .25 \times 10^6$

▲ Sharp Leading Edge, Ref. 1

● .188 in. Leading Edge Radius

■ .063 in. Leading Edge Radius

Inviscid Theory, Ref. 4

– – – .063 in. Leading Edge Radius

——— .188 in. Leading Edge Radius
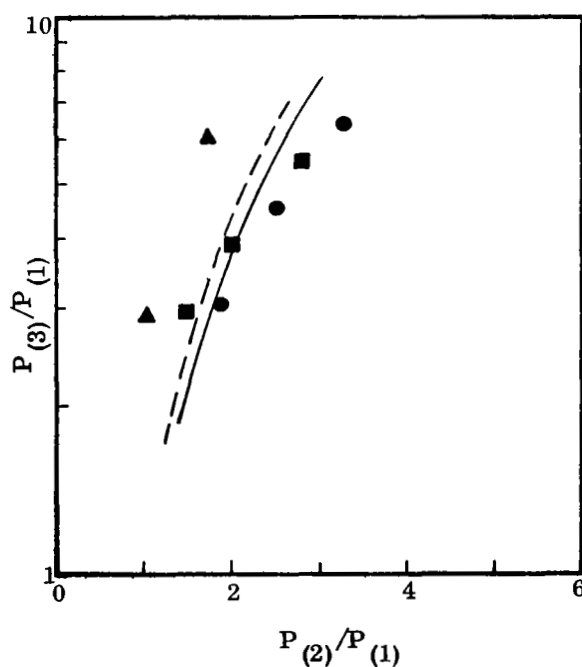
Figure 27. VARIATION OF MAXIMUM PRESSURE RATIO ACROSS INTERACTION
WITH INCIDENT SHOCK STRENGTH,
(COMPRESSION SURFACE).

65

	M$_\infty$	Re/ft
● Sharp Leading Edge, Ref. 1	10.40	0.80 x 10^6
■ Sharp Leading Edge, Ref. 1	10.55	2.00 x 10^6
⬤ .188 in. Leading Edge Radius	10.55	2.00 x 10^6
▲ .063 in. Leading Edge Radius	10.40	0.75 x 10^6
—— Inviscid Theory, Ref. 1	10.60	
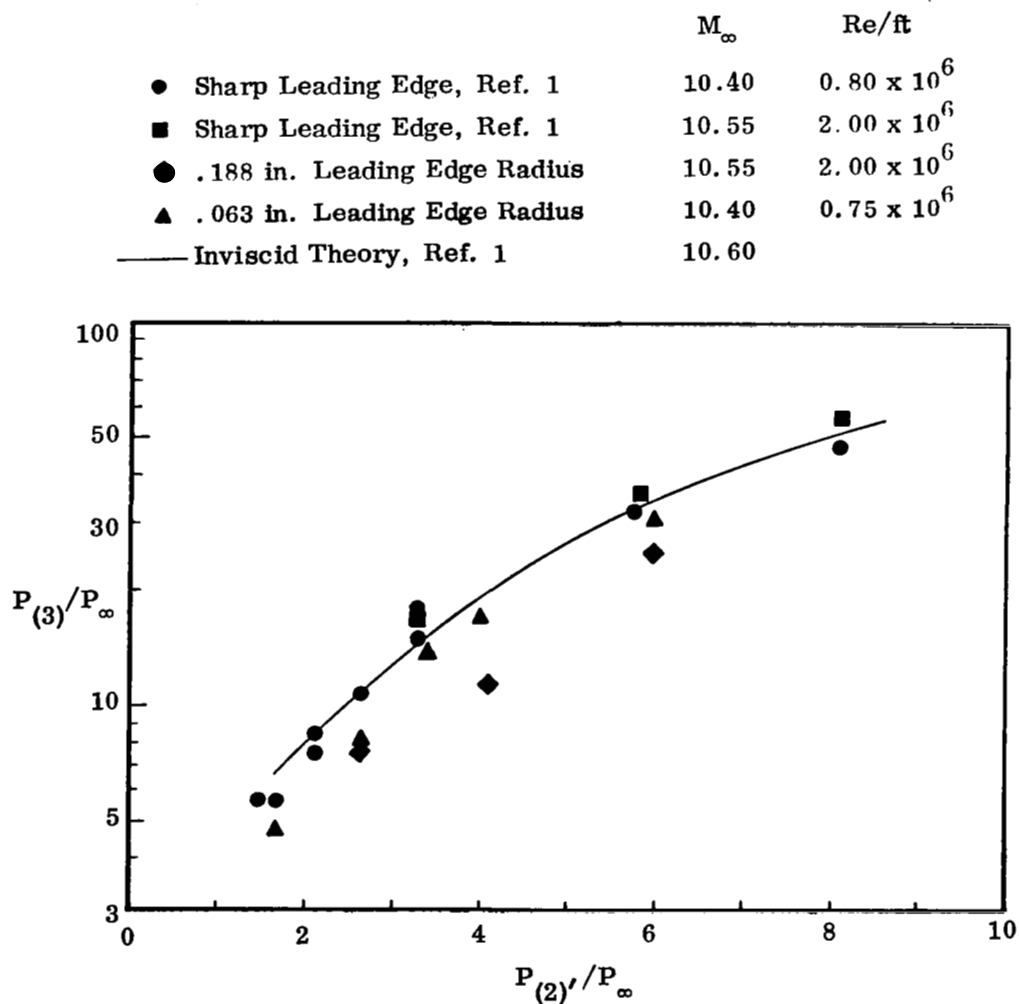
Figure 28. VARIATION OF MAXIMUM PRESSURE DOWNSTREAM OF INTERACTION
WITH INCIDENT SHOCK STRENGTH,
(FLAT PLATE).

66

Shock Generator

Theoretical Incident Shock

Experimental Laminar Boundary Layer
Without Interaction

(a)   .188 in. Leading Edge Radius

$\alpha_g = 2°$

(b)   .063 in. Leading Edge Radius

$\alpha_g = 2°$

P/P_∞

X, Inches
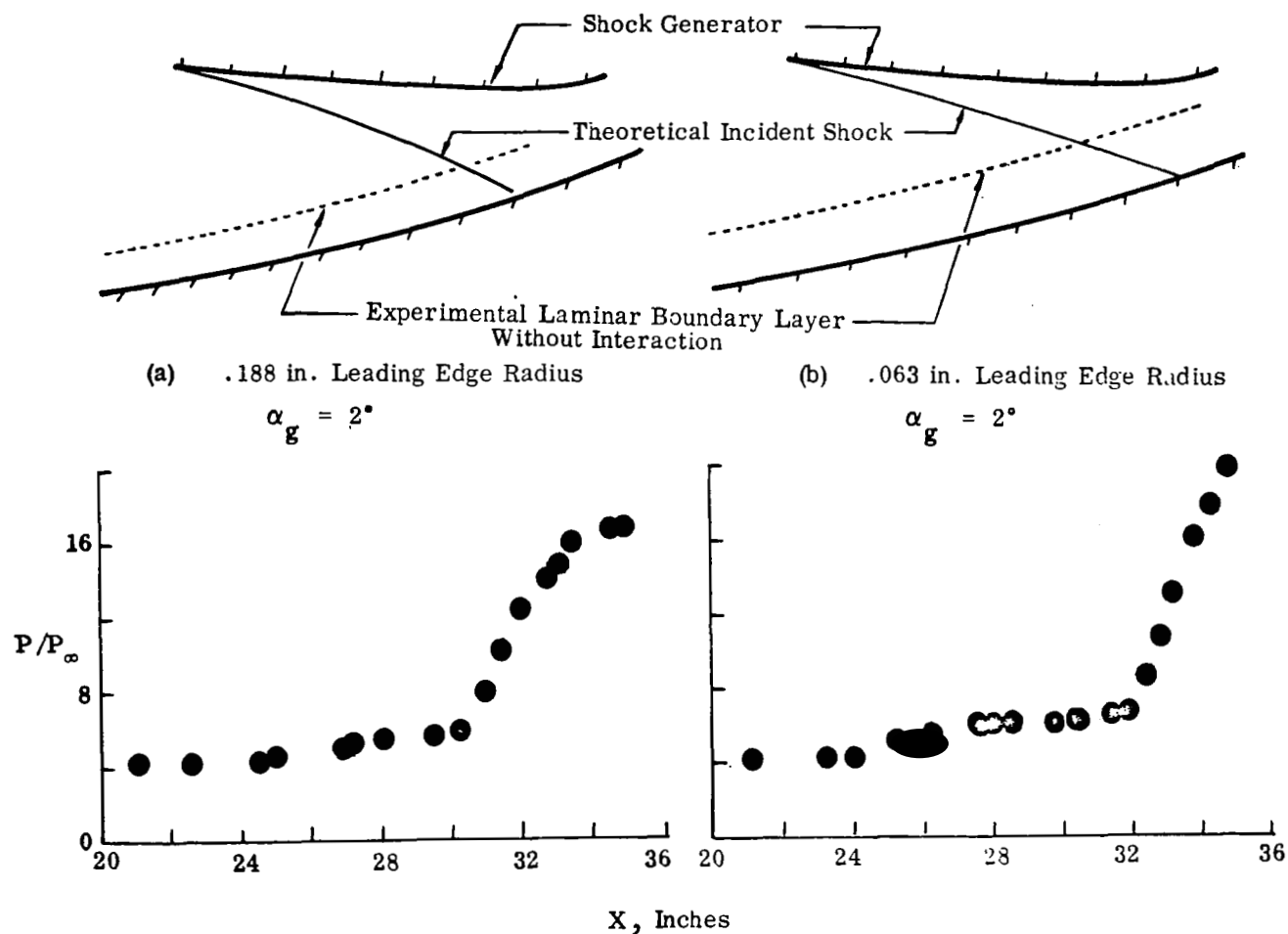
Figure 29. THEORETICAL AND EXPERIMENTAL INCIDENT SHOCK IMPINGEMENTS,

(COMPRESSION SURFACE),

$M_\infty = 10.55$, $Re/ft = 2 \times 10^6$.

|	α_g deg.	X_o in.
$\circ$	2.96	24.48
$\square$	4.03	24.48
$\triangle$	4.98	24.48
$\diamond$	no generator	24.48
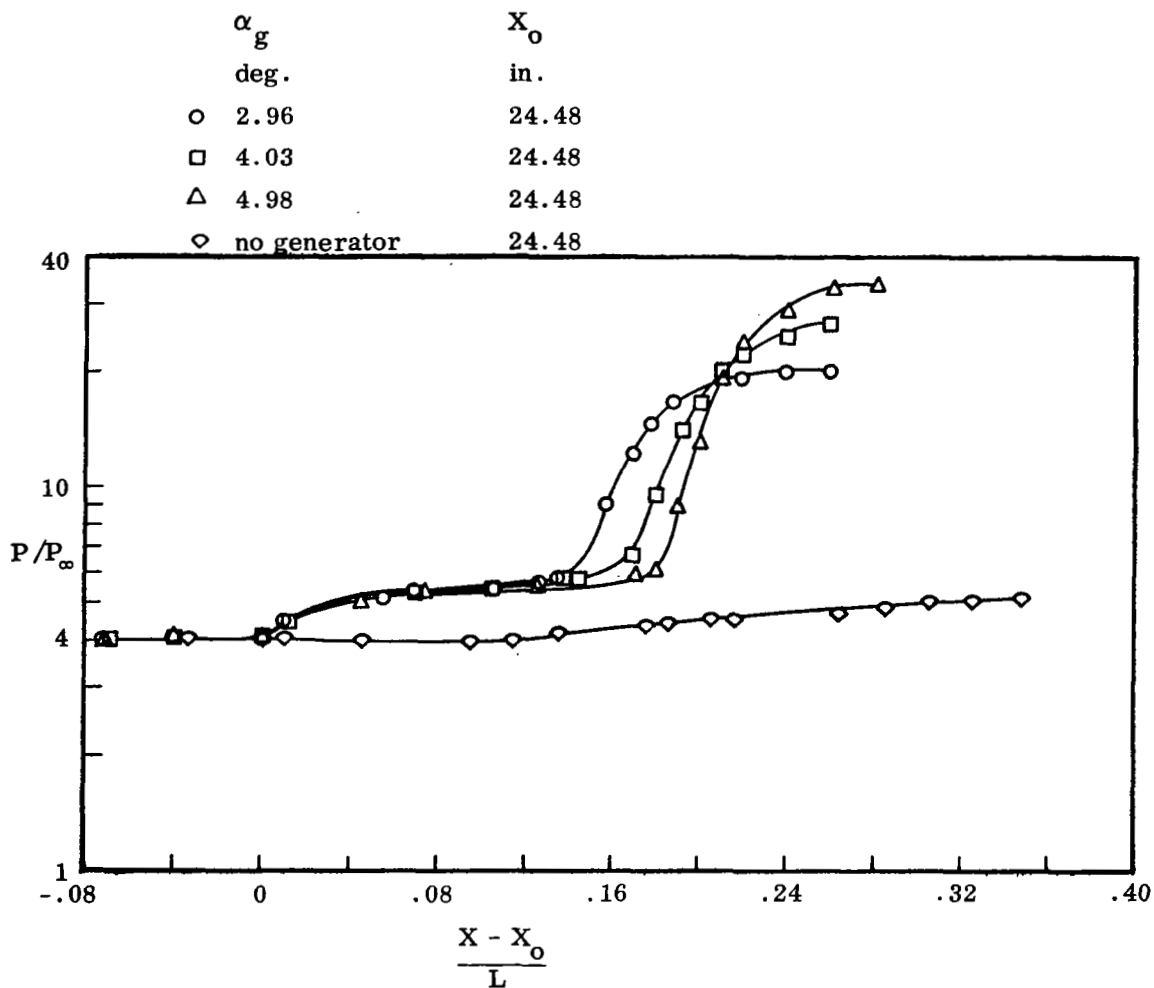
Figure 30. SURFACE PRESSURE DISTRIBUTIONS WITHIN SHOCK WAVE -
LAMINAR BOUNDARY LAYER INTERACTION,
COMPRESSION SURFACE, .188 in. LEADING EDGE RADIUS,
$M_\infty = 10.4$, Re/ft = .75 x 10^6.

	α_g deg.	X_o in.
O	4.02	23.52
□	7.00	26.40
◇	No Generator	23.52
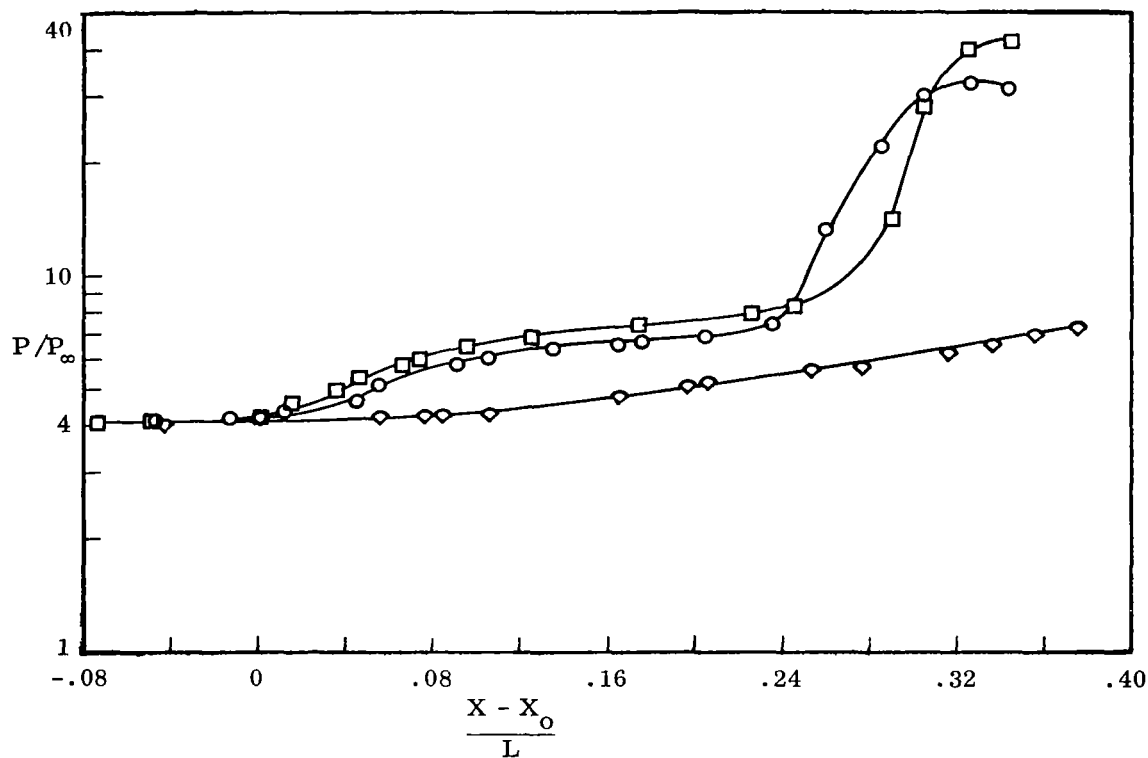
Figure 31. SURFACE PRESSURE DISTRIBUTIONS WITHIN SHOCK WAVE -
LAMINAR BOUNDARY LAYER INTERACTION,
COMPRESSION SURFACE, .063 in. LEADING EDGE RADIUS,
$M_\infty = 10.4$, Re/ft $= .75 \times 10^6$.

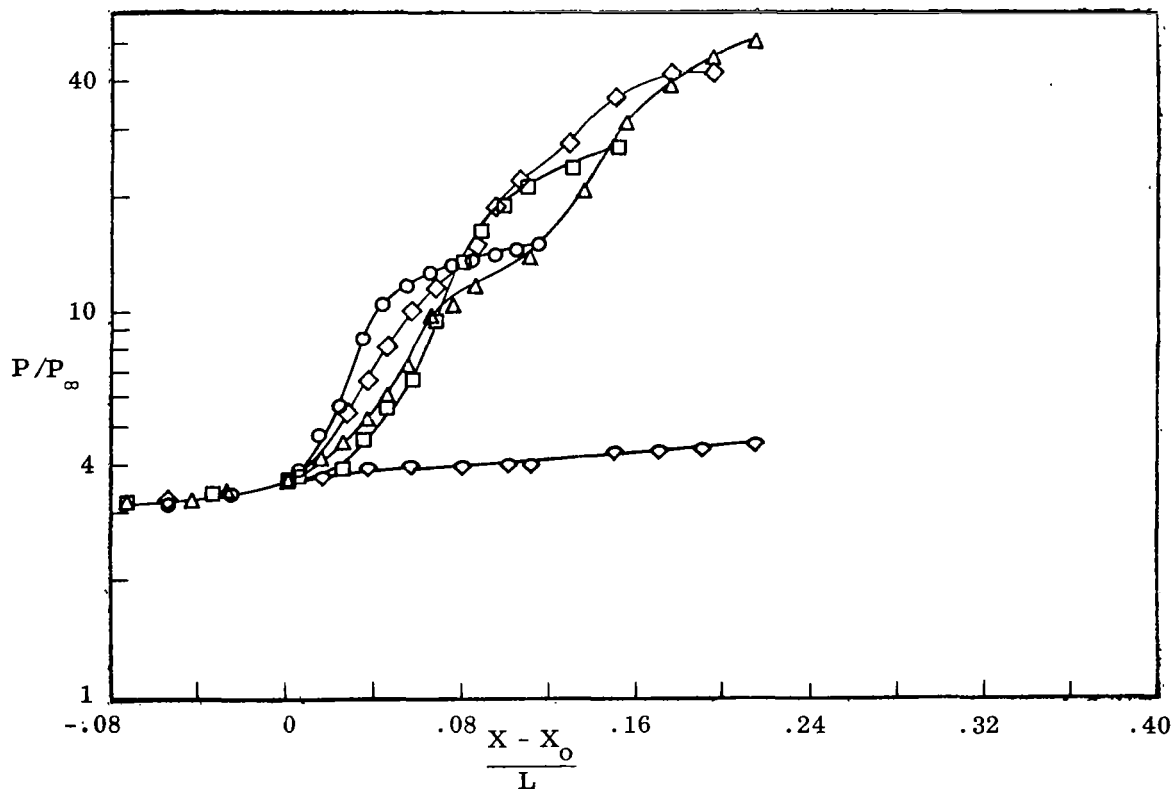|	α_g	X_o
	deg.	in.
O	2.00	24.48
□	4.00	24.96
△	6.01	24.96
◇	No Generator	24.48
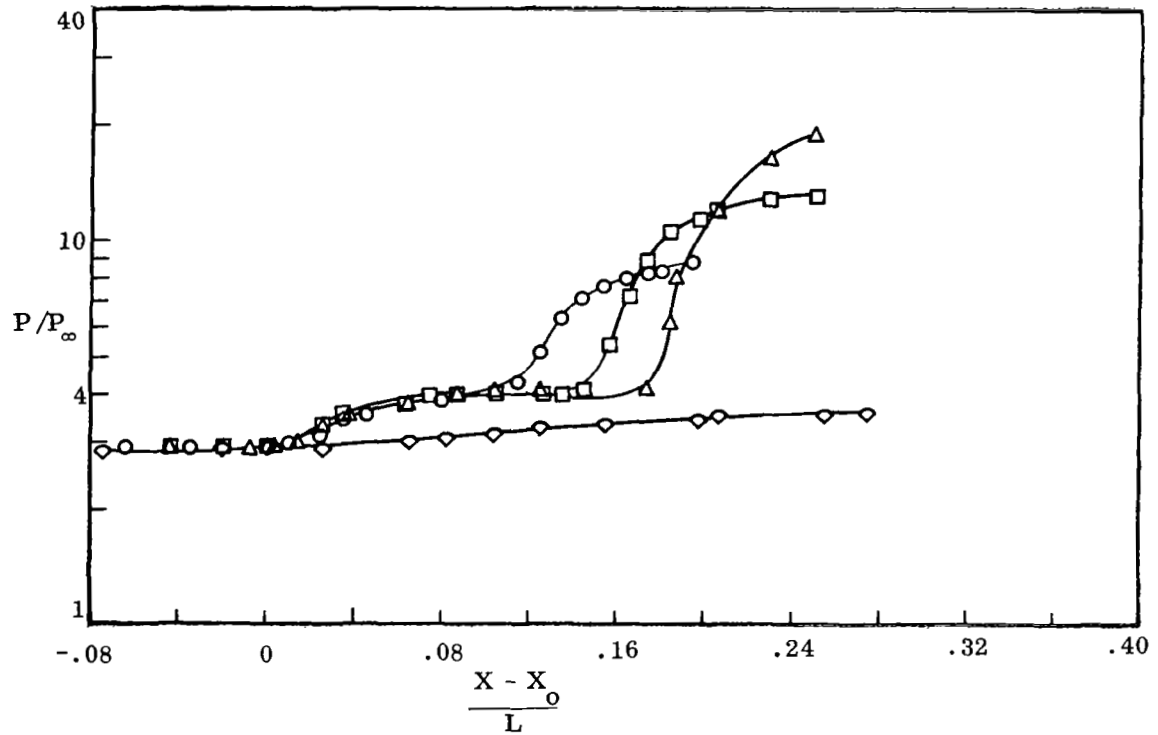
Figure 32. SURFACE PRESSURE DISTRIBUTIONS WITHIN SHOCK WAVE -
LAMINAR BOUNDARY LAYER INTERACTION,
COMPRESSION SURFACE, .188 in. LEADING EDGE RADIUS,
$M_\infty = 7.3$, Re/ft = .25 x 10^6.

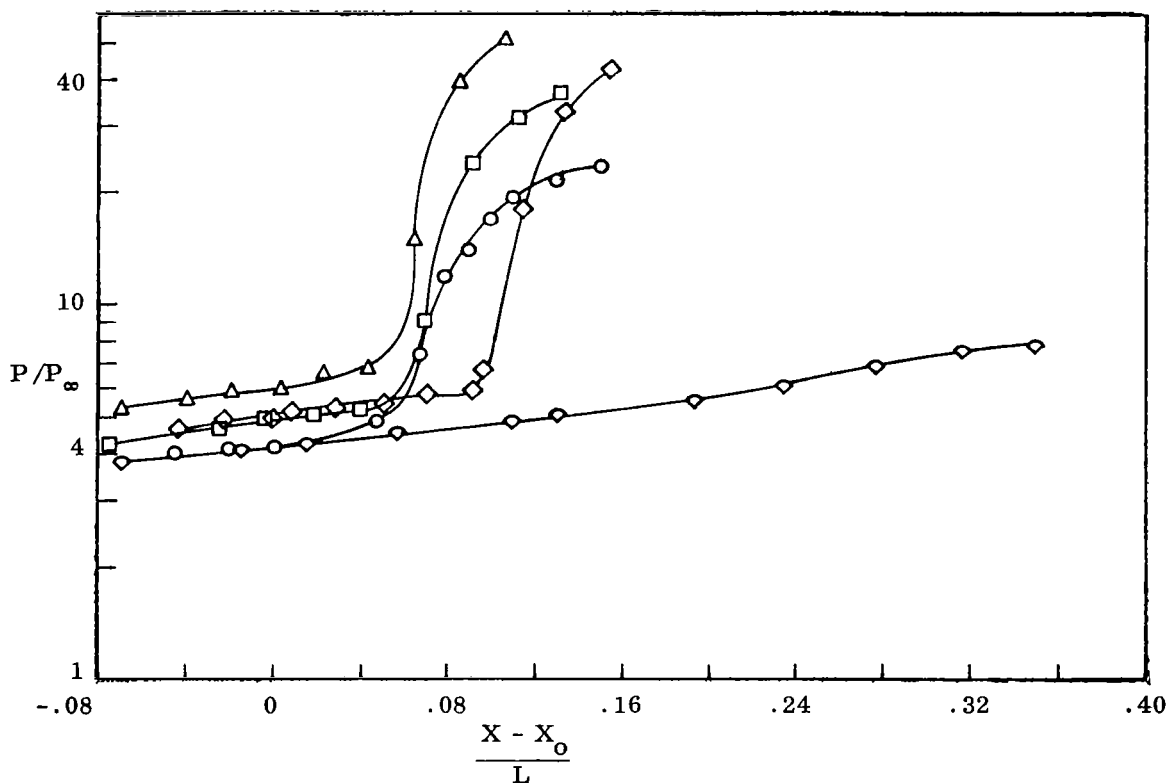|	α_g	X_o
	deg.	in.
o	2.05	24.96
□	3.02	24.96
△	4.00	24.96
◇	5.00	24.96
◇	No Generator	24.96
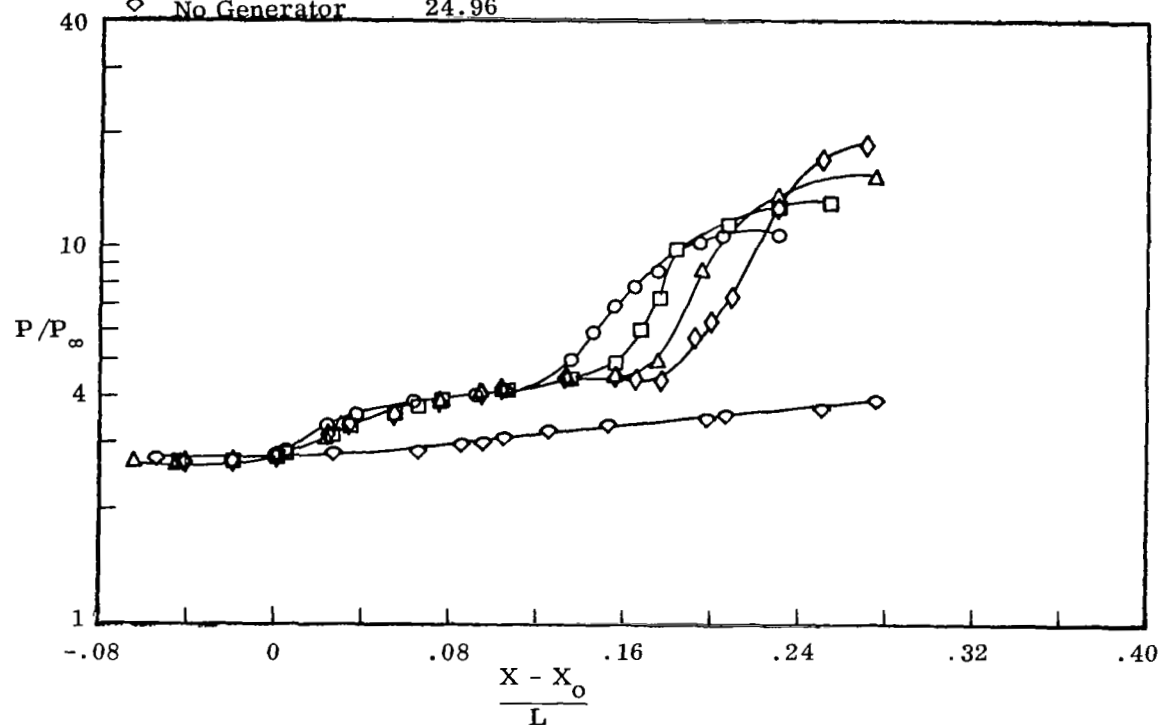
Figure 33. SURFACE PRESSURE DISTRIBUTIONS WITHIN SHOCK WAVE –
LAMINAR BOUNDARY LAYER INTERACTION,
COMPRESSION SURFACE, .063 in. LEADING EDGE RADIUS,
M_∞ = 7.3, Re/ft = .25 x 10^6.

71

	α_g	X_o
	deg.	in.
o	4.00	31.10
□	6.00	31.10
△	8.00	31.39
◇	No Generator	31.10

Trip Configuration No. 3

$$P/P_\infty$$

$$\frac{X - X_o}{L}$$
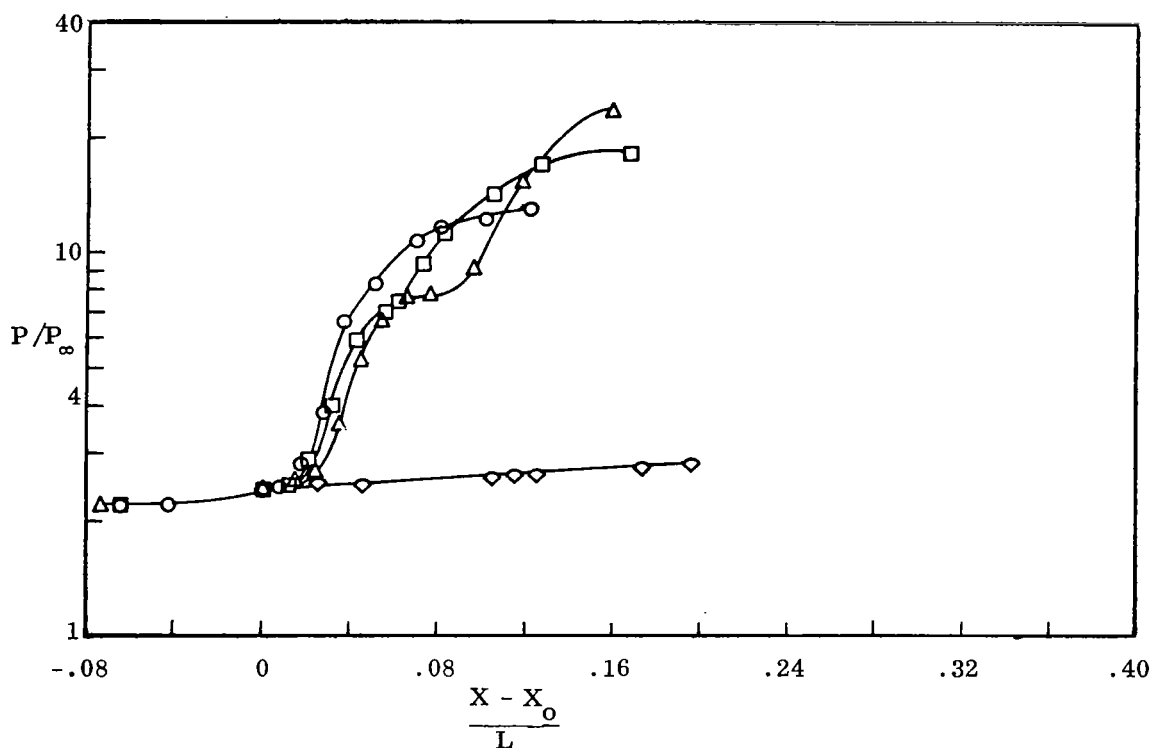
Figure 34. SURFACE PRESSURE DISTRIBUTIONS WITHIN SHOCK WAVE -
TURUBLENT BOUNDARY LAYER INTERACTION,
COMPRESSION SURFACE, .188 in. LEADING EDGE RADIUS,
M_∞ = 7.4, Re/ft = 2 x 10^6.

	α_g	X_o
	deg.	in.
○	2.02	31.92
□	4.00	33.12
△	6.05	36.00
◇	7.95	38.03
◇	No Generator	31.92

Trip Configuration No. 4
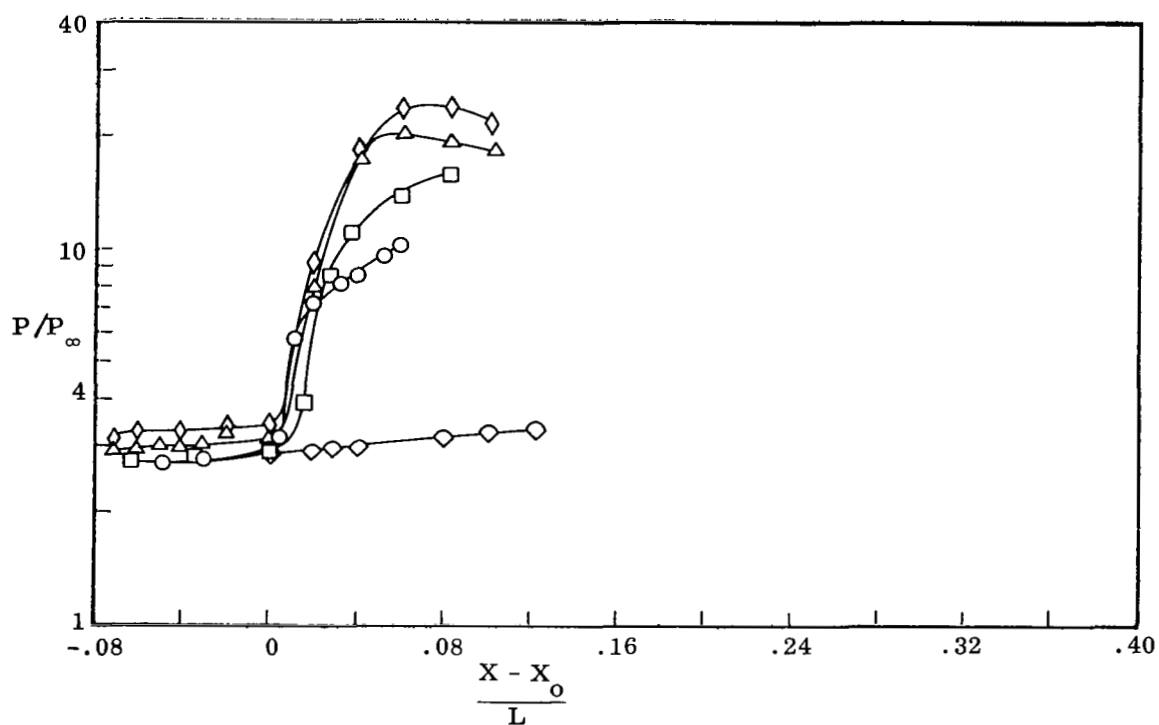
Figure 35. SURFACE PRESSURE DISTRIBUTIONS WITHIN SHOCK WAVE -
TURBULENT BOUNDARY LAYER INTERACTION,
COMPRESSION SURFACE, .063 in. LEADING EDGE RADIUS,
$M_\infty = 7.4$, Re/ft $= 2 \times 10^6$.

73

	α_g	X_o
	deg.	in.
O	2.06	29.28
□	4.00	29.76
◇	6.00	29.76
△	8.02	30.72
◇	No Generator	29.28

Trip Configuration No. 1
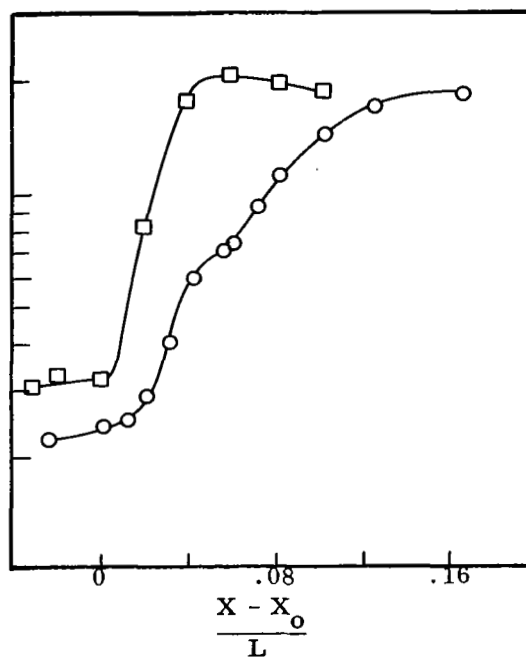

Figure 36. SURFACE PRESSURE DISTRIBUTIONS WITHIN SHOCK WAVE -
TURBULENT BOUNDARY LAYER INTERACTION,
COMPRESSION SURFACE, .188 in. LEADING EDGE RADIUS,
$M_\infty = 10.55$, Re/ft $= 2 \times 10^6$.

74

	α_g	X_o
	deg.	in.
○	2.03	29.36
□	4.30	32.64
◇	6.02	33.60
△	8.05	37.92
◇	No Generator	29.36

Trip Configuration No. 2

Figure 37. SURFACE PRESSURE DISTRIBUTIONS WITHIN SHOCK WAVE -
TURBULENT BOUNDARY LAYER INTERACTION,
COMPRESSION SURFACE, .063 in. LEADING EDGE RADIUS,
$M_\infty = 10.55$, Re/ft $= 2 \times 10^6$.

○ Sharp Leading Edge, Ref. 19

□ .188 in. Leading Edge Radius

△ .063 in. Leading Edge Radius
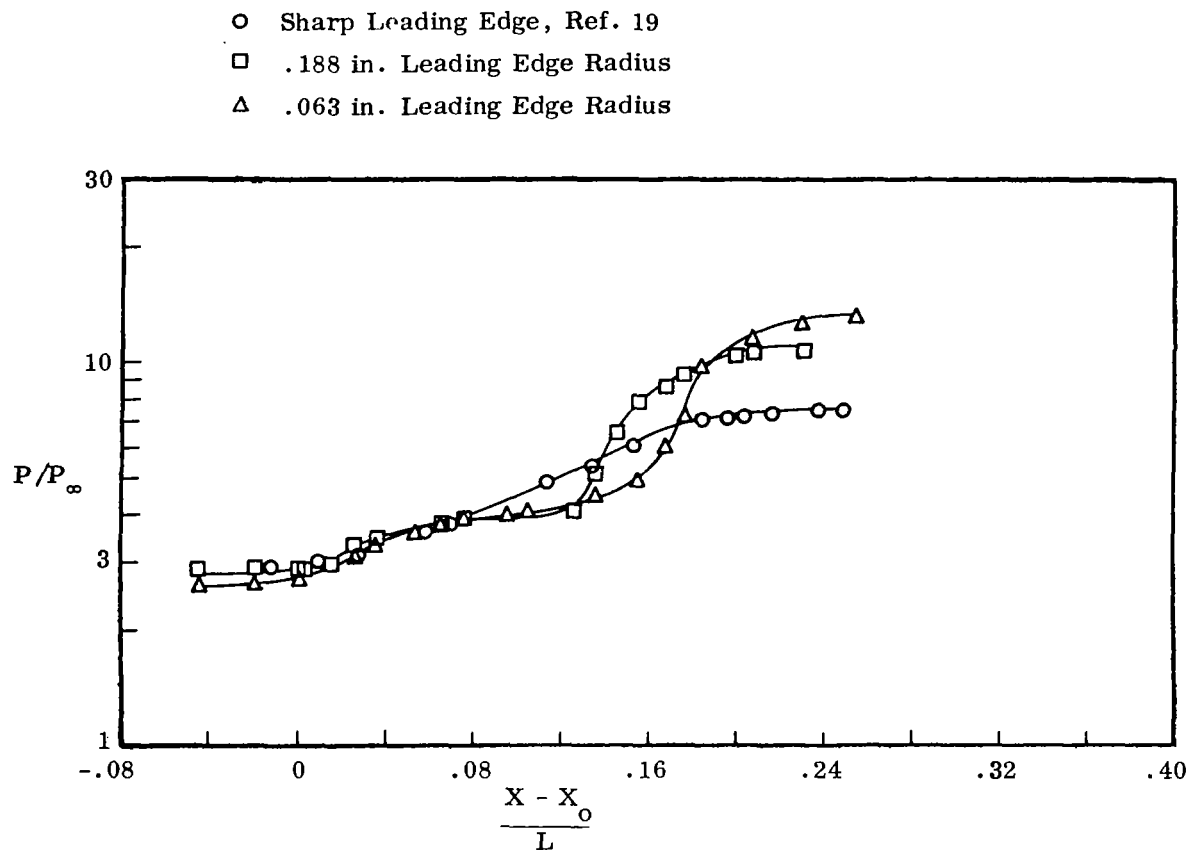
Figure 38. EFFECTS OF BLUNTNESS ON SURFACE PRESSURE DISTRIBUTIONS
IN REGIONS OF SHOCK WAVE –
LAMINAR BOUNDARY LAYER INTERACTIONS,
COMPRESSION SURFACE, $\alpha_g = 3°$,
$M_\infty = 7.3$, Re/ft $= .25 \times 10^6$.

(a) $\alpha_g = 4°$
  ○ .188 in. Leading Edge Radius
    Trip Configuration No. 3
  □ .063 in. Leading Edge Radius
    Trip Configuration No. 4
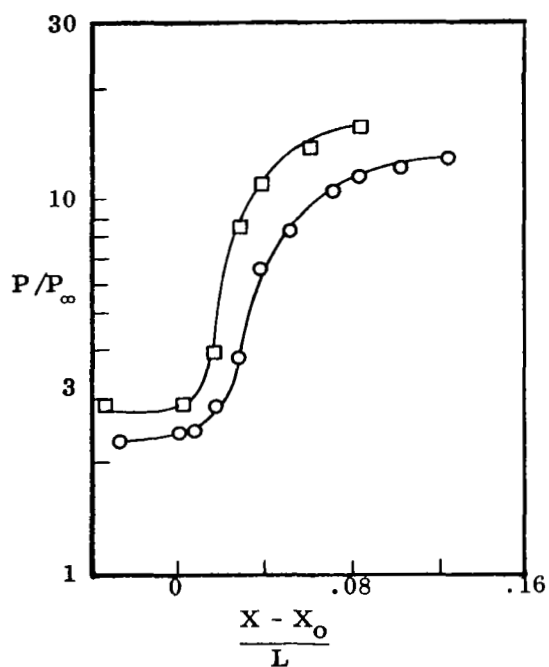
(b) $\alpha_g = 6°$
  ○ .188 in. Leading Edge Radius
    Trip Configuration No. 3
  □ .063 in. Leading Edge Radius
    Trip Configuration No. 4

Figure 39. EFFECTS OF BLUNTNESS ON SURFACE PRESSURE DISTRIBUTIONS
IN REGIONS OF SHOCK WAVE –
TURBULENT BOUNDARY LAYER INTERACTIONS,
COMPRESSION SURFACE,
$M_\infty = 7.4$, Re/ft $= 2 \times 10^6$.

77

M_∞ = 7.4, Re/ft = 2 x 10^6

.188 in. Leading Edge Radius

α_g = 6°

Trip Configuration No. 3

□ Profile Station - X/L = .646, δ = .520

○ Profile Station - X/L = .775, δ = .301
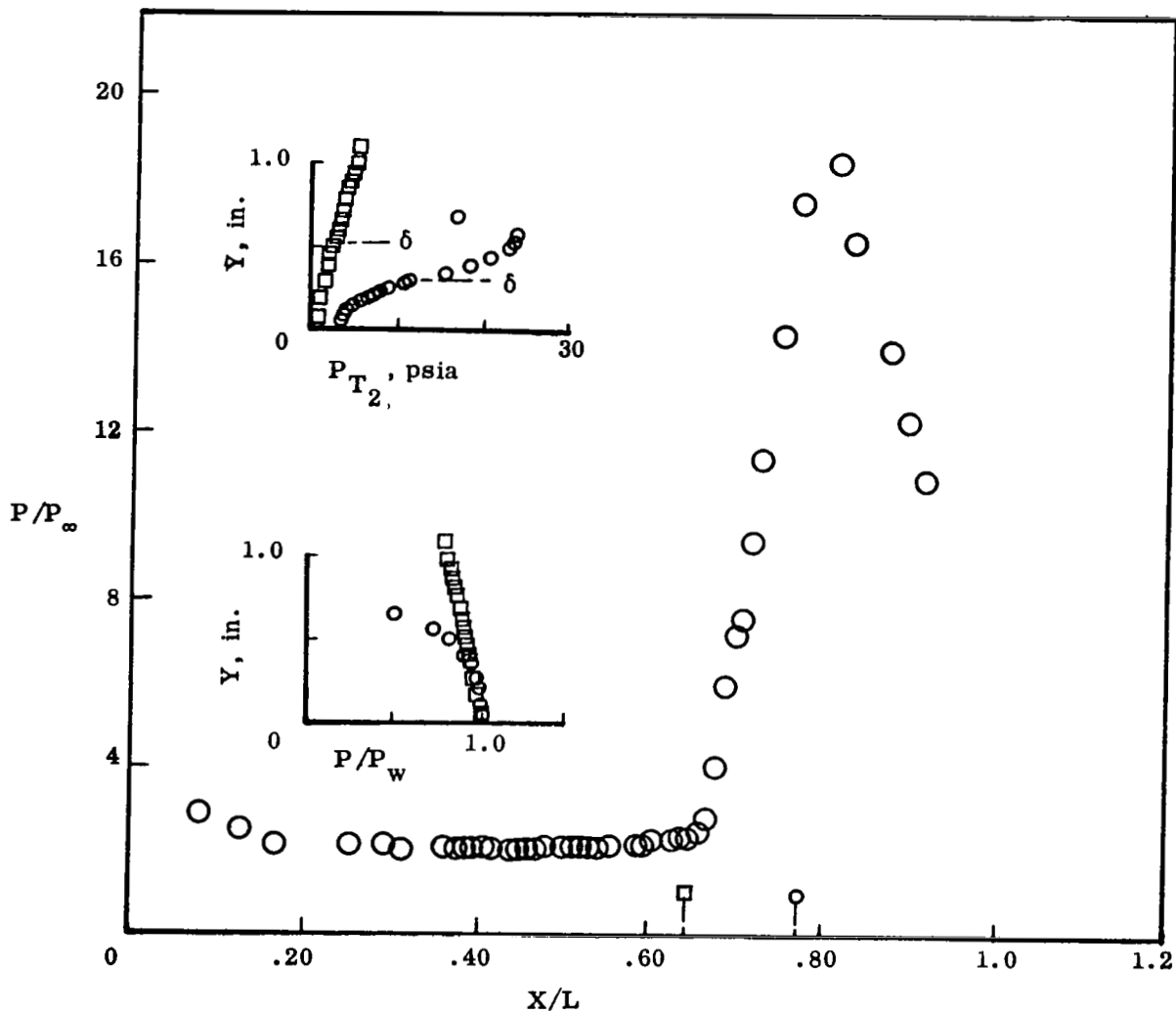
Figure 40. SURFACE PRESSURE - PROFILE DATA WITHIN SHOCK WAVE -
SEPARATED,TURBULENT BOUNDARY LAYER INTERACTION,
(COMPRESSION SURFACE).
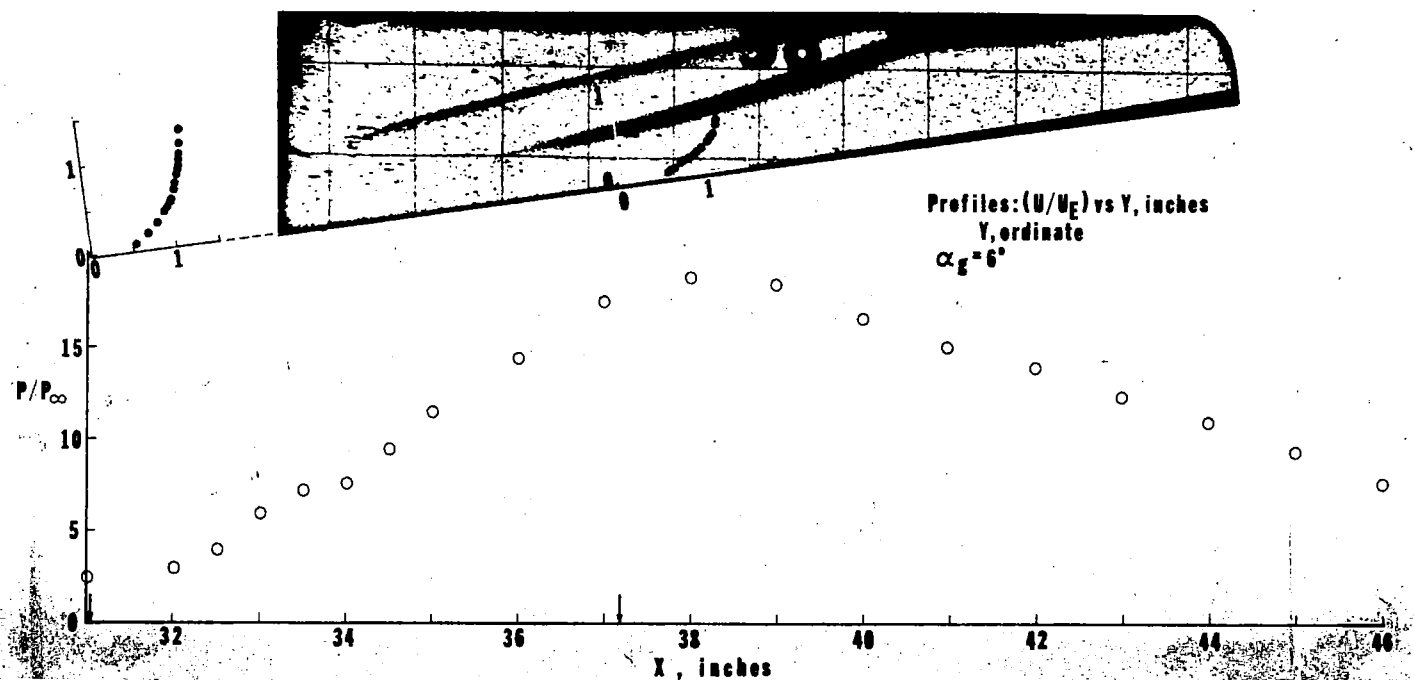
Figure 41. EXPERIMENTAL DATA OBTAINED IN THE REGION OF SEPARATED, TURBULENT INTERACTION, COMPRESSION SURFACE, .18Sin.LEADING EDGE RADIUS, $M_\infty = 7.4$, $Re/ft = 2 \times 10^6$.

Profiles: (U/U_E) vs Y, inches
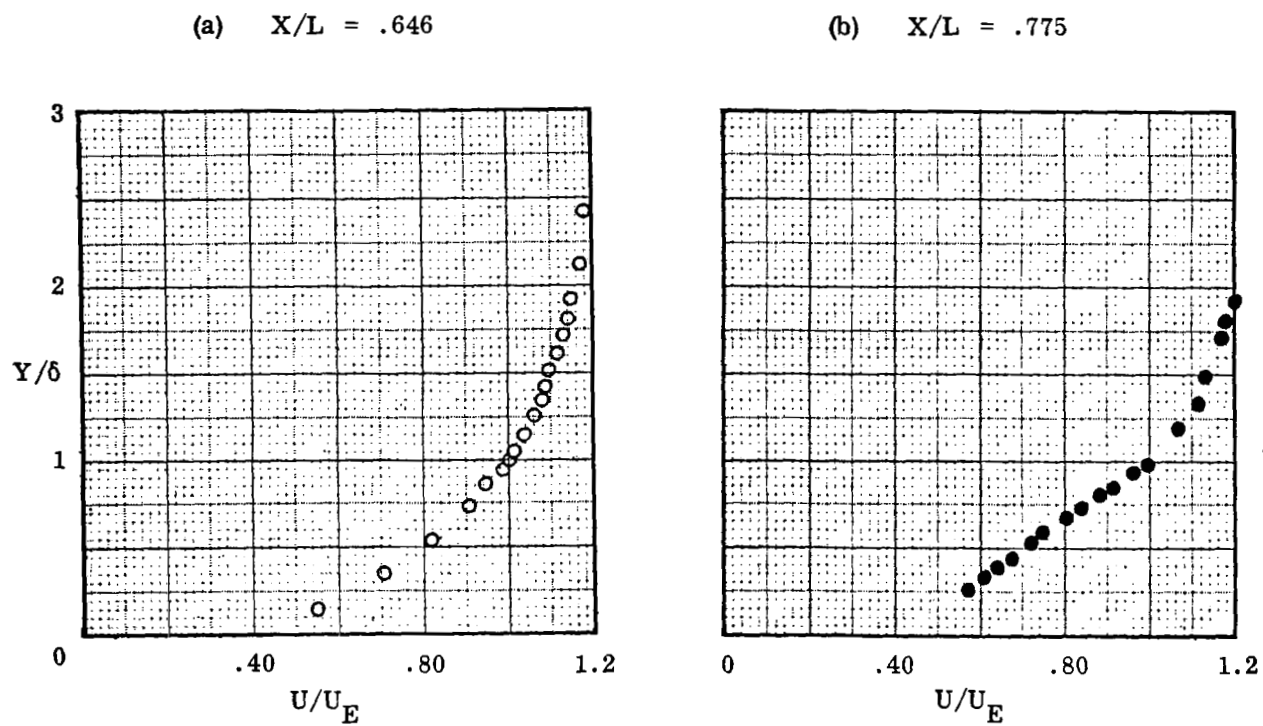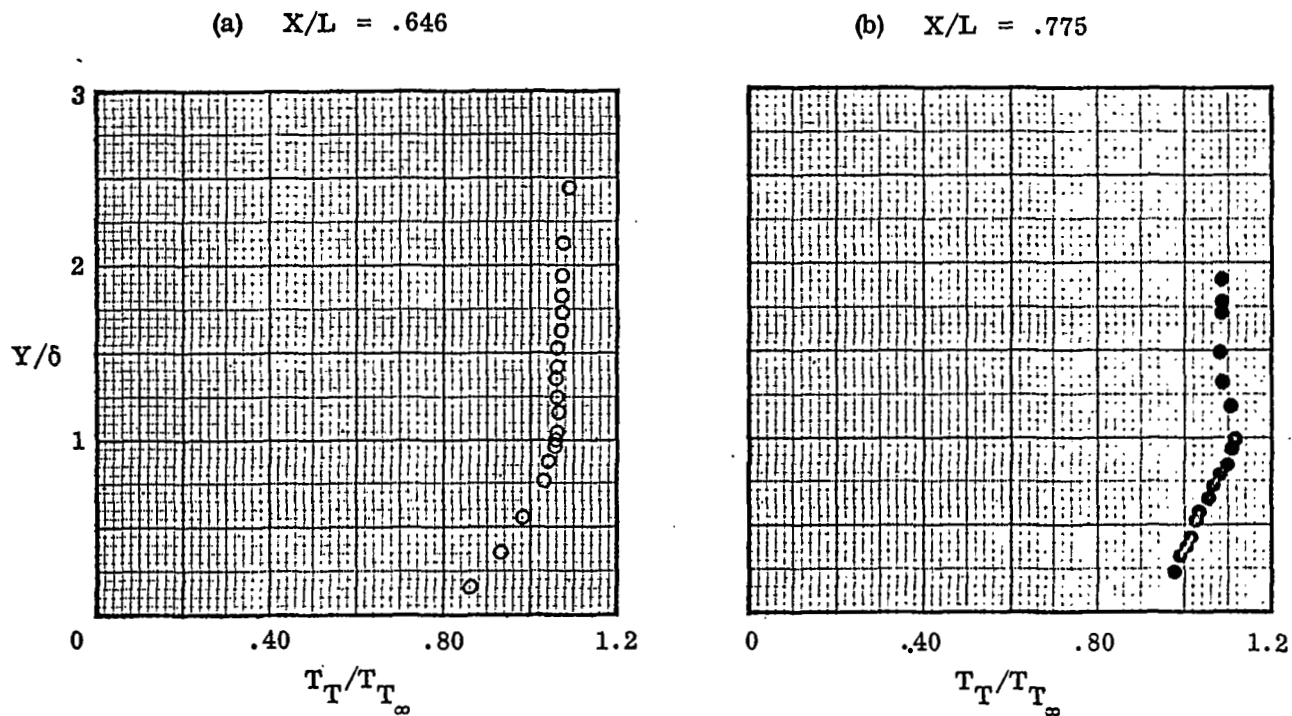Y, ordinate
$\alpha_g = 6°$

P/P_∞

X , inches

(a) X/L = .646

(b) X/L = .775
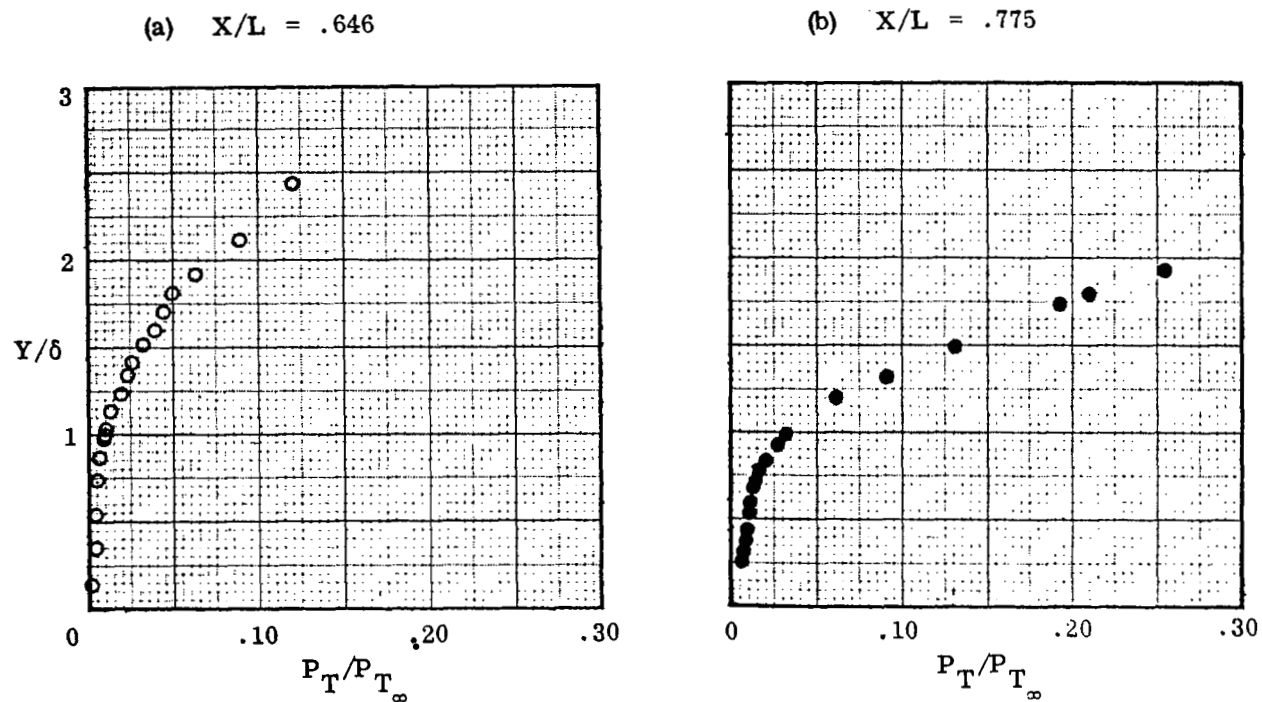
Figure 42. STAGNATION PRESSURE PROFILES WITHIN SEPARATED, TURBULENT INTERACTION,
COMPRESSION SURFACE, .188 in. LEADING EDGE RADIUS,
M_∞ = 7.4,   Re/ft = 2 x 10^6.

(a) X/L = .646   (b) X/L = .775
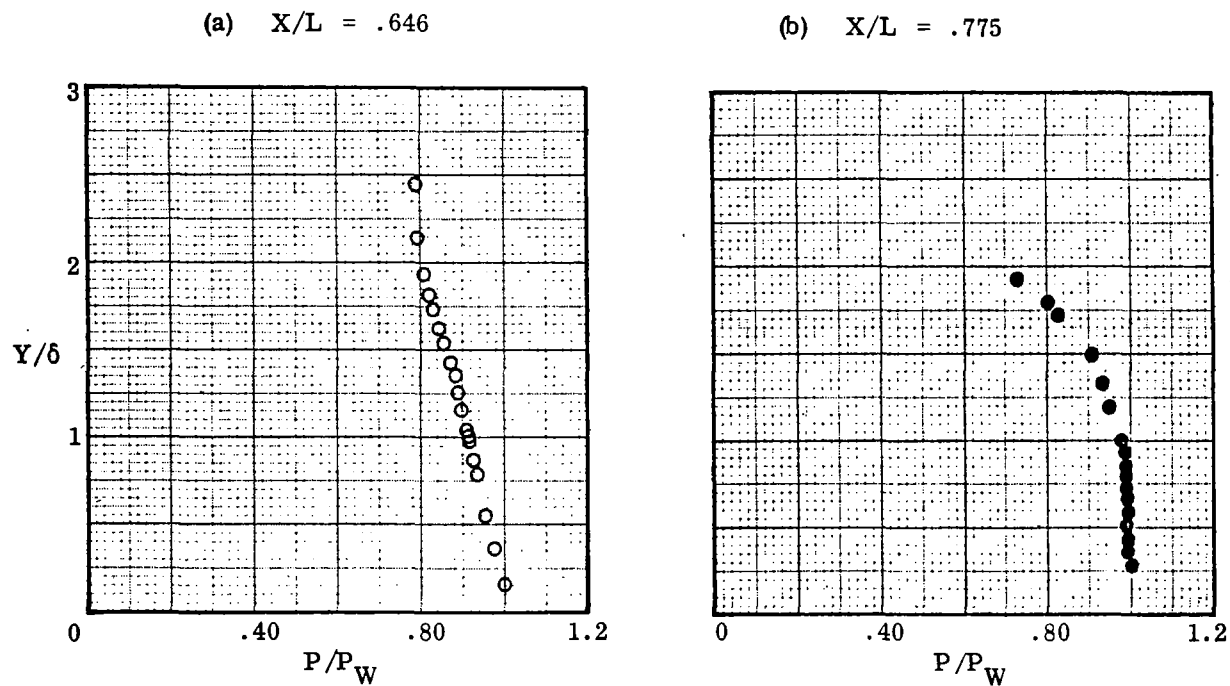
Figure 43. STATIC PRESSURE PROFILES WITHIN SEPARATED, TURBULENT INTERACTION,
COMPRESSION SURFACE, .188 in. LEADING EDGE RADIUS,
M_∞ = 7.4,   Re/ft = 2 x 10^6.

(a) X/L = .646

(b) X/L = .775

Figure 44. VELOCITY PROFILES WITHIN SEPARATED, TURBULENT INTERACTION,
COMPRESSION SURFACE, .188 in. LEADING EDGE RADIUS,
M_∞ = 7.4, Re/ft = 2 x 10^6.

(a)   X/L = .646   (b)   X/L = .775

Figure 45.   TOTAL TEMPERATURE PROFILES WITHIN SEPARATED, TURBULENT INTERACTION, COMPRESSION SURFACE, .188 in. LEADING EDGE RADIUS, $M_\infty = 7.4$, Re/ft = 2×10^6.

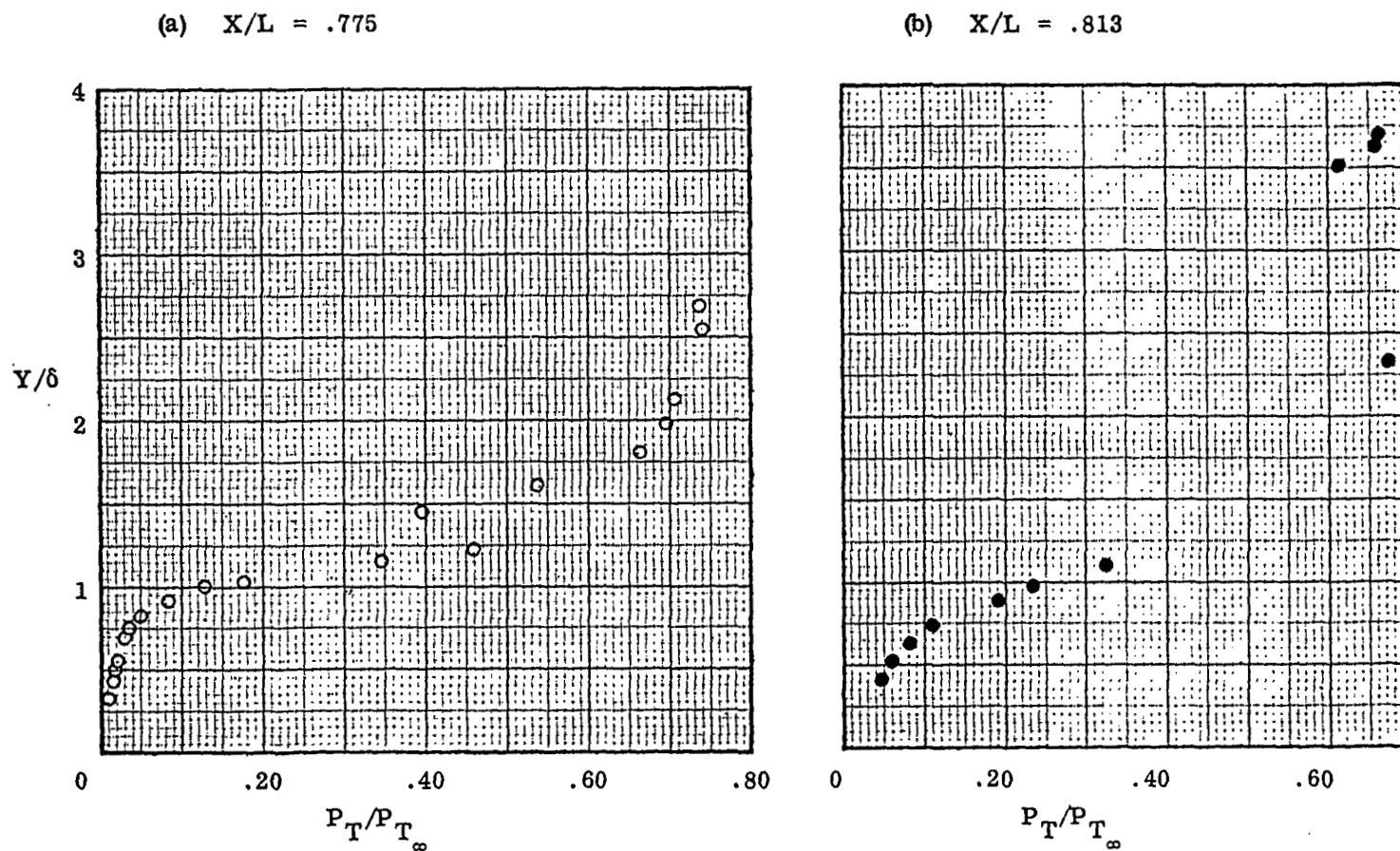$M_\infty = 7.4$, Re/ft = 2×10^6

.063 in. Leading Edge Radius

$\alpha_g = 6°$

Trip Configuration No. 4

□ Probe Station – X/L = .775, δ = .253

○ Probe Station – X/L = .813, δ = .182
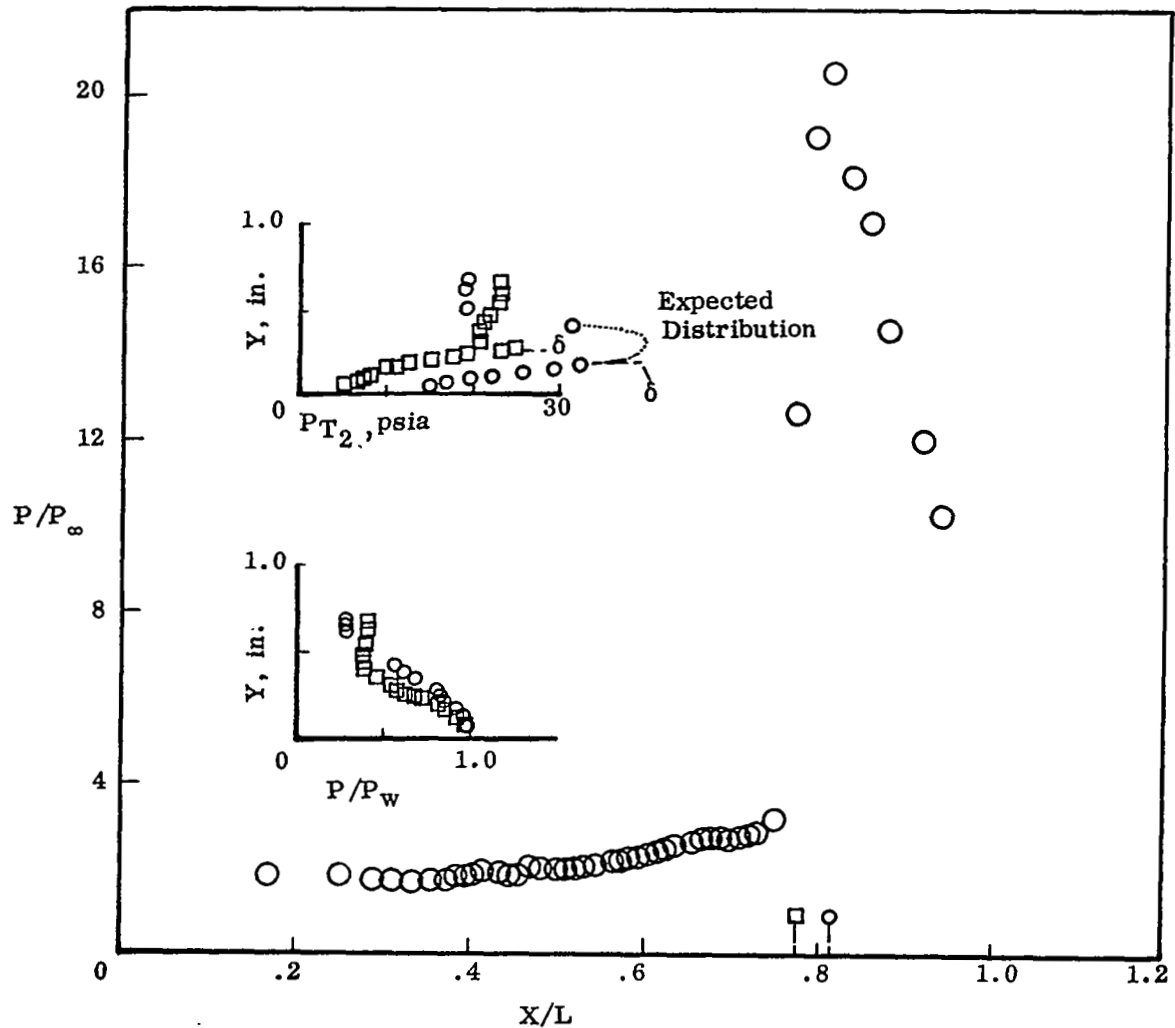
Figure 46. SURFACE PRESSURE – PROFILE DATA WITHIN SHOCK WAVE-
ATTACHED,TURBULENT BOUNDARY LAYER INTERACTION,
(COMPRESSION SURFACE).
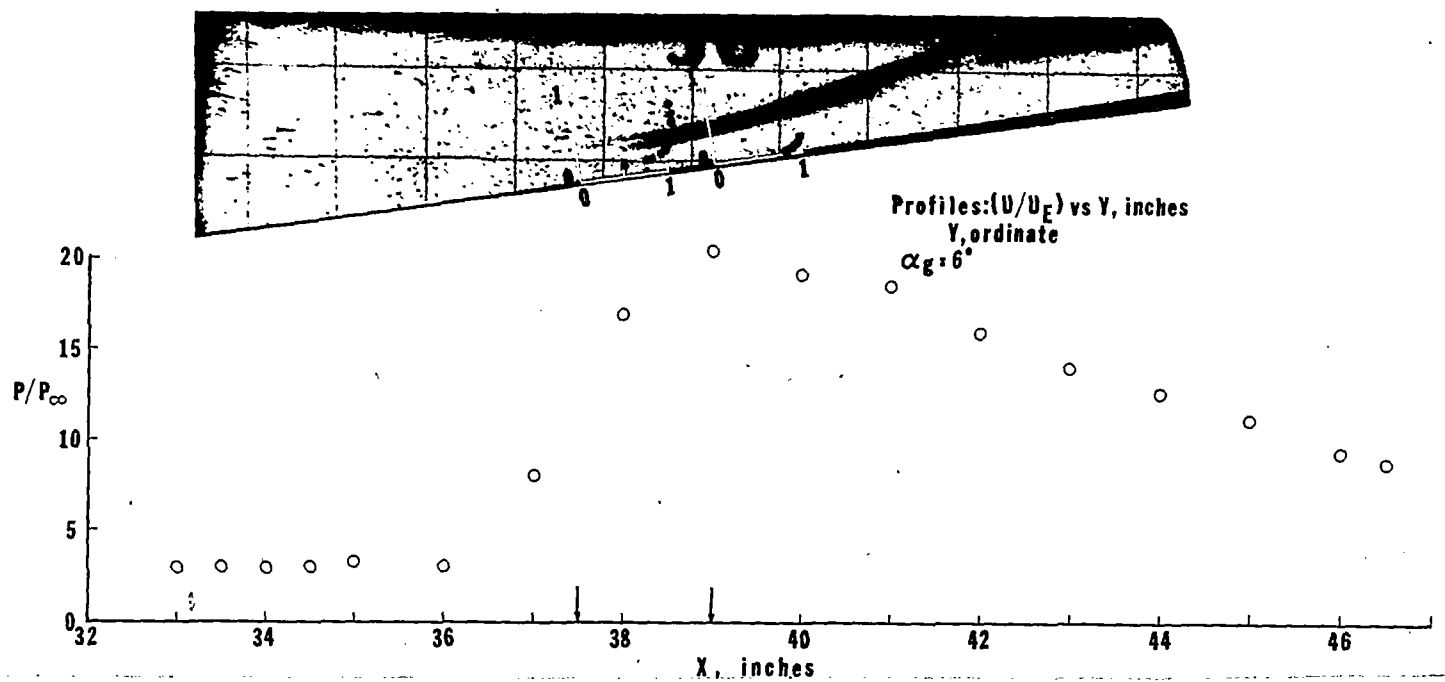
Figure 47. EXPERIMENTAL DATA OBTAINED IN THE REGION OF ATTACHED, TURBULENT INTERACTION,
COMPRESSION SURFACE, .063 in. LEADING EDGE RADIUS,
$M_\infty = 7.4$, Re/ft$= 2 \times 10^6$.

Figure 48. STAGNATION PRESSURE PROFILES WITHIN ATTACHED, TURBULENT INTERACTION, COMPRESSION SURFACE, .063 in. LEADING EDGE RADIUS,
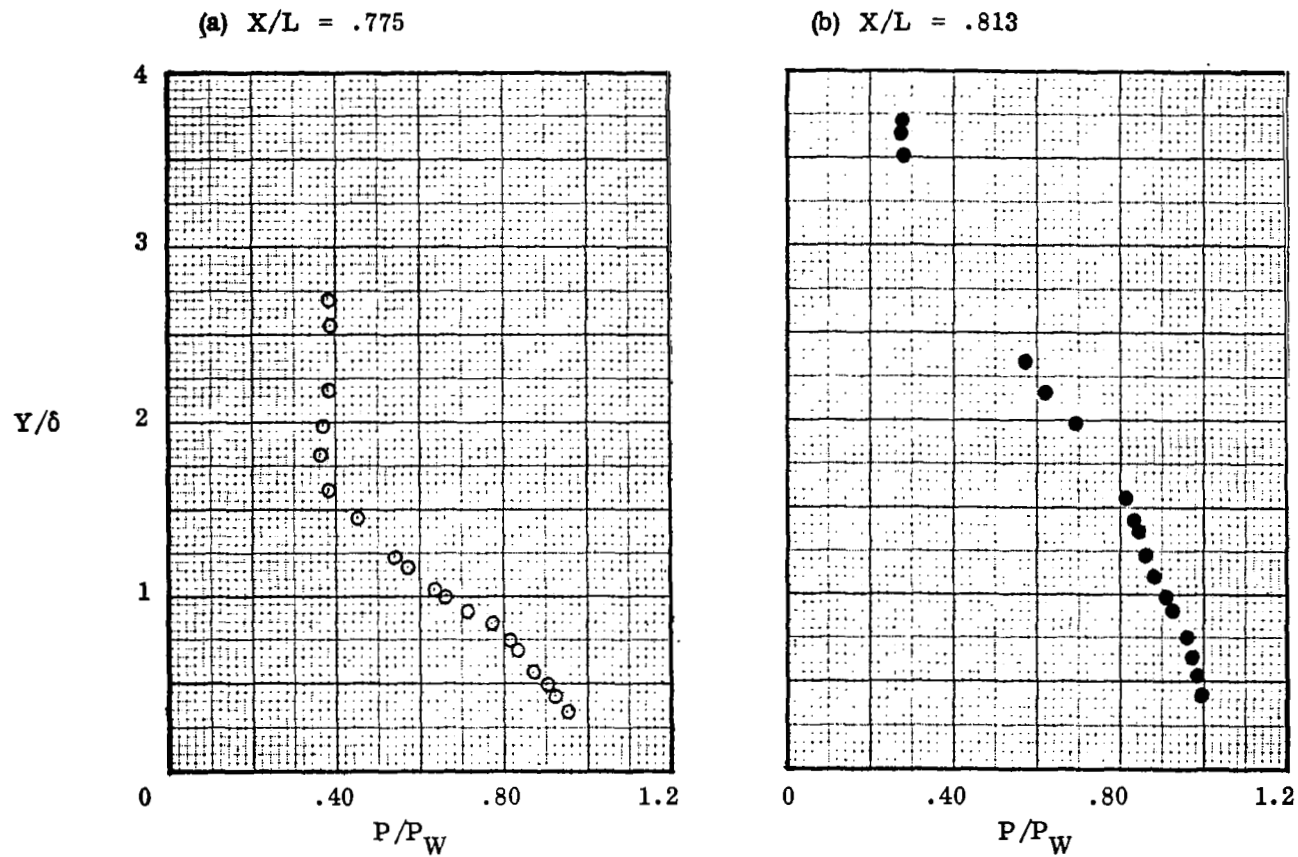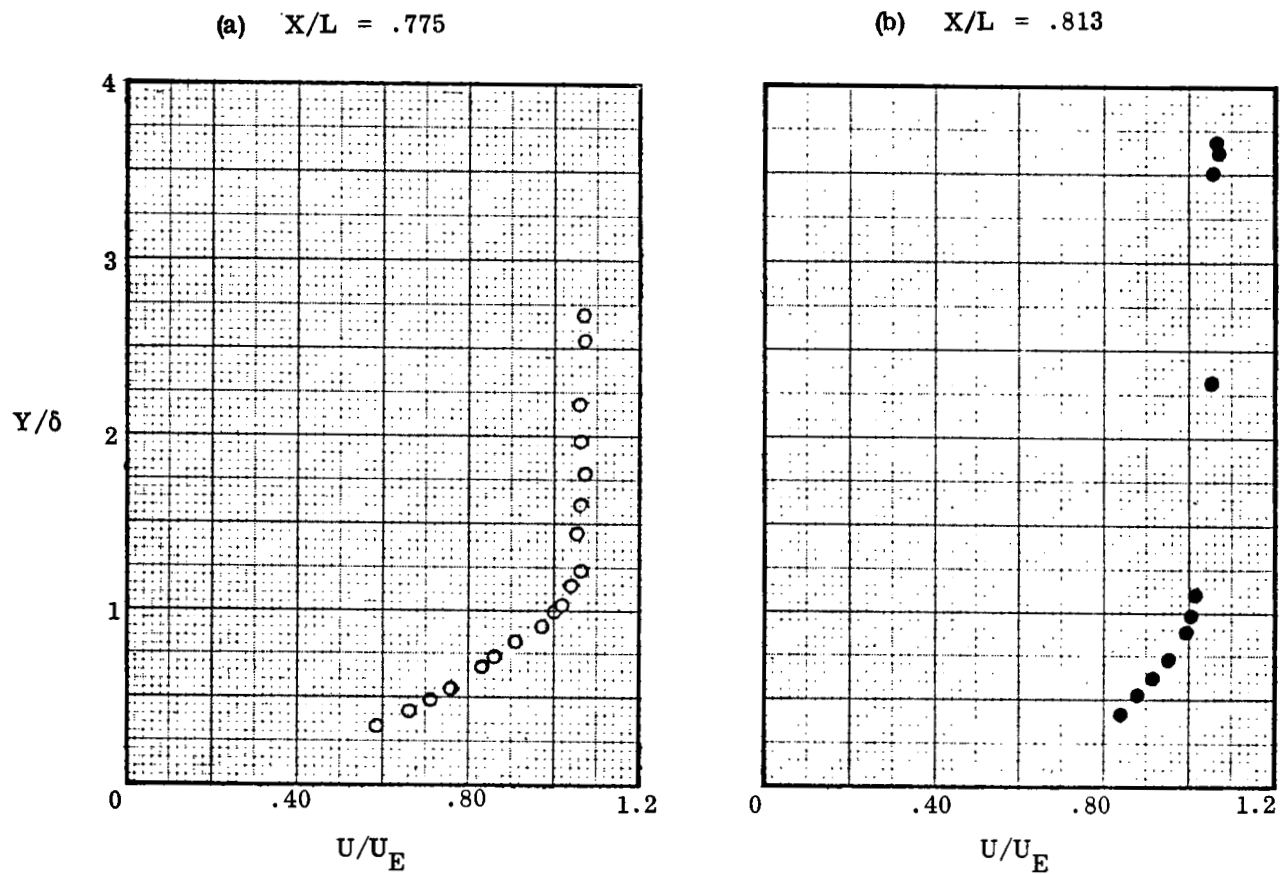$M_\infty = 7.4$, Re/ft = 2×10^6.

(a) X/L = .775　　　　　　　　　　(b) X/L = .813

Figure 49. STATIC PRESSURE PROFILES WITHIN ATTACHED, TURBULENT INTERACTION,
COMPRESSION SURFACE, .063 in. LEADING EDGE RADIUS,
$M_\infty = 7.4$, Re/ft = 2×10^6.

(a) X/L = .775

(b) X/L = .813

Figure 50. VELOCITY PROFILES WITHIN ATTACHED, TURBULENT INTERACTION,
COMPRESSION SURFACE, .063 in. LEADING EDGE RADIUS,
M_∞ = 7.4,   Re/ft = 2 x 10^6.
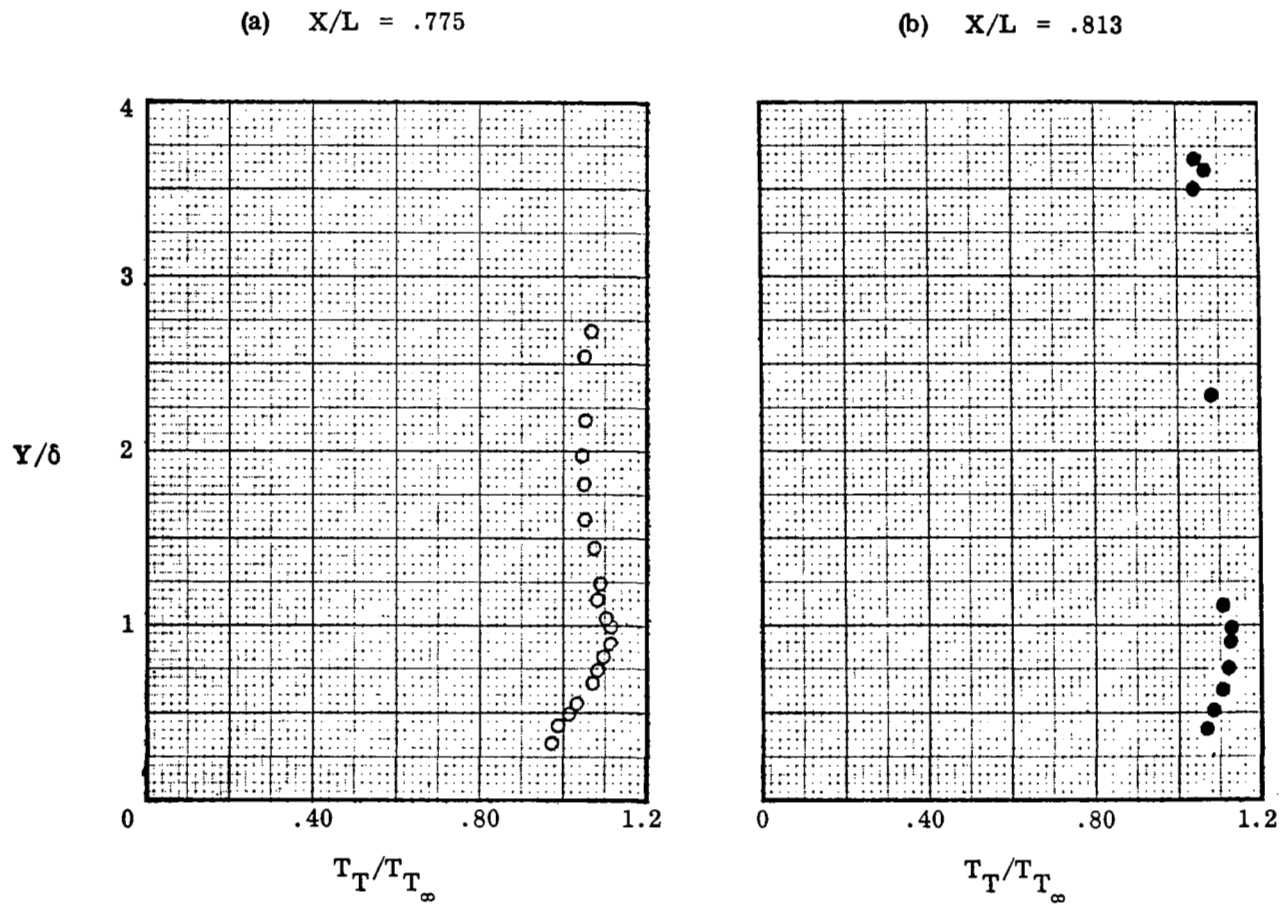
(a) $X/L = .775$ **(b)** $X/L = .813$

Y/δ

Figure 51. TOTAL TEMPERATURE PROFILES WITHIN ATTACHED, TURBULENT INTERACTION, COMPRESSION SURFACE, .063 in. LEADING EDGE RADIUS, $M_\infty = 7.4$, $Re/ft = 2 \times 10^6$.
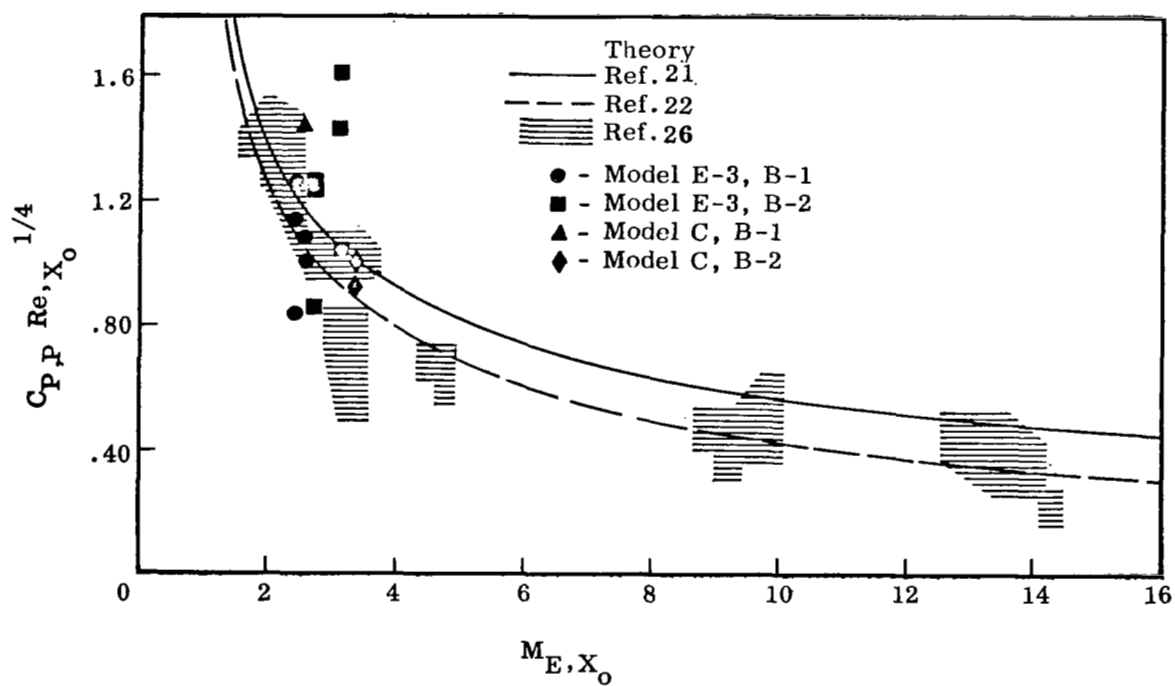
Figure 52. CORRELATION OF PLATEAU PRESSURE COEFFICIENT
OF SHOCK WAVE-LAMINAR BOUNDARY LAYER INTERACTION.

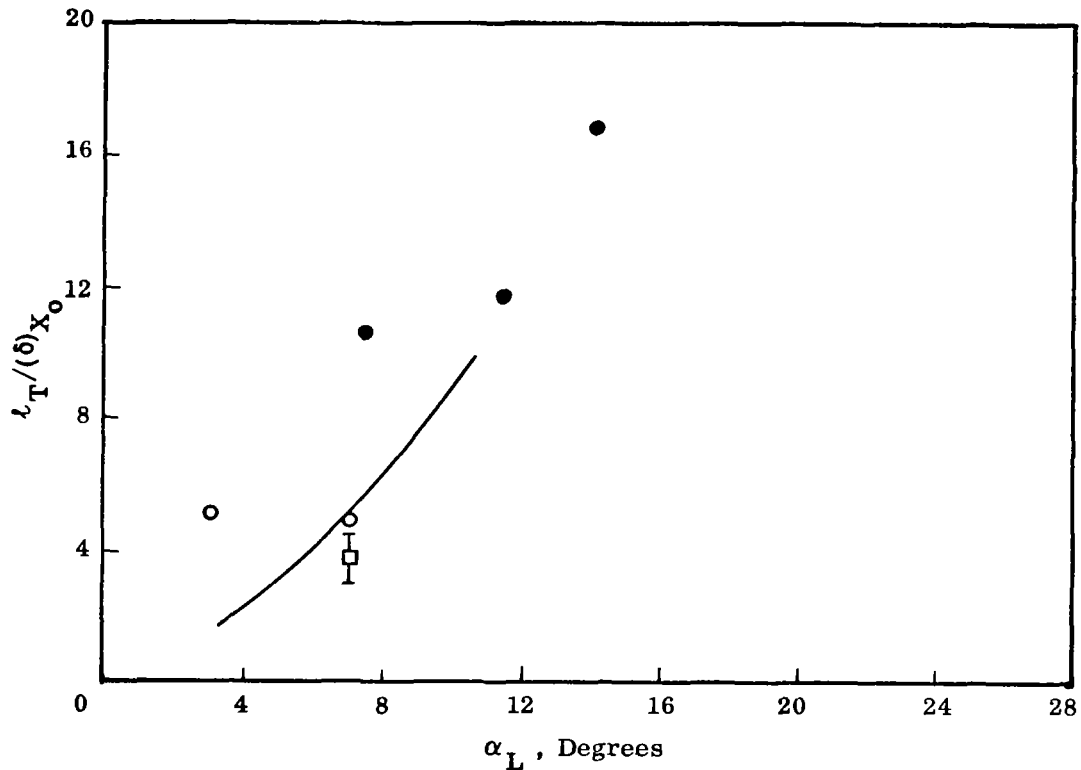|		$(M)_{X_O}$	$(n)_{X_O}$	$(Re_\delta) \times 10^{-5}$
●	.188 in. Leading Edge Radius, Trip Configuration No. 1	4.00	10.40	1.4
○	Sharp Leading Edge, Ref. 19	6.90	13.60	1.2
□	Sharp Leading Edge, Ref. 19	5.85	11.50	1.2
——	Theory, Ref. 28	4.00	7.75	1.0

Figure 53. VARIATION OF TOTAL TURBULENT INTERACTION LENGTH
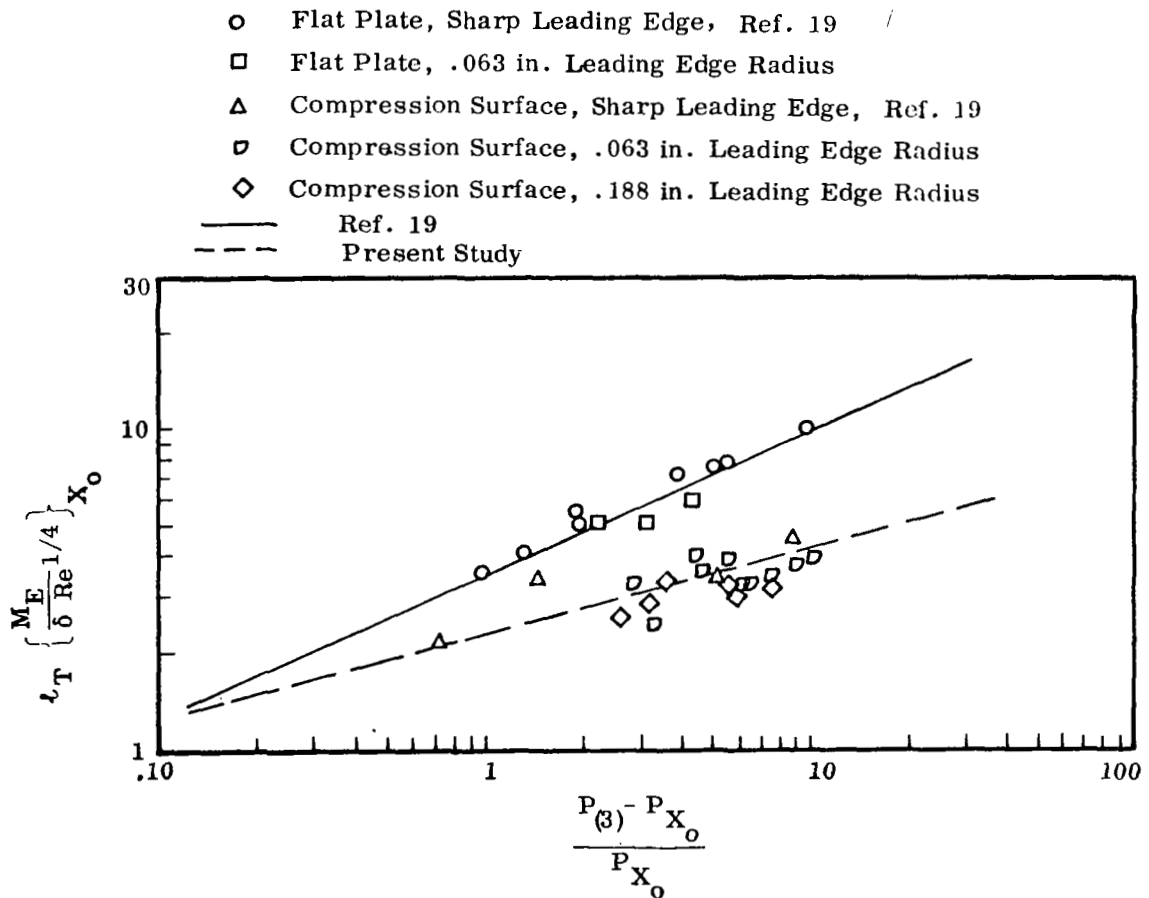WITH FLOW DEFLECTION ACROSS INCIDENT SHOCK,
(COMPRESSION SURFACE).

91

Figure 54. CORRELATION OF TOTAL LAMINAR INTERACTION LENGTH
WITH PRESSURE RISE.

"*The aeronautical and space activities of the United States shall be conducted so as to contribute . . . to the expansion of human knowledge of phenomena in the atmosphere and space. The Administration shall provide for the widest practicable and appropriate dissemination of information concerning its activities and the results thereof.*"

— NATIONAL AERONAUTICS AND SPACE ACT OF 1958

NASA SCIENTIFIC AND TECHNICAL PUBLICATIONS

TECHNICAL REPORTS: Scientific and technical information considered important, complete, and a lasting contribution to existing knowledge.

TECHNICAL NOTES: Information less broad in scope but nevertheless of importance as a contribution to existing knowledge.

TECHNICAL MEMORANDUMS: Information receiving limited distribution because of preliminary data, security classification, or other reasons.

CONTRACTOR REPORTS: Scientific and technical information generated under a NASA contract or grant and considered an important contribution to existing knowledge.

TECHNICAL TRANSLATIONS: Information published in a foreign language considered to merit NASA distribution in English.

SPECIAL PUBLICATIONS: Information derived from or of value to NASA activities. Publications include conference proceedings, monographs, data compilations, handbooks, sourcebooks, and special bibliographies.

TECHNOLOGY UTILIZATION PUBLICATIONS: Information on technology used by NASA that may be of particular interest in commercial and other non-aerospace applications. Publications include Tech Briefs, Technology Utilization Reports and Notes, and Technology Surveys.

Details on the availability of these publications may be obtained from:

SCIENTIFIC AND TECHNICAL INFORMATION DIVISION

NATIONAL AERONAUTICS AND SPACE ADMINISTRATION

Washington, D.C. 20546